THE IMPACT OF AGGREGATION OF DOUBLY FED INDUCTION GENERATOR BASED WIND TURBINES ON TRANSIENT STABILITY

Winnie Wambui Ngugi

A Thesis Submitted in Partial Fulfilment of the Requirements for the Degree of Master of Technology in Electrical and Electronics Engineering of Murang'a University of Technology

August, 2026

DECLARATION

Student Declaration

I hereby declare that this thesis is my original work and, to the best of my knowledge, has not been presented for a degree award in this or any other university. I understand what plagiarism is, and I am aware of the university's policy on this. I understand that any false claim regarding this work shall result in disciplinary action in accordance with the University Anti-Plagiarism Policy.

_____ _____

Winnie Wambui Ngugi Date

EN400/5200/2018

Supervisor Approval

The undersigned certify that they have read and hereby recommend for acceptance of Murang'a University of Technology a thesis entitled "**The Impact of Aggregation of Doubly Fed Induction Generator Based Wind Turbines on Transient Stability".**

_____ _____

Prof. Eng. Christopher Maina Muriithi, Date

Department of Electrical and Electronics Engineering,

Murang'a University of Technology.

_____ _____

Dr. Eng. Charles Mwaniki, Date

Department of Electrical and Electronics Engineering,

Machakos University.

DEDICATION

This thesis was dedicated my husband James whose dedication encouragement made it possible. To my children Stoney, Tracy and Ngugi for creating a conducive environment during my studies. The entire family members for their moral support.

ACKNOWLEDGEMENT

This thesis could not have been completed without the help, advice, and input of various individuals and institutions. First, I wish to thank the Almighty God for the strength, wisdom, and perseverance He granted me to devote the hours needed to complete this work.

I am deeply grateful to my supervisors, Prof. Eng. Christopher Maina Muriithi and Dr. Eng. Charles Mwaniki, for their invaluable advice, constructive criticism, and constant encouragement throughout the research process. Their experience and guidance were central to shaping the direction and quality of this study.

I also acknowledge the staff and management of Murang'a University of Technology for providing a conducive academic environment and the resources needed to carry out this research. My thanks extend to my colleagues and peers, whose comments and discussions played an important role in shaping this work. Finally, I owe my deepest thanks to my family for their unconditional moral support, patience, and encouragement throughout this academic journey.

ABSTRACT

Increasing wind power penetration challenges grid stability, yet simulating every turbine in a large wind farm individually is computationally prohibitive for transient stability studies. Existing aggregation techniques reduce this burden but are rarely evaluated alongside controller optimization, leaving open the question of whether aggregation can preserve the accuracy of transient stability while also improving computational efficiency. This study addresses that gap by developing an aggregated Doubly Fed Induction Generator (DFIG) wind farm model within the IEEE 39-bus benchmark system and tuning its grid-side, rotor-side, and DC-link PI controllers using Particle Swarm Optimization (PSO). The aggregated model's transient response was benchmarked against a fully independent (turbine-by-turbine) model under a range of symmetrical and unsymmetrical fault scenarios at Bus 6, using settling time, peak overshoot, and active/reactive power deviation as performance measures. PSO tuning improved settling time and peak overshoot by over 49% and 33%, respectively, relative to the unturned baseline. The aggregated model tracked the independent model's active and reactive power response to within 0.1% and 1%, respectively, while cutting simulation time by approximately 20%. These results show that coherency-based aggregation, combined with PSO-tuned control, offers a computationally efficient alternative to full wind-farm simulation without sacrificing transient stability accuracy a finding with practical value for grid operators and researchers modelling large-scale wind integration.

TABLE OF CONTENTS

DECLARATION ..... **ii**
DEDICATION ..... **iii**
ACKNOWLEDGEMENT ..... **iv**
ABSTRACT ..... **v**
LIST OF TABLES ..... **ix**
LIST OF FIGURES ..... **x**
ACRONYMS AND ABBREVIATIONS ..... **xi**
CHAPTER ONE: INTRODUCTION **1**
1.1 Background of the Study 1
1.2 Statement of the Problem 2
1.3 Objectives of the study 2
1.3.1 Main Objective 2
1.3.2 Specific Objectives 2
1.4 Research Questions 3
1.5 Significance of the Study 3
1.6 Scope and Limitation 4
1.7 Contribution of the Thesis 4
1.8 Organisation of the Thesis 5
CHAPTER TWO: LITERATURE REVIEW **6**
2.1 Introduction 6
2.2 Transient Stability in Wind-Integrated Systems 6
2.3 DIFG Wind Turbine Technologies and Generation Network Aggregation 8
2.4 Aggregation of Large Wind Power System Turbines 12
2.5 Wind farm aggregation methods 13
2.5.1 Detailed model (DM) 14
2.5.2 Aggregated model 14
2.5.3 Complete Wind Farm Aggregation Model 17
2.5.4 Aggregated wind farm model 18
2.6 Doubly Fed Induction Generator (DFIG) and the Dynamic Model 20
2.7 Control Strategies and PSO Optimization 22
2.8 Gaps in the Research 23
2.9 Summary 26
CHAPTER THREE: METHODOLOGY **27**
3.1 Introduction 27
3.2 Computational Environment and Tool Selection 27
3.3 Methodological Stages 28

3.4 Power System Model Development....29
3.4.1 The IEEE 39-Bus Benchmark System....29
3.4.2 Rotor Angle Dynamics and the Swing Equation....30
3.5 DFIG Wind Turbine Generator System Model....32
3.5.1 Aerodynamic Model....32
3.5.2 Mechanical Drive Train Model....34
3.5.3 Electrical Machine Model (Induction Generator)....34
3.5.4 Vector Control and Converter Strategy....36
3.6 Aggregation Methodology....37
3.6.1 Theory of Coherent Aggregation....37
3.6.2 Equivalent Parameter Scaling....38
3.6.3 Hybrid Aggregation Logic (Vestas V62 & Gamesa G62)....39
3.6.4 Collector System Aggregation....40
3.7 Controller Tuning Using Particle Swarm Optimisation (PSO)....40
3.7.1 Rationale for PSO....41
3.7.2 Optimisation Problem Formulation....41
3.7.3 Algorithm Mechanics and Implementation....42
3.8 Fault Scenarios and Stability Analysis Matrix....43
3.8.1 Fault Typology....43
3.8.2 Simulation Timeline and Sequence....44
3.9 Performance Indices and Data Analysis....45
3.9.1 Transient Response Metrics....45
3.9.2 Computational Efficiency Metric....46
3.9.3 Statistical Analysis of Hybrid Scenarios....46
3.10 Assumptions, Validation, and Limitations....47
3.10.1 Modelling Assumptions....47
3.10.2 Validation Strategy....47
3.11 Summary....48
CHAPTER FOUR: RESULTS AND DISCUSSION....49
4.1 Introduction....49
4.2 Steady-State Characterization and Baseline Analysis....49
4.2.1 Load Flow Analysis and Grid Stress Indication....49
4.2.2 Turbine Power Characteristics....50
4.3 Effect of PSO-Based Controller Tuning....52
4.3.1 PI Controller Gains and Scaling Logic Optimisation....52
4.3.2 Step Response Enhancement and Margins of the Stability....54
4.4 Comparison of Independent and Aggregated DFIG Models....56
4.4.1 Three-phase Ground fault and Aggregation....56
4.4.2 Unbalanced Fault and Sequence Component Analysis....59

4.4.3 Fault Ride-Through (FRT) and Recovery Trajectories 61
4.5 Statistical Analysis of Hybrid Aggregated Configurations 62
4.5.1 Robustness across Technology Configurations 62
4.5.2 Analysis of Steady-State Variance and Outliers 64
4.5.3 Hypothesis Testing and Justification of the "Average Machine" Assumption 65
4.6 Analysis of Computational Efficiency 66
4.6.1 Time savings in simulation and performance of a numerical solver 66
4.6.2 Scalability and Real-Time Application Potential 66
CHAPTER FIVE: CONCLUSION, RECOMMENDATIONS AND FUTURE WORK 68
5.1 Conclusion 68
5.2 Recommendations 68
5.3 Future Work 69
REFERENCES 70
APPENDICES 77

LIST OF TABLES

Table 2.1: Wind farm modeling methods 16
Table 2.2: Critical Review & Identified research gaps 25
Table 3.1: Fault typology applied at Bus 6 44
Table 3.2: Simulation timeline 45
Table 4.1: DFIG Control Parameter Gains independent and aggregated model 53
Table 4.2: PSO Tuning Performance Improvement 56
Table 4.3: Comparative Step Response Characteristics of the
various types of faults 60
Table 4.4: Hypothesis Testing for Model fidelity (N=27) 65
Table 4.5: Comparison of time to compute faults of various types 66

LIST OF FIGURES

Figure 2.1: The generic graph for LVRT simulator 7
Figure 2.2: DFIG wind turbine schematic diagram 9
Figure 2.3: Generation network aggregation case 1 10
Figure 2.4: Generation network aggregation case 2 10
Figure 2.5: case 3 of generation network aggregation 11
Figure 2.6: Transformer Aggregation 11
Figure 2.7: Interconnection of wind turbines 13
Figure 2.8: Aggregation of large wind farm to an equivalent WTG 13
Figure 2.9: Components of a DFIG aggregation wind farm 17
Figure 2.10: Inductor Motor classical equivalent circuit 19
Figure 2.11: Double Fed Induction Generator wind turbine 21
Figure 2.12: Doubly Fed Induction Generator wind turbine [48] 22
Figure 3.1: Stages in methodology 29
Figure 3.2: Flowchart for the code used to run PSO on the Simulink model 42
Figure 4.2: (a) p.u. of the generator synchronous speed; (b) nominal generator speed 51
Figure 4.3: Comparison of transient response 55
Figure 4.4: Active power transients 1 58
Figure 4.5: Voltage transient waveforms 58
Figure 4.6: Reactive power transient's waveforms 59
Figure 4.7: Box plot for the settling time 63
Figure 4.8: Box plot for the steady state 64

ACRONYMS AND ABBREVIATIONS

Abbreviation	Meaning
3G	Three-Phase-to-Ground Fault
3U	Three-Phase Ungrounded Fault
ADRC	Active Disturbance Rejection Controllers
AM	Aggregated Model
ANFIS	Adaptive Neuro-Fuzzy Inference Systems
ANOVA	Analysis of Variance
ASG	Adjustable Speed Generators
BESS	Battery Energy Storage Systems
BFOA	Bacterial Foraging Optimization
CCT	Critical Clearing Time
DFIG	Doubly Fed Induction Generator
DG	Distributed Generators
EMS	Energy Management System
EMT	Electromagnetic Transient
FAM	Full Aggregated Model
FRT	Fault Ride-Through
FSG	Fixed Speed Generators
GSC	Grid-Side Converter
GVO	Grid Voltage Orientation
HIL	Hardware-in-the-Loop
IGBT	Insulated-Gate Bipolar Transistor
IM	Induction Machine
IQR	Interquartile Range
ISE	Integral of Squared Error
ITAE	Integral of Time-weighted Absolute Error
LG	Single-phase-to-ground
LLG	Two-phase-to-ground
LPV	Linear Parameter-Varying
LVRT	Low-Voltage Ride-Through
MMM	Multi-Machine Model
MPPT	Maximum Power Point Tracking
MTDC	Multi Terminal DC

Abbreviation	Meaning
MV	Medium-Voltage
PCC	Point of Common Coupling
PI	Proportional-Integral
PLL	Phase-Locked Loops
PSO	Particle Swarm Optimization
PWM	Pulse Width Modulation
RMSE	Root Mean Square Error
RSC	Rotor-Side Converter
SAM	Semi-Aggregated Model
SCADA	Supervisory Control and Data Acquisition
SFO	Stator Flux Orientation
SMC	Sliding Mode Control
SME	Single Machine Equivalent
SSR	Sub-Synchronous Resonance
TFS	Transient Frequency Stability
TSO	Transmission System Operators
VSM	Virtual Synchronous Machines
WF	Wind Farm
WTG	Wind Turbine Generator

CHAPTER ONE
INTRODUCTION

1.1 Background of the Study

Advancements in wind power technology since the 1980s have led to exponential capacity growth, with global installed capacity doubling approximately every 4 years [1]. Wind energy is an essential energy source, and the associated power is fed into the grid at the point of common coupling (PCC). Wind turbines are often characterised by fluctuations in speed, control algorithms, type, and tower shadow, all of which affect the power generation. These turbines often have significant fluctuations in the output power due to the many connections of power from each turbine [1]. Therefore, fluctuations in each wind turbine's power significantly impact the power network [2]. Renewable energy sources like wind have become an integral part of modern power systems, as they are easily integrated into the smart grid [3]. The exhaustion of fossil fuels has driven the adoption of renewable energy [3], and, with the intermittent nature of sources like wind energy, aggregating wind turbines enables the simulation and study of the impact of large numbers of turbines on the grid.

For a system to be highly stable and secure, simulation of how it could withstand unsteady conditions during disturbances, such as bus or line faults and sudden equipment loss, is critical for anticipating design challenges [4]. The advantages of aggregating the Dynamic Induction Generator (DFIG) model include the ability to analyze wind farms, particularly in large-scale simulations. An aggregated DFIG method is introduced to Chowdhury et al., where individual turbines are simplified to ease their numerical representation and consequent numerically intensive actions at the expense of the required accuracy due to dynamic wind farms [5]. The aggregation is useful in speeding up simulations in large wind farms, reducing the computational cost during analysis by minimizing the number of equations to be solved to achieve a particular analysis. The aggregated models of DFIG are also important in enhancing power system stability via reactive power control [6]. These models improve grid stability using approximate dynamic programming [7]. These developments highlight the increasing need to address aggregated DFIG models in maximizing the deployment of wind power integration in power networks and stable grid operation.

1.2 Statement of the Problem

As more and more wind farms are adopted, their reliance on modern grids is increasing. Doing a full simulation for each turbine individually adds difficulties. Large wind farms became difficult to simulate and analyse due to the number of generators, which increased the computational time and memory requirements [1], [4], [8]. As [1] points out, frequency control systems sometimes require simplified DFIG models; higher-order equations introduce complexity. The trade-off between simplicity and accuracy is also addressed, as Xia et al. [2] propose the strategies of model reduction in situations when it is important to study the small-signal stability analysis of power systems. Moreover, the reduction of DFIG models can affect their reliability, since the individual dynamics of each turbine are approximated in the aggregation. As proposed by [5], DFIGs with similar operating conditions can be aggregated to significantly reduce computational cost without compromising the reliability of the model. While aggregation saves time, its "dependability" and "reliability" during severe grid disturbances (like faults) have not been thoroughly investigated. Furthermore, advanced tuning methods like Particle Swarm

Optimisation (PSO) for reactive-power control loops to supervisory controls has been designed to offset the lack of dynamic detail, but these have not been adequately examined [5], [6]. This research aims to investigate the effect of aggregating DFIG-based wind turbines on the transient stability of a power grid. A PSO-tuned aggregated model was used to quantify the trade-off between computational efficiency and simulation accuracy during severe grid disturbances.

1.3 Objectives of the study

1.3.1 Main Objective

The main objective of this research was to investigate the impact of the aggregation of Doubly Fed Induction Generators (DFIG)-based wind turbines on transient stability of the grid system using PSO.

1.3.2 Specific Objectives

The study specifically aimed to achieve the following objectives:

i. To formulate an aggregated model for a DFIG-based wind farm suitable for transient stability studies.

ii. To tune the PI controllers of both the aggregated and independent DFIG models using Particle Swarm Optimisation (PSO), and quantify the resulting improvement in transient response (settling time and peak overshoot) relative to their untuned baselines.

iii. To evaluate the extent to which the aggregated DFIG wind farm model preserves the transient stability accuracy of the independent, turbine-by-turbine model, and to quantify the computational efficiency gained through aggregation

1.4 Research Questions

This study was guided by and worked to provide an understanding of the areas covered by the following research questions:

i. How accurately does the aggregated DFIG model reproduce the dynamic response of the detailed independent turbine model, as measured by the Root Mean Square Error (RMSE), across the tested fault scenarios?

ii. To what extent does PSO-based tuning of the PI controllers improve the transient stability response of the aggregated and independent models relative to their untuned baselines?

iii. What is the quantifiable difference in computational time between the aggregated and independent wind farm models under multi-fault simulation scenarios?

1.5 Significance of the Study

The rapid increase in the number of installed DFIG wind farms and ratings demands Transmission System Operators (TSOs), grid planners and utility simulation teams to conduct comprehensive stability, protection-coordination and market-dispatch studies. Detailed electromagnetic modelling of individual turbines results in an extremely large differential system; thus, security checks and controller tuning can only be performed with Monte Carlo simulations, which are prohibitively long even on standard hardware. Benchmarks show that it is over 10 times slower to thoroughly study a 200-machine wind plant using a detailed model than to study the same plant with synchronous machines [7].

This was addressed by making use of aggregated DFIG models that combine turbines with similar electrical and wind behavior into one equivalent turbine. This combination enabled the model to deal with much smaller state data and maintain the necessary voltage and rotor-angle stability dynamics at the common coupling. An implementation of this aggregated model would have a practical payoff: it would reduce the average time of a simulation computation by about 18 to 20 per cent over independent modelling, including in multi-fault scenarios. These cuts, therefore, guarantee that the screening, small-signal analysis and iterative controller algorithms can be carried out within reasonable TSOs and system operator time constraints.

1.6 Scope and Limitation

The research study was limited to the development of an aggregated model of large wind power turbines with DFIG to assess transient stability, using IEEE 39-bus benchmark system. It included the simulation of the aggregated DFIG system, the optimization of the system control parameters using PSO, and the evaluation of the effects on transient stability in different multi-fault scenarios in the MATLAB/Simulink environment. The performance of the proposed system was then compared with an independent turbine model using step-response analysis and computational time. To define the limits, a number of specific modelling assumptions and constraints were considered. First, the simulation assumed a constant wind speed at 16 m/s, thus no aerodynamic variability or turbulence in the wind. Second, the analysis of the theory was limited to electromechanical transient stability; the constraints of Electromagnetic Transient (EMT) modelling and high-frequency electromagnetic fault interactions were not considered. This study addresses large-disturbance (transient) rotor-angle stability, evaluated through fault-induced step responses; small-signal (steady-state) stability analysis lies outside the scope of this work. The reference to small-signal analysis in Section 1.5 refers to a downstream application enabled by faster simulation, not an analysis performed in this thesis.

1.7 Contribution of the Thesis

This study contributes to the wind-integration literature in three specific ways: (i) it jointly evaluates aggregation accuracy and PSO-based controller tuning within a single, common simulation framework, rather than treating the two in isolation as most prior studies do; (ii) it demonstrates the aggregation methodology's robustness across

a heterogeneous, multi-technology wind farm (V62/G62 mixes), rather than a single homogeneous turbine type; and (iii) it provides a quantified accuracy-versus-efficiency trade-off (≈ 1% accuracy loss for ≈ 20% computational savings) that gives grid planners a concrete basis for deciding when aggregated modelling is fit for purpose.

1.8 Organization of the Thesis

The thesis is divided into five chapters. Chapter One provides the background on wind energy integration and states the problem statement and research objectives. It describes justification and scope, and the theoretical limits of the research. Subsequently, Chapter Two presents a critical review of transient stability in wind-integrated systems and DFIG mathematical modelling principles. It also presents wind farm aggregation and PSO control methods and, finally, defines the specific research gaps this study addressed. Then Chapter Three describes the MATLAB/Simulink simulation environment and defines the mathematical models, including the IEEE 39-bus system model, detailed DFIG modelling, and the aggregation strategy. Besides, it includes the PSO optimization framework and the multi-fault simulation scenarios. Chapter Four then discusses the steady-state performance and analyses the improvements in dynamic step response provided by PSO tuning. It establishes the stability comparison between independent and aggregated models of various types of faults, both statistically and computationally. Lastly, Chapter Five provides a conclusion of the main findings. It clearly presents the research limitations and provides practical recommendations for grid stakeholders and future research.

CHAPTER TWO
LITERATURE REVIEW

2.1 Introduction

This chapter reviews the literature on aggregated DFIG for enhancing grid transient stability. It explores fundamental concepts of transient stability in wind-integrated systems, detailed DFIG technology and mathematical models, various aggregation methods for wind farms, advanced control strategies including Particle Swarm Optimisation (PSO), and identifies key research gaps addressed by this study. Emphasis is placed on recent advancements, highlighting the impacts of high wind penetration, optimization techniques for fault-ride-through, and computational efficiency in large-scale simulations.

2.2 Transient Stability in Wind-Integrated Systems

Transient stability describes how a system tends to remain at a steady state under a severe disturbance. In systems with high penetration of DFIG-based wind farms, the intermittent nature of wind resources introduces variability that can reduce overall system inertia and damping, potentially leading to instability [8]. For instance, studies indicate that DFIG integration can either enhance or degrade transient stability depending on factors like penetration levels and control settings; at up to 70% penetration, optimized DFIG parameters such as rotor speed and stator resistance can increase the critical clearing time (CCT) by improving fault ride-through capabilities [9]. Aggregated models are crucial for efficient analysis, as they simplify complex wind farms into equivalent representations, reducing simulation time while preserving key dynamic responses at the point of common coupling (PCC) [10]. Recent studies also note that grid coupling and inertia constants have minimal impact on DFIG transient stability, whereas load models significantly influence outcomes, with constant-impedance loads providing better stability margins [11]. Furthermore, in multi-machine systems, DFIG wind farms can supply reactive power during faults, preventing voltage collapse and supporting synchronization torque, though high penetration may exacerbate angular separation if not properly controlled [12]. Additional factors like gearbox ratio and reactive power control further affect transient responses, emphasizing the need for tailored strategies in wind-integrated grids [10]. The achievement of transient stability is dependent on the severity of the disturbance

and initial operating point of the system as shown in Figure 2.1. Instability of the system is a periodic angular separation of the system from its initial operation point and happens when the system lacks adequate synchronization torque [13]. During short circuit state, DFIG feedbacks the reactive power to the grid due to the solid-state electronic converter. The scenario of the DFIG, therefore, is advantageous to maintain the higher voltage at the PCC to achieve no-voltage collapse. Having the wind turbine connected to the grid also helps maintain the integrity of the automated control systems in the grid. Information systems such as the EMS (Energy Management System), SCADA (supervisory control and data acquisition), and Power World Retriever are the most popular in automation and management of grid systems. These systems assign a state or a variable to each turbine. This means a state variable's disappearance of would make the system unstable.

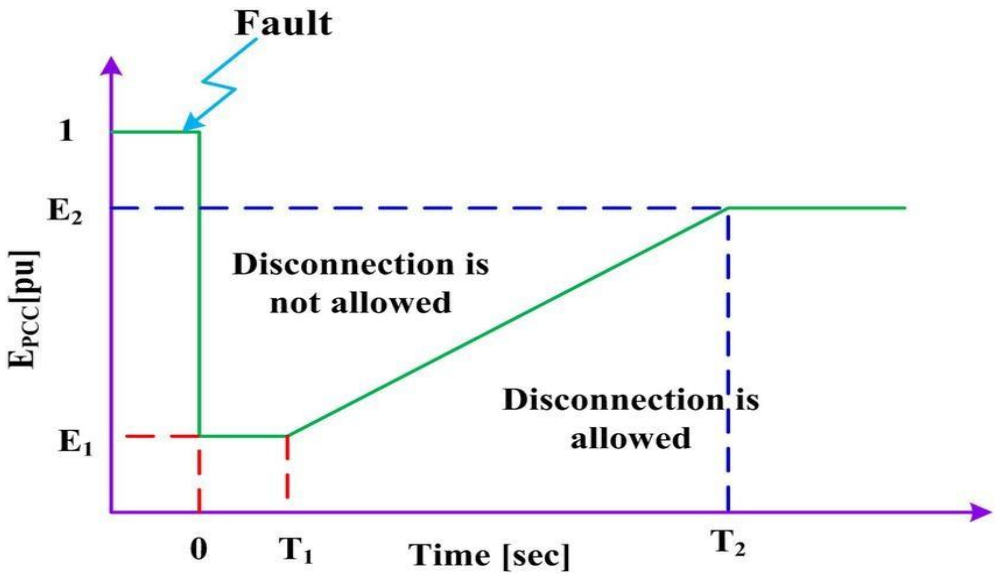


Figure 2.1: The generic graph for LVRT simulator

. Decoupling the DFIG rotor and high installation are two characteristics that deteriorate the synchronization torque and degrade the system inertia [14] placing the DFIG rotors in a better position compared to conventional synchronous generator. During a system fault, the two aforementioned characteristics also cause an increase in the aggregated angular acceleration/deceleration of the synchronous generators jeopardizing the system's stability performance. Transient stability index is calculated using time-domain nonlinear simulations for the initial normal operating system. This is used to determine the DFIG system stability margin. [15] [16]. The controller can

be trained without the mathematical model to achieve stability based on approximate programming supplementary learning [17].

2.3 DIFG Wind Turbine Technologies and Generation Network Aggregation

Doubly Fed Induction Generators (DFIGs) are widely adopted in wind turbines for their variable-speed operation, achieved via back-to-back converters that connect the rotor to the grid, enabling independent control of active and reactive power [18]. The mathematical model includes active power extraction given by

$$P = (\frac{1}{2})\, \rho A V^3(\lambda, \beta) \qquad 2.1$$

where ρ is air density, A is swept area, V is wind speed, and C_p is the power coefficient dependent on tip speed ratio λ and pitch angle β [19]. Reactive power and voltage are regulated via proportional-integral (PI) controllers, with phase-locked loops (PLL) ensuring synchronization [20]. Key advantages include efficient energy capture (up to 10% more than fixed-speed generators), reduced mechanical stress on gearboxes, improved reactive power support, and lower acoustic noise [21]. However, drawbacks include sensitivity to grid faults, the need for crowbar protection or advanced controls for low-voltage ride-through (LVRT), and potential sub-synchronous resonance (SSR) in series-compensated lines [22]. Dynamic models often use voltage and torque equations in stationary or synchronous reference frames, with state variables such as rotor or air-gap flux, which simplify analysis for stability studies [23]. Recent developments focus on hybrid models incorporating fuzzy logic or neural networks to handle uncertainties in wind speed and grid conditions [24]. For floating offshore applications, oriented control models assess mechanical stability and reveal vulnerabilities to wave-induced oscillations [21].

Wind turbines are classified into four major types: induction generators with fixed rotor resistance, DFIGs, wound-rotor induction generators, and full-converter generators. During short-circuit conditions, both induction and wound-rotor induction generators must be immediately disconnected from the grid. This is because the generator draws reactive power, which increases the voltage drop and affects grid stability. This is why it cannot be used as a large electricity generation source. DFIG is connected directly to the grid using back-to-back electronic converters (ac-to-dc-to-ac) at fixed frequency. This, therefore, allows the DFIG motor to consume the power

within the given limits through the change of the rotor currents' magnitude. DFIGs can remain connected during a fault by supplying reactive power to sustain voltage levels, thereby increasing voltage stability at the voltage nodes [25].

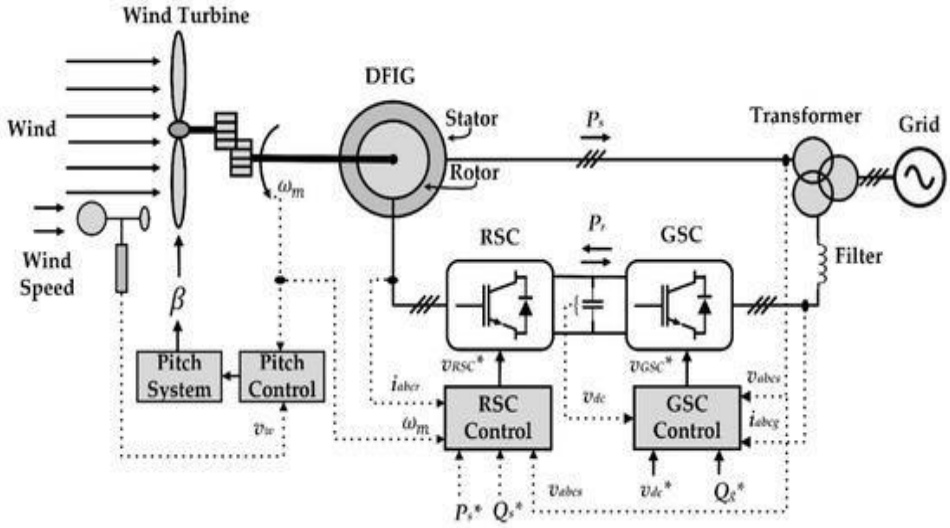


Figure 2.2: DFIG wind turbine schematic diagram

The figure 2.2, as from **[**26] represents the DFIG aggregation with the aim of simplifying the wind farm model while maintaining the accuracy. This is a pictorial depiction of a wind turbine connection to a transmission system.

Aggregation of the generated network model development may need to develop and formulate a representation of the wind power plant, considering the power lost at the point of voltage drop [27]. Several layouts may have different levels of impact depending on the impedance of the grids interconnected to the buses. The technique for calculating the line equivalent characteristics, in accordance with the prior conditions and the configuration of the lines, may be highly effective in the aggregation process of the generated network [5]. In this case, two main assumptions can be made: first, that the current wind turbines have similar magnitudes and angles. The second assumption that can be made is that reactive power being generated by the line capacitive shunts may be based on the assumption that voltage is only one per unit (1 p.u). The two main types of layouts can therefore be assessed.

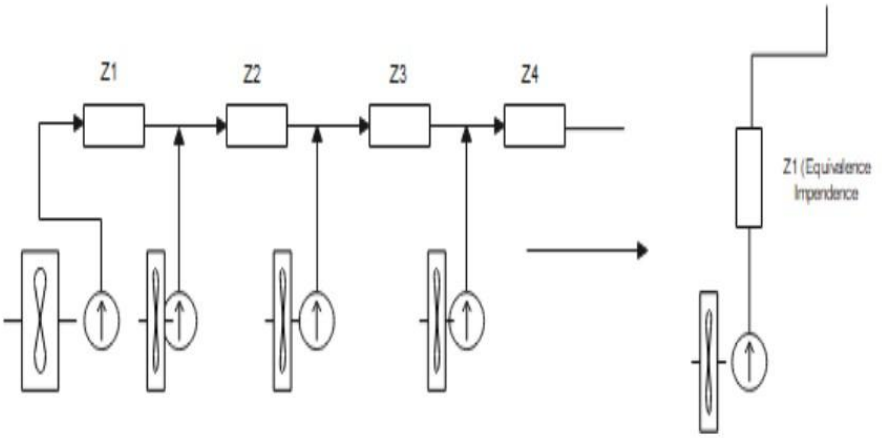


Figure 2.3: Generation network aggregation case 1

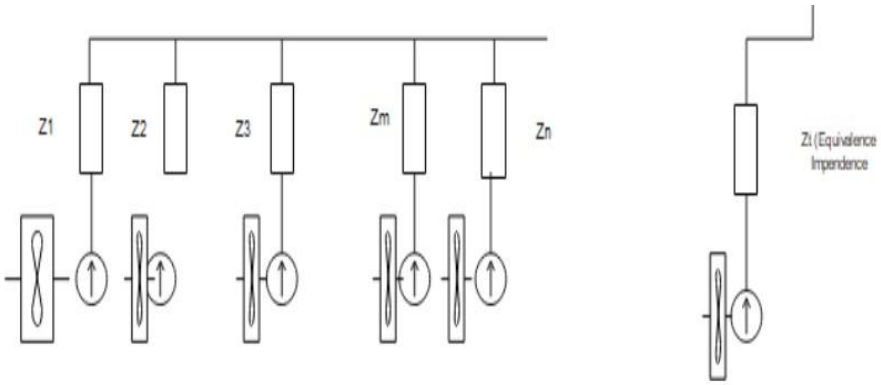


Figure 2.4: Generation network aggregation case 2

Figure 2.3 above as from [28] gives an indication of a diagram with corresponding row showing a chain of configuration. Figure 2.4 on the other hand shows correspondence to the aggregation of different numbers of rows, highlighting several branches in connection to the same node. Upon the generation taking the form of figure 2.5, equivalence of the impendence can be illustrated by; [5]

$$Zt = \frac{\sum_{m=1}^{n} m2Zm}{n2} \qquad 2.2$$

Where:

Z_m is the branch impedance at m impedance in branch m, whereas n represents the total number of branches.

In order to shunt the representation of the equivalent susceptance, it is given by [5]

$$Bt = \sum_{i=1}^{n} Bi \qquad 2.3$$

Whenever the lines are lying parallel to one another as indicated in figure 2.5, the equivalent formula for determination of aggregated model for the resultant line needs to be equivalent to the number of losses of the lines of the detail model and can be represented by equation 2.4

$$(t) = \sum_{m=1}^{n} n \qquad 2.4$$

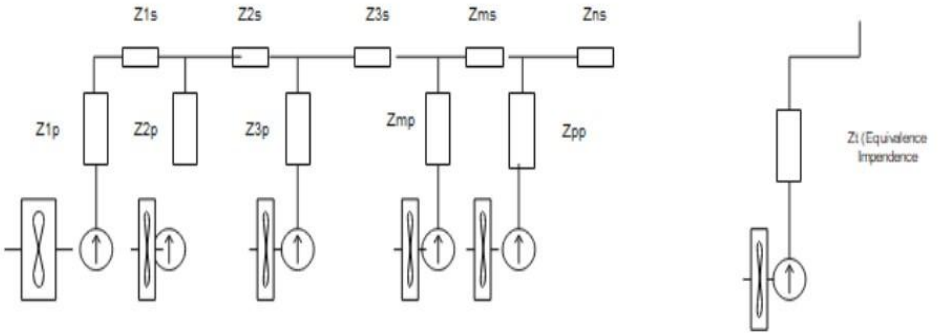


Figure 2.5: case 3 of generation network aggregation

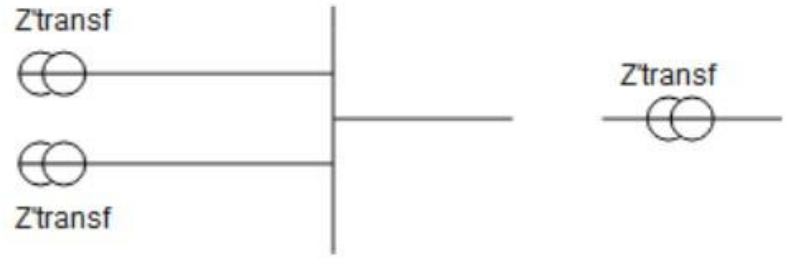


Figure 2.6: Transformer Aggregation

2.4 Aggregation of Large Wind Power System Turbines

Aggregation techniques are essential for modelling large wind farms in power system studies, reducing computational complexity by representing multiple turbines as equivalents while maintaining accuracy in transient responses [29]. Common methods include: Detailed Model (DM) for small-scale analysis of individual turbine dynamics; Aggregated Model (AM) to lower system order; Full Aggregated Model (FAM) assuming uniform wind conditions, using weighted averages for parameters like impedance; Semi-Aggregated Model (SAM) for varying wind speeds, aggregating torques to a single generator; and Multi-Machine Model (MMM) clustering turbines by similar operating points, such as wind speed or power curves [30]. Recent advances introduce dynamic aggregation prioritizing reactive power equivalence over wind homogeneity, effectively managing overvoltage and decoupling aggregation from wind variability [31]. Model-data-driven equivalents integrate simulation data with clustering algorithms, achieving up to 87% reduction in computation time and errors below 5% in voltage dips [32]. These methods positively impact CCT, with aggregated DFIG farms improving stability at high penetrations by smoothing power fluctuations and enhancing reactive support, though accuracy diminishes under non-uniform winds without proper grouping [31]. Comparisons show MMM outperforming

FAM in diverse conditions, reducing simulation time by 50-70% for large farms [30]. Simplified models for frequency control further aid aggregation, balancing simplicity and accuracy in assessing power variations [30]. The development of a windfarm and installation of several wind turbines is meant to smooth the irregularity of the wind diversity and hence increase the reliance of the wind as an electricity source. Figure 2.7 below depicts the connection of each wind turbine to the transmission line via a pad-mounted transformer at the foot of each turbine. The pad-mounted collector increases the voltage level because it is connected to an underground collector. Underground collector systems act as a link between the transformers and the substation.

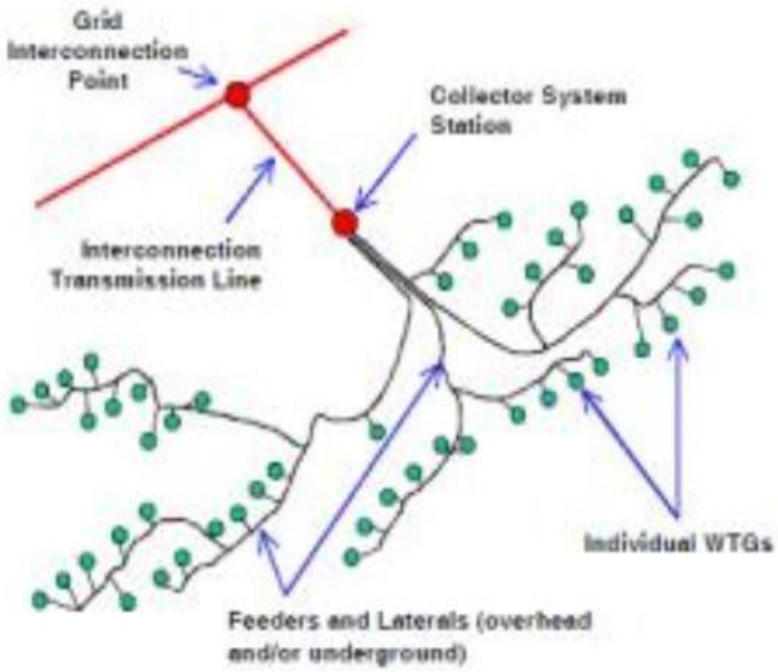


Figure 2.7: Interconnection of wind turbines

As in the figure 2.7 above, simplification of the network is seen as it reduces the network's size by equating all turbines to a single machine as shown in the figure 2.8 below. This single machine equivalence has a better load flow and stability, improves planning, and ease of operating the plant.

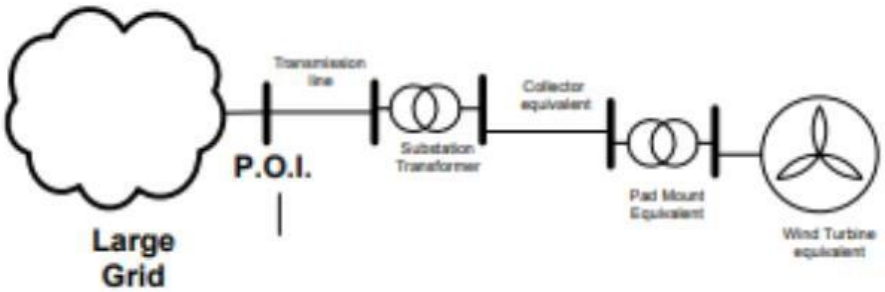


Figure 2.8: Aggregation of large wind farm to an equivalent WTG

2.5 Wind farm aggregation methods

During network aggregation and simplification, there is greater reliance on the chosen aggregation method. As stated in [32], the stability of the system depends on the stability methods used. Finding a suitable aggregation method is a complex task that

has attracted the attention of many researchers. Given the impact of the aggregated model on system behavior, identifying an effective, efficient, and reliable aggregation model is indispensable. A system can be presented in a detailed or aggregated form [33]. An aggregation of a wind farm is a modeling technique used to obtain the farm's overall response at the PCC. The following section discusses commonly used modeling and aggregation methods.

2.5.1 Detailed model (DM)

This is a modeling technique in which all the wind turbines are fully modeled, including electrical networks such as cables and transformers. The DM is appropriate when studying the dynamic behaviors of one or a few wind turbines. This model is inappropriate for many wind turbines. This is because the model will grow to a higher-order model, hence consuming more computational time. These characteristics disadvantage the use of DM and necessitate the use of aggregated models for wind turbine power studies.

2.5.2 Aggregated model

This is a modeling technique in which all the wind turbines are aggregated to form a single- or multi-machine equivalent at the PCC. This means that the aggregated model will provide a system equivalent electrical network at the PCC. This modeling reduces the system's order and the computational time. Given the wind turbines' dependence on wind conditions, the operating points are evidently dependent on wind characteristics. The probability of the firm having different wind speeds necessitates a consideration of the modeling. This, therefore, determines the aggregation method used. The following are the aggregation methods

2.5.2.1. Full aggregated model (FAM)

This is the process where all the wind turbines are aggregated into one equivalent turbine since they have similar operating points (the same turbines in the firm receive the same velocity of wind at the same angles). The challenge facing the implementation of this modeling technique is the process of calculating the wind equivalent for each wind turbine. [34] calculates the equivalent wind turbine with the turbines receiving different wind velocities using the equation:

$$S_{eq} = \sum_{i=1}^{n}; \quad P_{eq} = \sum_{i=1}^{n} P_i \qquad 2.5$$

Where:

i = and index

S_i = MVA rating of the individual generator

P_i = real power of the individual generator

This formula depicts a weighted mean method representation of a calculation for the parameters of the equivalent model. Also, the parameters of the equivalent model are represented using the weighted mean method [33] [35].

2.5.2.2 Semi-aggregated model (SAM)

This is an aggregation model that aggregates the generators into an equivalent generation system, without aggregating the independent wind turbines, thereby modeling an equivalent generation unit driven by independent turbines. This aggregation model is appropriate for situations where the wind characteristics received by all the turbines vary. The difference in wind velocities received by the wind turbines is converted into a mechanical torque that is transmitted and aggregated to obtain an equivalent torque fed to the generation system. Both full and semi-aggregation models have been used in wind farms owing to the characteristics of permanent magnet synchronous wind turbines.

2.5.2.3 Multi machine model (MMM)

The second strategy used to cater for the irregular distribution of wind among the wind turbines in the wind farm. This aggregation model groups wind turbines with identical wind characteristics and thus at the same operating point; they are aggregated together and hence form an equivalent machine for this group. This signifies that there will be several groups of aggregated models and hence the wind farm will have multiple equivalent machines. [36] Investigated the aggregated DFIG wind turbines based on sorting the wind turbines that receive identical wind characteristics. The analysis led to the development of power curves and the turbines with the same characteristics could be grouped. The importance of MMM in solving issues of diversity in wind turbine characteristics, incident wind velocity differences, and line impedances in the development of the aggregated wind farm models.

Table 2.1 below provides a recap of the aggregation models discussed herein:

Table 2.1: Wind farm modeling methods

Method	Description	Pros	Cons
DM	Models **ALL** wind turbines	Convenient for small number of wind turbines	Higher-order models when a large number of turbines are aggregated
FAM	All wind turbines are aggregated into one equivalent turbine with a single internal electrical network	Reduced computational time and reduced order of the system	It is disadvantaged by irregular incident wind characteristics
SAM	Generators are aggregated without aggregating wind turbines.	Captures impacts from irregular wind characteristics.	Relatively high order and greater computational times
MMM	Groupings are made based on wind turbine characteristics or incident wind characteristics, and aggregated together	Captures the reality of wind irregularities and wind turbine differences	Relatively high order model and longer computational times.

Studies on these influences justify the need to develop dynamic wind farms with a large number of generators. However, detailed models take longer to compute. In the past, the electrical model for aggregation has been used alongside non-aggregated models to achieve better estimates of the collective response at the PCC of the wind farm [15].

In this study, new approaches using simplified, reduced-order aggregation models that include a complete DFIG model have been considered. This is because the mode of aggregation should be inclusive of wind turbines with different operational conditions and incident wind conditions. Every wind turbine has a scaled power capacity needed to feed an equivalent torque into the aggregated system. The model for wind aggregation includes a smaller number of equations. Therefore, the effectiveness of the model for aggregation can be demonstrated by comparing the approximations of the response observed at the PCC and the simulation computation time with those obtained using a complete set of wind farm models. The generation of most of the bus

system generators is up to 319.6 MW, with the load supplied by the generators approximated at 315 MW of active power and 115 MVAR of reactive power [37].

2.5.3 Complete Wind Farm Aggregation Model

The DFIG wind farm consists of induction generators (wound-rotor), which are connected to the wind turbines, with the drive train placed in between. The stator of the generator is in direct connection to the generator grid, with the generator rotor connected through a back-to-back converter (IGBT-PWM) in the presence of the DC link capacitor. The wind farm model for aggregation can be well represented based on the nature and behavior of the subsystems in the main induction system.

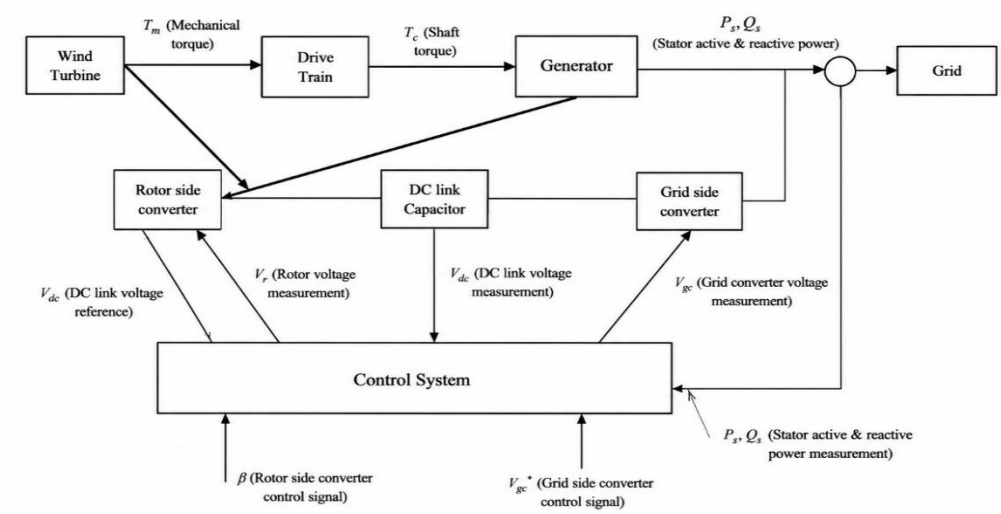


Figure 2.9: Components of a DFIG aggregation wind farm

Figure 2.9 illustrates the flow of energy and data in a DFIG wind farm. Mechanical energy flows from the turbine through the drivetrain to the generator as torque (Tm, *Tc*). Electrically, power flows from the stator (*Ps*,*Qs*) to the grid, while a bidirectional path connects the rotor to the grid through rotor-side and grid-side converters linked by a DC capacitor. The control system regulates this process by collecting feedback measurements, including rotor, DC-link, and grid voltages (Vr, Vdc, Vgc), as well as stator power, and issuing specific control commands (β, *Vgc*) to the converters to ensure synchronization, stability, and optimal power output.

Wind-based generation is a current technology that plays a significant role in the power technology mix. It is the most common and is present in different scales,

ranging from multi-megawatt turbine generators installed in extremely large wind farms to small sub-kilowatt units found in individual and independent installations. Because of the many connections that may be involved, there is a great need for an equivalent model that can accurately represent the behavior of the WF at the grid connection point without recording a significant increase. During the aggregation of the wind turbine, the decision regarding simplification depends on the type and level of accuracy required.

2.5.4 Aggregated wind farm model

A precise aggregation model should represent the DFIG wind farm response accurately [38]. However, achieving this will be difficult and hence the precise model should have the highest possible accuracy. Systems studies such as 'Impact of Large Wind Power Integration on

Transient Stability has demonstrated the necessity of a high-fidelity computational model in aggregation.

This calls for aggregation to reduce the model order and the required computational time. Aggregation and modeling of wind generators in a wind farm into a single equivalent generator reduces computational time and model order.

The aggregated model at PCC represents active and reactive power. Detailed wind farm models are used to validate aggregated ones. Another validation technique is by taking actual measurements of an operational wind farm [3] [2]. The detailed aggregated models are then used to analyze and study the transient stability of the generation systems. This is because the modeled systems demand fewer computational resources and hence require shorter computational time. The analysis of wind farm generators during system faults is better performed using detailed wind farm models. Utility-scale power integrates multiple wind farms, making aggregated wind farm models appropriate for investigating the system's transient stability and for reducing computational times.

This study employs the no-load test, locked-rotor test, and induction motor aggregation. As proposed by [39] in this aggregation method, the two operating conditions can determine the parameters of the aggregate induction. These two

conditions are: no load and locked rotor. For this method, an assumption is made for both the load and no-load conditions.

For no load, slips of the induction motors should be equivalent to zero, whereas slips in locked rotor are the same as unity. Figure 2.10 below shows equivalent circuits for the aggregate motor-load induction.

- Xs is the stator reactance, Rs is the stator resistance.
- Xm is the magnetic reactance
- Xr is the rotor reactance
- S is the slip of the induction motor.

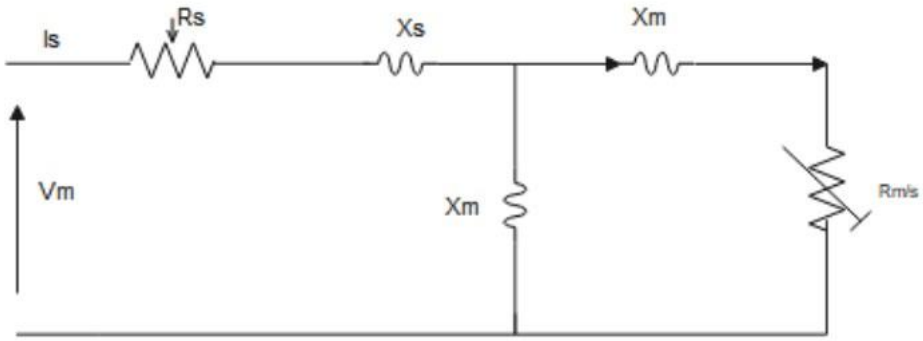


Figure 2.10: Inductor Motor classical equivalent circuit

Crucially, the chosen aggregation method directly impacts the fidelity of the transient response. When individual turbines are lumped into a Single Machine Equivalent (SME), the diverse aerodynamic torque ripples and high-frequency inter-turbine jitter are mathematically filtered out. While this smoothing effect is beneficial for studying bulk power transfer and inter-area oscillation modes, a poorly scaled aggregated model can mask localized stability degradation mechanisms, such as individual converter saturation or localized voltage collapse. Therefore, contemporary literature dictates that an effective aggregation strategy must accurately scale not only the steady-state capacities but also the collective inertia and controller gains to ensure the SME exactly mimics the reactive power injection trajectory of the original detailed farm during the critical milliseconds following fault clearance.

2.6 Doubly Fed Induction Generator (DFIG) and the Dynamic Model

Double Fed Induction Generator is often preferred because it has the ability to meet the modern grid codes necessities and the grid turbine system, having the capacity of reactive power support

[40]. The DFIG is a wind turbine-based system that is highly preferred over other power aggregation systems. In a DFIG, reactive power is delivered 'doubly', at the stator and the rotor, and hence can be supported on either side [41]. For the DFIG, the wind turbine starter is connected in parallel with the grid rotor, with which it is interfaced through a power converter. On the other hand, the voltage applied to the stator is supplied from the grid [42]. The rotor voltage is generated by induction from a power converter. The power is delivered to the grid via power converters when the generator operates above synchronous speed.

The DFIG has the following advantages:

- They possess better energy capture compared to the other fixed-speed generation generators
- It can store energy from sudden wind gusts
- The generator's gearbox has less stress
- There is better control to the reactive power injected to the generator
- Acoustic noise reduction

The DFIG allows for constant AC supply at constant frequency even when the rotor's speed varies with the wind velocity. This is achieved by using converters that carry a set fraction of the generated power and hence reducing the power losses and the total cost of equipment unlike the full converter.

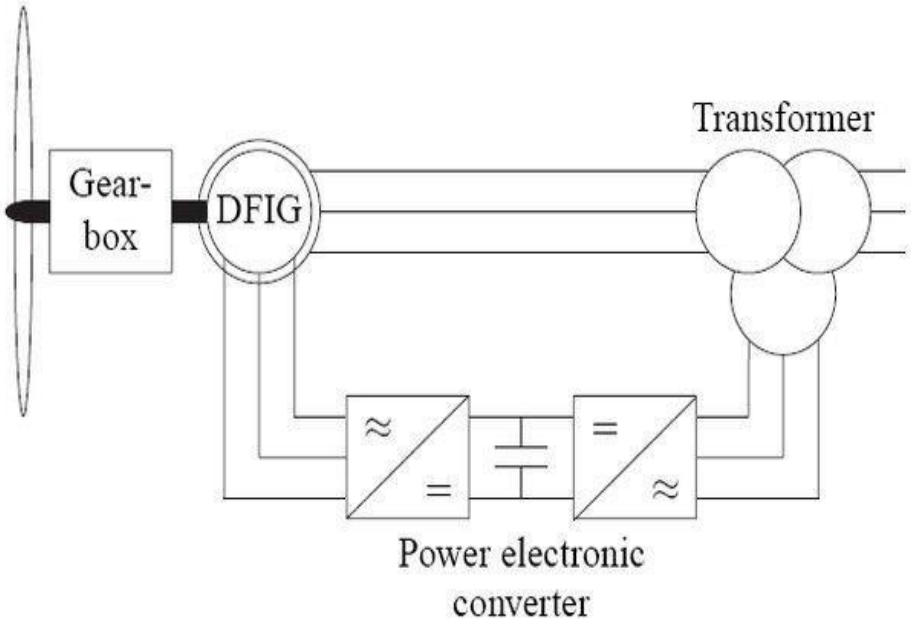


Figure 2.11: Double Fed Induction Generator wind turbine

The development, construction, and performance of fixed-speed wind turbines depend heavily on the attributes of the mechanical sub-circuits, which may include pitch control time constants, maximum switching rate of a main breaker, etc. The approximate ranges of the mechanical circuits are on the order of tens of milliseconds. However, [44] criticized the Double Fed Induction Generator Wind Turbine, noting that the DFIG might not be able to withstand stronger gusts of wind, which may hit the wind turbine faster and cause a large variation in electric output. Variations in voltage may require not only changes in the load but also a stiff power grid for stable operation, and an effective mechanical design to absorb high levels of mechanical stress. This strategy is highly expensive for mechanical construction, especially at high power ratings.

Modern turbines have high power ratings and adjustable-speed capability. They are termed as adjustable speed generators (ASG). Compared with fixed-speed generators (FSGs), ASGs are highly cost-effective. This is attributed to reduced pitch-control complexity and peak power requirements [45] [46]. Pitch angle control is implemented to achieve maximum power output for any incident wind speed. There is a wide range of power output by a turbine as a function of the speed of incident wind, between the lowest power output and the maximum turbine output. This results in up to 10% efficiency. The figure below shows the output power as a function of turbine and wind speed.

A DFIG dynamic model is needed during the aggregation of the large wind power penetration. DFIG is similar in construction to a wound-rotor induction machine (IM). It comprises a three-phase stator winding and a three-phase rotor winding [47]. The slip rings are fed through the latter.

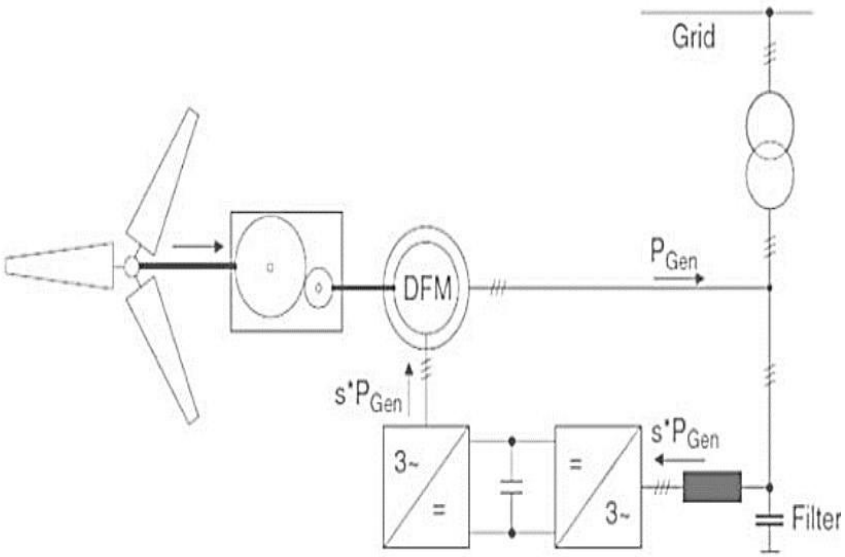


Figure 2.12: Doubly Fed Induction Generator wind turbine [48]

2.7 Control Strategies and PSO Optimization

The selection of an optimization algorithm is critical for tuning the highly coupled, non-linear Proportional-Integral (PI) controllers of the DFIG. While classical tuning methods (like Ziegler-Nichols) assume linearity and fail under severe grid disturbances, meta-heuristic algorithms offer global search capabilities. A critical comparison of optimization techniques reveals that Particle

Swarm Optimization (PSO) presents distinct advantages over Genetic Algorithms (GA) or Differential Evolution (DE) for power system control. Unlike GA, which relies on complex evolutionary operators such as crossover and mutation, PSO uses a simpler velocity-position update mechanism based on swarm intelligence. This results in significantly faster convergence rates and lower computational overhead when searching the continuous, multimodal parameter space characteristic of back-to-back converter control loops. Consequently, PSO is uniquely suited for minimizing settling times and overshoots in transient stability applications.

Control strategies for DFIGs focus on maximizing stability by optimizing converter parameters, pitch angles, and reactive power dispatch [51]. Particle Swarm Optimization (PSO) is prominently used to tune PI controllers, minimizing overshoot and settling time in response to disturbances [24]. For grouped reactive power control, PSO optimizes across turbine groups while using proportional allocation within each group, increasing active power output by 0.05 p.u., stabilizing voltages, and reducing computation by 50% [32]. In hybrid systems with distributed generators (DGs), PSO placement improves transient frequency stability (TFS) by 10-14.5%, though integration with HVDC links may worsen oscillations [52]. Advanced techniques include linear parameter-varying (LPV) feedback for robust control, virtual synchronous machines (VSMs) to mimic inertia, and sliding mode control (SMC) to mitigate SSR [22]. PSO-based adaptive neuro-fuzzy inference systems (ANFIS) enhance pitch-angle control in variable-speed DFIGs, reducing fluctuations by 15-20% under turbulent wind conditions [51]. Hybrid PSO with bacterial foraging optimization (BFOA) or swarm algorithms further refines MPPT and voltage regulation, achieving faster convergence and better fault tolerance [24]; [52]. These optimizations are critical for grid-connected systems, ensuring compliance with grid codes and enhancing overall resilience [23]. Prescribed convergence laws and nonlinear active disturbance rejection controllers (ADRC) provide additional performance boosts in rotor current control [23]; [20].

2.8 Gaps in the Research

Existing literature predominantly relies on outdated sources (pre-2020), overlooking recent advancements in dynamic aggregation and PSO-tuned controls for high-penetration scenarios [11]. Weak synthesis often summarizes studies sequentially without critically addressing contradictions, such as the benefits of aggregation in stability enhancement versus risks of accuracy loss in non-uniform conditions [31]. Limited focus on PSO for aggregated models ignores computational reductions and performance under diverse faults. This study bridges these gaps by developing an aggregated DFIG model with PSO-tuned controls, comparing transient performance against independent models, achieving 20% computation time reduction, and validating through IEEE 39-Bus simulations for improved grid resilience.

Previous studies have explored aggregating large wind penetrations using different systems, though with varying methodological approaches.

According to J.K and C Muriuki [53], the aggregation method included the analysis of transient stability in transmission and distribution, assuming the generation point. Transient stability measures the ability of the power systems to maintain synchronism under severe transient disturbances, and forms a critical basis of assessing the system stability levels. Researchers have analyzed the voltage in the fixed turbine models leaving a gap on transient stability assessment [15].

In most cases, DFIG wind turbines are adopted in major wind farms for wind power penetration analyses, and the IEEE 39-Bus system has been used as a benchmark in simulating the large wind power penetration [53]. In essence, a study by [39] reviewed dynamic models of wind aggregations with fixed-speed turbines and established that different aggregation methods can be used in the wind aggregation process. On the other hand, a study [54] determined the extent to which aggregation helps with synchronism. A related study analyzed the transient stability of a front-end speed-controlled wind turbine using MATLAB/Simulink, aggregating the wind farm only partially rather than in full.

The study explored the development of an aggregation model of wind power plants and integrating it into a conventional grid for transient stability analysis. This chapter presents a review of the relevant literature on developing a detailed, aggregated model of a Doubly Fed Induction Generator that reduces the system to one machine for the transient stability of power systems.

Table 2.2: Critical Review & Identified research gaps

Author(s) & Year	Core Focus / Scope	Methodology & Benchmark System	Key Strengths & Contributions	Critical Limitations	Identified Research Gaps / Future Directions
Wang et al. (2025)	Dynamic Aggregation & Overvoltage Protection	Dynamic equivalent modeling for PMSG wind farms under high-voltage ride-through (HVRT).	Models overvoltage protection triggering and non-uniform fault responses accurately.	Primary emphasis on PMSG; limited PSO parameter tuning for converter-level loops.	**Gap:** Co-optimizing converter controller gains while dynamic overvoltage protection mechanisms trigger across heterogeneous wind farms.
Amrane et al. (2025)	PSO-Tuned Direct Power Control (DPC)	Robust IP/PI controller gain optimization for DFIG converters on dSPACE hardware.	Demonstrates superior active/reactive power decoupling and hardware validation.	Tested on a standalone turbine setup rather than a multi-machine aggregated grid benchmark.	**Gap:** Scaling PSO-tuned converter algorithms from standalone DFIG setups to full single-machine aggregated models on multi-bus networks.
Liu et al. (2024/2025)	Physics-Informed / ML Aggregation	Physics-informed machine learning for two-machine dynamic wind farm aggregation under LVRT.	Achieves ~87% computational reduction during severe low-voltage dips.	Dependent on rich SCADA training sets; fails under unlearned, black-box fault scenarios.	**Gap:** Hybridizing data-driven ML dynamic aggregation with heuristic search (PSO) to ensure parameter robustness under unlearned faults.
Zhang et al. (2025)	Dynamic Stability in High Wind Systems	Kuramoto-like reduced oscillator modeling on an improved IEEE 39-Bus benchmark.	Reduces critical coupling strength by 17% and bounds fault limit removal time errors within 10%.	Simplifies turbine dynamics into lower-order oscillators, omitting inner-loop control optimization.	**Gap:** Integrating detailed inner-loop converter dynamics and meta-heuristic tuning into reduced-order oscillator models on transmission benchmarks.
Yenealem et al. (2025)	PSO-PID Control in High-Penetration Grids	Sensitivity-guided PSO optimization for PI/PID gains in hybrid renewable power grids.	Minimizes peak overshoot and frequency oscillations under severe power fluctuations.	Modeled individual generation units without considering dynamic wind farm aggregation.	**Gap:** Quantifying the performance loss of PSO-tuned controllers when transitioning from full-scale models to single-machine equivalent models.

Ren et al. (2025)	Grid-Forming Aggregation Modeling	Dynamic aggregation of grid-forming (GFM) renewable plants for frequency/voltage dynamics.	Extends aggregation theory to grid-forming topologies with power synchronization loops.	Lacks analysis under severe symmetrical/asymmetrical fault transient conditions.	**Gap:** Extending dynamic equivalent aggregation and meta-heuristic controller tuning to hybrid plants containing both grid-following and grid-forming DFIGs.

2.9 Summary

Existing literature relies heavily on outdated sources, static models, and partial aggregation, leaving a critical gap in assessing dynamic transient stability and optimized control efficiency in high-wind power systems. This study's methodology directly bridges these literature gaps through a targeted three-part approach. First, it formulates a single-machine aggregated DFIG wind farm model within the IEEE 39-Bus benchmark using MATLAB/Simulink to model high penetration. Next, Particle Swarm Optimization (PSO) tunes the PI controllers of both aggregated and independent models to minimize settling time and peak overshoot. Finally, comparative simulations confirm the aggregated model preserves transient accuracy while achieving computational time reduction.

CHAPTER THREE
METHODOLOGY

3.1 Introduction

This chapter presents the methodology used to evaluate the transient stability of grid-connected DFIG-based wind farms under a matrix of fault scenarios on the IEEE 39-bus New England benchmark system, focusing on two central considerations: wind farm aggregation and controller tuning. An Independent Model, in which every turbine was represented explicitly, served as the ground truth against which an Aggregated Model was verified across two turbine technologies, the Vestas V62 and Gamesa G62, with Particle Swarm Optimisation (PSO) applied to controller tuning in both. Section 3.2 outlines the computational environment and tools adopted for this work, and Section 3.3 sets out the overall methodological workflow; the remaining sections then detail the power system model, the DFIG and aggregation formulations, the PSO tuning procedure, and the fault scenarios and analysis methods used to evaluate the results.

3.2 Computational Environment and Tool Selection

In this work, MATLAB R2021a, along with the Simulink and Simscape Power Systems toolboxes, was used. The study required a combination of electromechanical power systems models, scaled power-electronic models (PWM converters), and mechanical drives. Simscape provided blocks that supported such heterogeneous domains. The equations characterizing the power systems were robust, with time constants ranging from microseconds due to switching transients to seconds for electromechanical swings. The ode23t and ode15s variable-step solvers of MATLAB were tailored to ensure a numerically correct solution in the case of discontinuities caused by fault inception and clearance.

Moreover, one of the most critical aspects of the methodology was PSO tuning of controllers. MATLAB provided a platform to repeatedly execute Simulink simulations, extract performance measures, and update controller parameters in a closed loop via native scripting. This combined process is less demanding to execute than conventional power system analysis packages like PSS/E or DIgSILENT PowerFactory, without interfacing with other packages. The formulation of system

parameters was done using MATLAB scripts (.m files), while dynamic simulations in Simulink (.slx models) and post-processing of the output time-series data was done to obtain transient stability indices. This unified system ensured that the process of data flow between the definition of parameters and the eventual statistical analysis was both automated and repeatable.

To handle the intensive computational load required for solving the high-order differential equations of the detailed 108-turbine model, all simulations were executed on a high, performance Lenovo X380 Yoga. The hardware configuration utilized an Intel Core i7 processor (or equivalent), 16 GB of RAM, and a 64-bit operating system. This robust hardware environment, combined with MATLAB's variable-step solvers, prevented memory saturation and allowed for efficient execution of the multi-fault simulations.

3.3 Methodological Stages

The research study was structured into six different but also related phases as shown in Figure 3.1. The flowchart outlines a structured, six-step system evaluation workflow designed with integrated feedback mechanisms. The process begins with initial system development, followed by detailed turbine modeling and the application of an aggregation strategy. Once the framework is set, controller parameters are optimized, leading directly into fault analysis testing. At this stage, the outcome undergoes a primary evaluation to determine if system performance is satisfactory; if unsatisfactory, the loop reverts to repeat the fault analysis. When performance meets the benchmark, a second check determines if further fault scenarios require testing. If additional scenarios exist, the flow loops back to controller optimization; otherwise, the process concludes with final system validation.

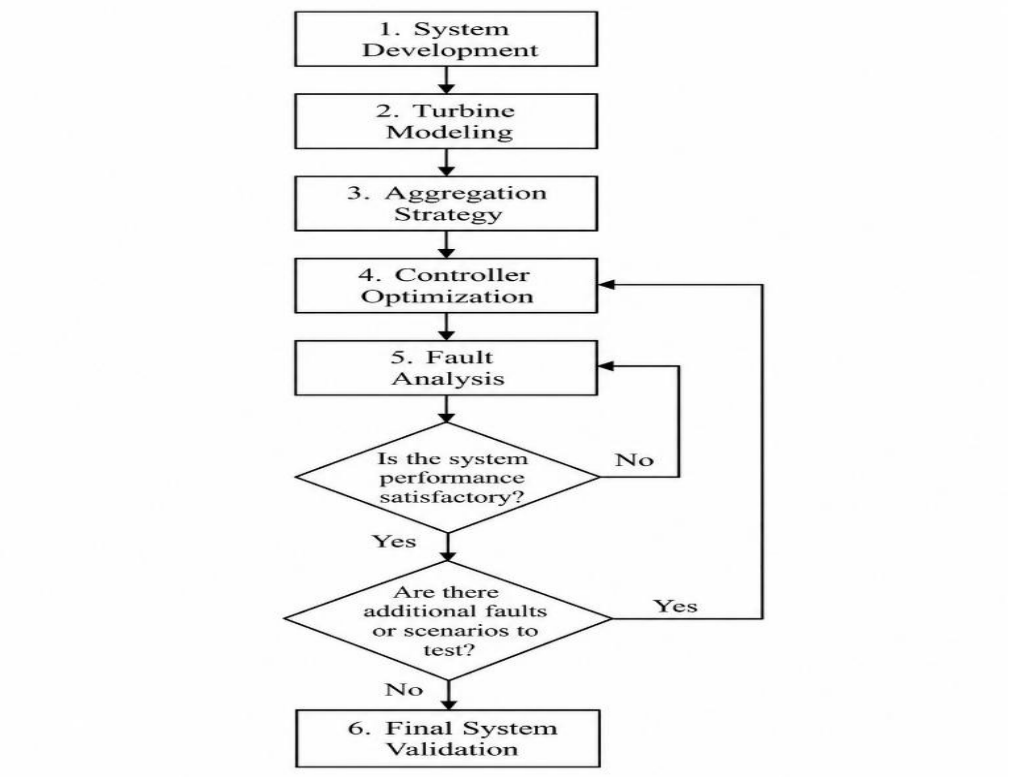


Figure 3.1: Stages in methodology

The remainder of this chapter follows this workflow, beginning with the development of the power system model in Section 3.2.

3.4 Power System Model Development

3.4.1 The IEEE 39-Bus Benchmark System

The system network chosen in this research was the IEEE 39-bus New England Power System.

This system was originally proposed by [73], and is a typical standard of dynamic stability analysis in power engineering. It provides a simplified and representative representation of the New England 345 kV high-voltage transmission network of the United States. It was chosen based on its dynamic complexity, having oscillation modes in the IEEE 39-bus system many of which are local plant modes and inter-area mode. This provides a testing platform to evaluate the effects of renewable system integration on wide-area stability. The system was composed of 39 buses and 10 generators and 19 load centers connected with a transmission net comprising 34 lines and 12 transformers. It has a non-radial topology to reduce the multiple fault-current paths.

i. Generators

The system contains ten generators. Generator 1, at Bus 39 was represented by the equivalent aggregation of the large interconnection. Generators 2-10 were modelled to represent the thermal and hydro stations in the New England grid. Bus 6, due to its central position in the network, was considered a heavy fault connection [73].

ii. Loads

This system was modeled with a total active load of 6.1GW. The PQ loads were used to solve the transient-stability analysis in the power-flow model. In the simulation these were also transformed into voltage-dependent impedances to perform the dynamic analysis to capture load relief during voltage dips [74].

iii. Transmission lines

The transmission lines were modeled as 34 using the equivalent Pi(π) model Simulink blocks, thus a series impedance ($Z = R + jX$) and shunt susceptance (B) at the ends. This perfectly represented the line-charging currents, which are typically significant at 345kV [75]. To examine the role of doubly-fed induction generators (DFIGs), the system was modified by adding a scaled wind farm aligned with the displaced synchronous generation, ensuring that the steady-state power flowing in the system matched the benchmark base case. This approach allows for a direct comparison of the generation type, synchronous or asynchronous [72].

3.4.2 Rotor Angle Dynamics and the Swing Equation

It was essential that the synchronous generators' capability sustained synchronism after a disturbance in the power system. While the DFIGs have no load angle, thus asynchronous, their interaction with the grid, in particular, their active-power recovery and their reactive-power support, had a direct effect on the accelerating torque experienced in synchronous machines.

Therefore, the swing equation was used to control the system's stability response [76]. The Newton Law of Rotation of the Second law, which gives angular momentum change as the product of the net torque on the rotating mass, formed the basis of dynamic behavior of a synchronous generator as in equation 3.1.

$$J\frac{d^2\theta_m}{dt^2} = T_m - T_e \qquad 3.1$$

Where J represents the sum of the generator and turbine moment of inertia ($kg.\ m^2$). θ_m is the angular position of the rotor relative to a fixed axis in mechanical radians, T_m is the mechanical torque of the prime mover and is positive when generating and T_e is the magnetic opposing torque to rotation (including retarding losses).

To make this equation useful in the analysis of power systems, it was normalized and transformed into electrical per-unit quantities. Here we refer to the constant of inertia, H, as the kinetic energy of the rotating mass at synchronous speed that equals the rated apparent power S_{rated} in MVA, of the machine as in equation 3.2

$$H = \frac{\left(\frac{1}{2} J\ \omega_{m0}^2\right)}{S_{rated}} \qquad 3.2$$

When substituted into the rotational equation with power converted to torque, ($P = T\omega$), we have the standard Swing equation that was used in the Simulink model as in equation 3.3

$$\frac{2H}{\omega_0}\frac{d^2\delta}{dt^2} = P_m - P_e - D(\omega - \omega_0) \qquad 3.3$$

Where δ is the angle of rotation of the rotor in electrical radians about a synchronously rotating frame of reference ($\delta = \theta_e - \omega_0 t$), ω_0 is the synchronous electrical speed, ω is the real rotor electric speed, P_m is the mechanical power input that is normally a constant because the response of the governor is slower than the moment of transient window, P_e represents the electric output power and D is damping factor, which is the sum effect of damper windings and mechanical friction.

The term $P_m - P_e$ in equation 3.3, defines the accelerating power P_a. With a pressure difference of zero, the machine has no acceleration and is in a steady state, rotating at a synchronous velocity. In the case of a fault condition introduced by Bus 6, the system voltage collapses. The

EV voltage drop in transmission of electrical power is proportional to voltage, ($P_e \propto$ $___X \sin\delta$), and thus the voltage drop of the electrical power decreases steeply. The mechanical prime mover (steam or hydro turbine) is incapable of responding instantly, hence, P_m remains high. It leads to a large positive change in the force on the rotor, which accelerates with the resultant improvement in the angle of rotation, δ. The stability is achieved when the deceleration of the rotor is sufficient following

the clearing of the fault to ensure that there is no indefinite increase in the value of the δ (slipping a pole). It is conceptually identical to the Equal Area Criterion that the kinetic energy gained during the fault (accelerating area) has to be counterbalanced by the energy dissipated after the fault (decelerating area) as in equation 3.4

$$\int_{\delta_0}^{\delta_{clear}} (P_m - P_e)\, d\delta + \int_{\delta_0}^{\delta_{max}} (P_m - P_e)\, d\delta = 0 \qquad 3.4$$

In this research study, the wind farm of DFIG power plant affected this balance by introducing active power (P_{dFIG}) and reactive power (Q_{DF}). The faster recovery of fault aided in load support, decreasing load of the synchronous generators. On the other hand, DFIG reactive current injection was meant to increase the local voltage, V, which, in effect, increasing the electrical power capability of nearby synchronous machines, increased their decelerating capability [76]. These interactions are explicitly modeled by the simulation that solves the swing equations of the remaining nine synchronous machines alongside the DFIG control dynamics.

3.5 DFIG Wind Turbine Generator System Model

The use of DFIG in wind turbines technology allows for variable-speed, over both a broad band (± 30) percent of synchronous speed with an active and reactive power independent control. The dynamic model of the DFIG used in its methodology includes four interrelated sub-models: aerodynamic, mechanical, electrical machine and converter control [77]. The model are shown in

3.5.1 Aerodynamic Model

The aerodynamic sub-model determines the mechanical torque that is transferred by the turbine rotor in the wind. This is a non-linear process governed by the laws of momentum theory.

The mechanical power captured by the turbine is given by equation 3.5.

$$Pmech = {}^{1}_\, \rho A V w^{3}(\lambda, \beta) \qquad 3.5$$

Where the air density ρ, was assumed constant at 1.225 kg/m³ [6], A is the swept area of the rotor proportional to the rotor radius. For the Vestas V62, the rotor diameter was 62 meters, yielding a swept area of approximately 3,019 m². V_w is the free-stream wind speed incident on the rotor plane and (λ, β) is the aerodynamic power coefficient, representing the efficiency of the turbine. The power coefficient is a function of the tip-speed ratio (λ) and the blade pitch angle (β). The tip-speed ratio is defined as the ratio of the linear speed of the blade tip to the wind speed as in equation 3.6.

$$\lambda = \frac{\omega_t R}{V_w} \tag{3.6}$$

To capture the accuracy of the aerodynamic performance of the Vestas V62 and Gamesa G62 then the study adopted a standardized, nonlinear empirical representation of the power

coefficient C_p and equation 3.7

$$C_p(\lambda, \beta) = c_1 (c^2 - c_3\beta - c_4)^{(-c\lambda 5_i)} + c_6\lambda \tag{3.7}$$

Where the variable is given as in equation 3.8

$$\frac{1}{\lambda_i} = \frac{1}{\lambda + 0.08\beta} - \frac{0.035}{\beta^3 + 1} \tag{3.8}$$

The coefficients, c_1, c_2, c_3, c_4, c_5, c_6, were obtained regarding the performance charts as 0.5176, 116, 0.4, 5, 21, and 0.0068. This term is appropriate to describe the inefficiency of an increase in the pitch angle or an increase in the turbine moving away from the most efficient tip-speed ratio. Similarly, the aerodynamic torque T_{aero} that acts at the hub was modelled based on the balance of mechanical power as in equation 3.9

$$T_{aero} = \frac{P_{mech}}{\omega_t} = \frac{1}{2}\rho\, \pi\, R^3 V_w^2 \frac{C_p(\lambda, \beta)}{\lambda} \tag{3.9}$$

This non-linear relation in wind speed, rotor speed, and torques played a significant role in the simulation, since the decrease in the torque of the generator and the wind speed kept constant led to acceleration of the rotor. The aerodynamic model thus ascertained the extra energy developed in the proceeding acceleration, which has a direct bearing in the intensity of the disturbance occurrence.

3.5.2 Mechanical Drive Train Model

The transient-stability investigations required the elasticity of the mechanical connections between the turbine's high-inertia rotor and the generator's low-inertia rotor. A simple lumped-mass model cannot compute the torsional oscillations that can appear in the drive-train shaft whenever grid faults occur and produce severe torque shocks. As a result, the Two-Mass Drive Train Model was used. The rotating machine was divided into two masses: the turbine mass J_t and the generator mass J_g connected by a flexible shaft represented as a spring-damper system. The equations governing the system included the turbine equation of motion (3.10),

Generator equation of motion (3.11) and shaft twist equation (3.12). A simplified "lumped mass" model was insufficient because it could not reproduce the torsional oscillations in the drive-train shaft during severe torque shocks associated with grid faults.

$$2H_t \frac{(d\omega_t)}{dt} = T_{aero} - K_s(\theta_t - \theta_g) - D_s(\omega_t - \omega_g) \quad 3.10$$

$$2H_g \frac{d\omega_g}{dt} = K_s(\theta_t - \theta_g) + D_s(\omega_t - \omega_g) - T_{elec} \quad 3.11$$

$$\frac{d(\theta_t - \theta_g)}{dt} = \omega_t . \omega_{base} - \omega_g . \omega_{base} \quad 3.12$$

where H_t and H_t are the inertia constants of the turbine and generator, respectively (typical values on an 860kW machine are H_t = -3.5 s, and H_t = -0.5 s). Shaft stiffness and the damping coefficients in p.u. torque/rad and p.u. torque/ p.u. speed, respectively) are denoted by K_s and D_s, and the electromagnetic torque generated by the DFIG is denoted by $Telec$. This model captured the phenomenon of shaft windup caused by an instantaneous change in apparent power on the grid due to faults. The drivetrain acts like a torsion spring, causing the generator rotor to vibrate against the turbine rotor.

3.5.3 Electrical Machine Model (Induction Generator)

The electrical dynamics of the DFIG were given in a synchronously rotating d-q reference frame. The transformation ensured synchronism with the stator magnetic

flux rotor turning at the synchronous speed, and thus changing time-varying sinusoidal quantities of AC into constant value DC quantities, and making the design of linear PI controllers simpler. The stator-rotor windings interaction was assumed to be magnetic and is described with the flux linkage equations 3.13, to 3.16.

$$\psi_{ds} = L_s\, i_{ds} + L_m i_{dr} \tag{3.13}$$

$$\psi_{qs} = L_s i_{qs} + L_m i_{qr} \tag{3.14}$$

$$\psi_{dr} = L_r i_{dr} + L_m i_{ds} \tag{3.15}$$

$$\psi_{qr} = L_r i_{qr} + L_m i_{qs} \tag{3.16}$$

in whichL_s and L_rr are the overall stator and rotor inductances, including the leakage L_{ls} L_{lr} and L_m is the magnetizing inductance.

The voltage balance between the windings takes into consideration resistive drops, transformer EMF (time derivative of flux) and rotational EMF (speed voltage) were defined as stator equation 3.17 and 3.18, besides rotor equation 3.19 and 2.20.

$$v_{ds} = R_s i_{ds} - \omega_s \psi_{qs} + \frac{d\psi_{ds}}{dt} \tag{3.17}$$

$$v_{qs} = R_s i_{qs} + \omega_s \psi_{ds} + \frac{d\psi_{qs}}{dt} \tag{3.18}$$

$$v_{dr} = R_r i_{dr} - (\omega_s - \omega_r)\psi_{qr} + \frac{d\psi_{dr}}{dt} \tag{3.19}$$

$$v_{qr} = R_r i_{qr} + (\omega_s - \omega_r)\psi_{dr} + \frac{d\psi_{qr}}{dt} \tag{3.20}$$

Where the difference ($\omega_s - \omega_r$) is the slip speed. The rotor of a DFIG was excited at slip frequency, which, when combined with the mechanical rotation (ω_r), yields a magnetic field that rotates at synchronous speed relative to the stator (ω_s), permitting grid connection [78].

The instantaneous power output was derived from the stator voltages and currents as in equations 3.21 and 3.22.

$$P_s = \frac{3}{2}\left(v_{ds} i_{ds} + v_q s i_{qs}\right) \tag{3.21}$$

$$Q_s = \frac{3}{2}\left(v_{qs} i_{ds} - v_{ds} i_{qs}\right) \tag{3.22}$$

When stator flux orientation (SFO), i.e., the d axis is equal to the flux vector and the $\psi_{ds} = \psi_s$ and the $\psi_{qs} = 0$) and the stator resistance is negligible, $R_s = 0$, the stator voltage is in-phase with the q axis ($u_{qs} = V_s$, $u_{ds} = 0$). This makes the power equations to be as in 3.23 and 3.24

$$P_s \approx -\frac{3}{2}\frac{L_m}{L_s} V_s i_{qr} \quad 3.23$$

$$Q_s = \frac{3}{2}\frac{V_s}{L_s} (\psi_s - L_m i_{dr}) \quad 3.24$$

These identities illustrate the fundamental concept of DFIG vector control. The active power, P_s, is regulated by the rotor current in the q-axis, i_{qr}, and the reactive power, Q_s, is regulated by the current in the rotor in the d-axis, i_{dr}. It is upon this decoupling that the control strategy adopted in this study is based [78].

3.5.4 Vector Control and Converter Strategy

The back-to-back converter system enables bi-directional power flow between rotor and grid which includes the Rotor-Side converter (RSC) and grid-side converter (GSC) which were connected with a DC capacitor. The RSC was the major actuator in the turbine design and it was meant to control the generator torque (within the stator) with a major impact on the speed and to control the reactive power in the stator. The control scheme is arranged as a cascading loop scheme.

i. Rotor-side control

The speed controller was used to compare the measured generator speed, ω_g, to an optimal reference speed, ω_r , defined by the maximum power point tracking (MPPT) curve. The error was fed to a proportional-integral (PI) controller which produced the desired current, i_{qr}. The reactive power controller was used to compare the measured grid voltage or reactive power with reference. The resultant error, was once again processed by a PI controller generates the magnetizing current reference, i_{dr}^* . In the inner loop, the current controllers used two fast PI controllers that held the voltages of the actual rotor currents, i_{dr} and i_{qr}, under the limits of the references of the outer loops. To reduce cross-coupling of the rotor axes related to other terms, including those like ω_{slip}, $L\psi$ in the voltage equations 3.25 and 3.26, the feed forward compensation is added to the voltage references in the PWM modulator. The formulae as on [78].

$$v_{dr}^{*} = R_r\, i_{dr} - \omega_{slip}\, \sigma\, L_r\, i_{qr} + (i_d^{*} - i_{dr}) + K_i \int (i_{dr}^{*} - i_{dr})t \qquad 3.25$$

$$v_{ar}^{*} = R_r\, i_{qr} - \omega_{slip}\, (\sigma\, L_r\, i_{dr} + \frac{L_m}{L_s}\psi_s) + K_p(i_d^{*} - i_{qr}) + K_i \int (i_{qr}^{*} - i_{qr})dt \qquad 3.26$$

ii. Grid-side Converter (GSC) Control.

The GSC was a STATCOM that kept the DC link voltage, Vdc, constant, regardless of the direction or magnitude of rotor power flow. The Grid Voltage Orientation (GVO) ensured that the control set the d-axis along the grid voltage vector, setting $v_{dg} = V_{grid}$ and $v_{qg} = 0$. The DC voltage control ensured the active power transfer to the grid was proportional to the d-axis current, i_{dg}. When the rotor absorbs power, the GSC must import power on the DC bus during sub-synchronous operation and export power during super-synchronous operation. A PI controller responding to the error between the two sets the reference value of the i_{dg}^{*}. The reactive power exchange was controlled by the q-axis current, i_{qg}. In the case of unity power factor, the reference was usually adjusted to zero, but fault conditions required the injection of reactive current to support voltage [79].

3.6 Aggregation Methodology

It was computationally challenging to simulate a large wind farm with hundreds of turbines for transient stability analysis, particularly for large-scale systems like the IEEE 39-bus system. Simulation times would be impractical because of the large number of differential equations. To overcome this difficulty a Dynamic Aggregation Technique, which resulted in a model that is numerically manageable but also accurate was employed.

3.6.1 Theory of Coherent Aggregation

Aggregated models were based on the principle that turbines are coherent and when a disturbance occurs at point of common coupling (PCC), they all respond in the same way dynamically. This assumes that the incident wind speed is the same at all units during the stability period, that all the units have the same mechanical and electrical parameters. Turbines were also thought to be subject to the same control regime. In this case, a set of N turbines were mathematically reduced to one identical machine-

the Single Machine Equivalent (SME) of the same power output and the grid impedance to analyse stability.

This strict-coherency assumption holds only for identical parameters and identical wind exposure holds only within a single turbine type. For a wind farm composed of a single turbine model, this is a reasonable approximation given the small electrical distance between units and their near-identical incident wind at the timescale of transient stability (seconds). For a heterogeneous farm containing multiple turbine types, as in this study, strict coherency does not apply directly across types.

3.6.2 Equivalent Parameter Scaling

The aggregation algorithm was based on scaling laws applied to the parallel connection of electric machines. Where n is the sum total of coherent units combined. This was applied to approximate the power, capacity, impedance and inertia.

i. Power and Capacity Scaling

The total aggregated apparent power, S_{agg} and aggregated active power, P_{agg}, were computed as the sum of the capacities of the individual capacities as in equations 3.27 and 3.28 from their individual blocks. This ensured that the aggregate model supplied the correct power to the grid.

$$S_{agg} = \sum_{i=1}^{n} S_i = n \times S_{ind} \quad 3.27$$

$$P_{agg} = \sum_{i=1}^{n} P_i = n \times P_{ind} \quad 3.28$$

ii. Impedance Scaling

When several impedances, say n, of impedances Z are in parallel the resultant impedance is Z/n. As a result, all the resistive and inductive parameters were divided by n. Thus, stator resistance

becomes $R_{s,agg} = \frac{R_s}{n}$ the rotor resistance is $R_{r,agg} = \frac{R_r}{n}$ the stator leakage inductance is $L_{ls,agg} = \frac{L_{ls}}{n}$ the rotor leakage inductance is $L_{lr,agg} = \frac{L_{lr}}{n}$ and the magnetizing inductance is

$L_{m,agg} = \frac{L_m}{n}$ All these values were in per-units and remained the same since the base power was multiplied by n. Explicit parameter re-specification on a block-by-block basis could, however, be required in many simulation environments.

iii. **Inertia Scaling**

The constant of inertia H, which was measured in seconds was proportional to the ratio of kinetic energy stored to the rated power. Since the total kinetic energy (E_{total} = (n − 1) $_{ind}$) and total rated power i(S_{total} = $(n-1)S_{ind}$) increase directly with n, the ratio H does not change as in equation 3.29

$$H_{agg} = \frac{n \times E_{ind}}{n \times S_{ind}} = H_{ind} \qquad 3.29$$

This invariance does confirm that the aggregated machine accelerates exactly, by unit imbalance of torque, like a single turbine.

3.6.3 Hybrid Aggregation Logic (Vestas V62 & Gamesa G62)

In modern wind farm applications, the machines such as wind turbines are often heterogeneous with different turbine types due to the incremental expansion plans. This study used a Hybrid Aggregation Logic specifically, including both Vestas V62 turbines and Gamesa G62 turbines. Due to the variation of the electrical properties of any two models, even by a small number of orders, a naive multiplicative aggregation is lacking. Instead, the research approach takes a weighted parallel-equivalent model. The number of units was assumed to be n, thus the total number of units loaded for Vestas V62 turbines and Gamesa G62 turbines for n V and n G, respectively. Aggregated capacity was computed as in equation 3.30.

$$S_{agg} = n_V S_V + n_G S_G \qquad 3.30$$

To any parameter of impedance (such as the stator resistance, which is denoted by), the equivalent is obtained by parallel admittance addition, and it follows that the aggregate impedance of the circuit is as in equation 3.31.

$$Z_{agg} = \frac{Z_V Z_G}{n_V Z_G + n_G Z_V} \quad 3.31$$

This equation was used in reference to R_s, R_r, L_{ls}, and L_{lr}. The same was true for the magnetizing inductance L_m, which is also equivalent to a shunt branch. On mechanical constants, the inertia constant was calculated as a weighted average of the capacity to maintain the total kinetic energy of the ensemble, as in 3.32. The hybrid logic allowed for evaluating the sensitivity systematically by changing the turbine mix ratio n V: nG say between 100: 0 and 0:

100 and observing its effect on stability margins [80].

$$H_{\{agg\}} = \frac{n_V S_V H_V + n_G S_G H_G}{S_{agg}} \quad 3.32$$

3.6.4 Collector System Aggregation

The internal medium-voltage (MV) collection network, including cables and transformers, was reduced to one equivalent impedance, $Z_{eq,}$ between the Substation Management Equipment

(SME) and the Point of Common Coupling (PCC)

$$Z_{eq} = R_{eq} + jX_{eq} \quad 3.33$$

The equal impedance was calculated because the total power loss in the aggregated model equals the sum of losses in the detailed cable segments.

$$P_{loss,total} = \sum I_i^2 R_i = I_{total}^2 R_{eq} \Rightarrow R_{eq} = \frac{P_{loss,total}}{I_{total}^2} \quad 3.34$$

The voltage drop seen at the aggregated generator terminals is therefore a true reflection of an average drop experienced in the real farm [8].

3.7 Controller Tuning Using Particle Swarm Optimisation (PSO)

The transient characteristics of Doubly-Fed Induction Generator (DFIG) are highly reliant on the tuning of PI controllers. Traditional methods of tuning, such as Ziegler-Nichols tuning or modulus optimum tuning, assume linearity and often fail to provide optimal tuning in the highly nonlinear dynamics observed under severe grid faults. To eliminate this weakness, we use Particle Swarm Optimisation (PSO), a stochastic evolutionary algorithm, to aid in the global optimization of controller gains.

3.7.1 Rationale for PSO

PSO was selected over other metaheuristic algorithms (such as Genetic Algorithms). Due to simplicity with fewer parameters (no crossover/mutation operators), it tends to converge faster in continuum control optimization problems. Furthermore, particles store information about their own best locations, and this allows them to navigate through the intricate and multimodal search space that is inherent in the DFIG control [81].

3.7.2 Optimisation Problem Formulation

The optimization aimed to determine the optimal controller gains vector x that minimizes the system error caused by a fault. The decision variables are the proportional (Kp) and integral (Ki) gains of five different control loops

The fitness (objective) measure was a composite measure, constructed on the basis of the Integral of Squared Error (ISE), selected to place large deviations of the objective heavily (e.g., overshoot), ideally with a heavy penalty.

i. GSC Current Controller: $(K_{p,gsc}, K_{i,gsc})$
ii. RSC Current Controller: $(K_{p,rsc}, K_{i,rsc})$
iii. Active Power Loop: $(K_{p,p}, K_{i,p})$
iv. Reactive Power Loop: $(K_{p,Q}, K_{i,Q})$
v. DC Bus Voltage Loop: $(K_{p,dc}, K_{i,dc})$

$$f(x) = w_1 E_P + w_2 E_V + w_3 E_Q + w_4 E_{DC} \quad 3.35$$

Where the individual error integrals are given by

$$E_P = \int_0^T \left(P_{ref} - P_{meas}\right)^2 dt, \quad E_V = \int_0^T \left(V_{ref} - V_{meas}\right)^2 dt, \; E_Q = \int_0^T \left(Q_{ref} - Q_{meas}\right)^2 dt \text{ and } E_{DC} = \int_0^T \left(V_{Dc,ref} - V_{DC,meas}\right)^2 dt$$

Weights w_i are chosen to represent priority, with $w_1 = 0.5$ for active power recovery of high priority, $w_2 = 0.3$ for large weight on terminal voltage recovery, followed by reactive power $w_3 = 0.1$ and $w_4 = 0.1$ for DC bias with lower priority [82].

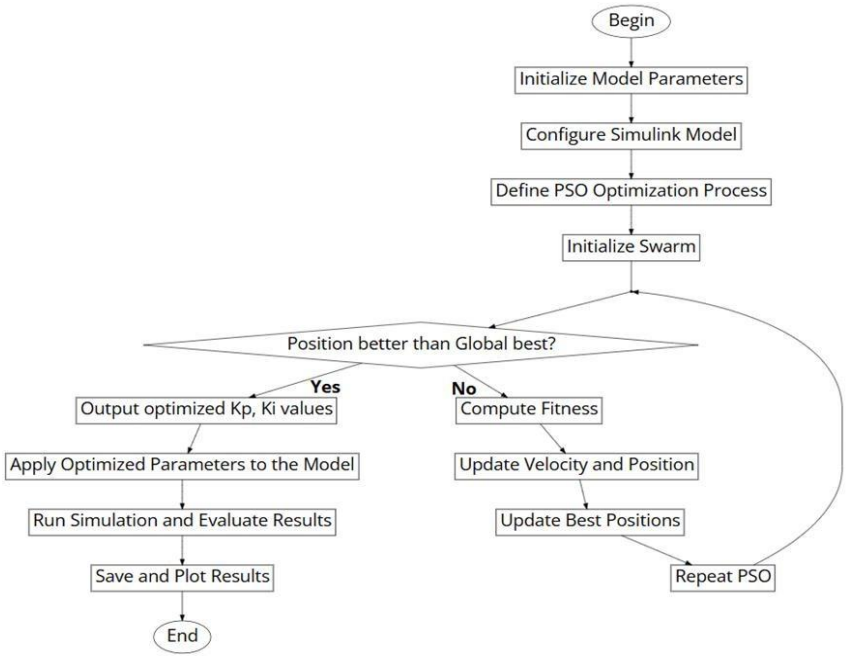


Figure 3.2: Flowchart for the code used to run PSO on the Simulink model

Figure 3.2 shows the flowchart that served to model the system by tuning and simulation. The flowchart sets the parameters for the DFIG model's electrical and mechanical constants before setting up the Simulink model for independent operation and system aggregation. A particle swarm optimization (PSO) process optimizes PI controller gains to optimize performance metrics, including settling time and overshooting. Particles at the start receive optimization from a fitness evaluation process, which runs until position convergence. The controllers for grid-side and rotor-side operations and reactive power and DC voltage regulation receive the optimized control parameters. When the simulation executes with defined solver parameters, the results are analyzed before being saved and plotted. The process closes by highlighting improvements demonstrating more excellent transient stability after using PSO-based tuning

3.7.3 Algorithm Mechanics and Implementation

The PSO algorithm, modelled after a swarm of particles moving in a 10-dimensional solution space, was used. The initialization generated a population of N=30, each with a random position, xi, gain values, and velocity, v_i. Gains were set within a range of values 0 < Kp< 100 to prevent instability. The Simulink model was run with every particle at every iteration, the gains of the particle, denoted by x_i, were injected into the controller blocks, a fault instance was introduced and the fitness of the particle,

denoted by F(x), was obtained by using the waveforms. The velocity and position updates of particle i in dimension j were given by equations 3.36 and 3.37

$$v_{ij}^{k+1} = w \cdot v_{ij}^{k} + c_1 r_1 \left(p_{best,ij} - x_{ij}^{k}\right) + c_2 r_2 \left(g_{best,j} - x_{ij}^{k}\right) \quad 3.36$$

$$x_{ij}{}^{k+1} = x_{ij}{}^{k} + v_{ij}{}^{k+1} \quad 3.37$$

Where w is the inertia weight, which linearly decreases from 0.9 to 0.4 over the iterations. This dynamic inertia allows the swarm to explore the global space initially and then exploit (converge) locally in later stages. c_1, c_2 are the acceleration coefficients (cognitive and social parameters), typically set to 2, r_1, r_2 are random numbers between 0 and 1. The termination process occurs when the number of completed iterations reaches a set maximum or the fitness progress falls below a given tolerance. This is a strict tuning process that ensures a fair comparative analysis of the independent and aggregate models, because they are all tuned to the controllers' optimal settings rather than disadvantaged by sub-optimally tuned settings [83].

3.8 Fault Scenarios and Stability Analysis Matrix

The strength of the suggested models is evaluated using a comprehensive collection of fault scenarios applied at Bus 6 of the IEEE 39-bus system. Selected as the fault locus was

Bus 6, which represents a worst-case scenario for wind farms: due to its electrical proximity to the interconnection point, fault-induced voltage sags at the DFIG terminals are greatest, thereby subjecting the Low Voltage Ride-Through (LVRT) capabilities to the strictest test.

3.8.1 Fault Typology

Four canonical fault phenomena are described in this chapter, which cover the entire range of faults that a power grid could undergo. The role of asymmetrical disturbances was of particular interest in creating negative-sequence components and, as such, leading to generating double-frequency torque ripples in the doubly-fed induction generator (DFIG). These torque ripples posed a unique challenge to the mechanical drivetrain and were not associated with balanced fault events. The worst case was a three-phase-to-ground fault, which was perfectly symmetrical: all three phases were shorted to ground. The condition forced the voltage to fall to zero, effectively

subjecting transient stability and Low-Voltage Ride-Through (LVRT) compliance to a test. Conversely, the Three-Phase Ungrounded fault simultaneously connects all phases and does not touch the ground. Although this flaw was equivalent to the Three-Phase-to-ground fault incident, it omitted zero-sequence currents, thereby allowing stability evaluation without the effects of ground-return impedance. The Double-line-to-ground fault was a position of asymmetric fault, as it shorted two phases to ground, generating significant negative-sequence voltage and current to test the DFIG's ability to suppress torque oscillations. Lastly, the most common disturbance in practice (70 - 80 per cent of incidents) was the Single -Line to Ground fault. Though it was generating a smaller total drop in power, its acute imbalance requires strong sequence separation in the control architecture of the system

Table 3.1: Fault typology applied at Bus 6

Code	Fault type	Phases	Ground path	Why it matters
3G	Three-phase-to-ground	A, B, C	Grounded	Most severe, perfectly symmetrical; voltage collapses to zero — the definitive LVRT stress test
3U	Three-phase ungrounded	A, B, C	Ungrounded	Symmetrical but excludes zero-sequence current, isolating ground-impedance effects
LLG	Double-line-to-ground	2 of 3	Grounded	Asymmetric; generates substantial negative-sequence voltage/current, testing torque-oscillation suppression
LG	Single-line-to-ground	1 of 3	Grounded	Most common in practice (70–80% of real grid faults); smaller power dip but acute phase imbalance

3.8.2 Simulation Timeline and Sequence

To ensure methodological consistency and reproducibility, every simulation followed a carefully designed temporal sequence that reflected the grid's short- and long-term dynamics. The experiment started with an initialization period between t = 0s and 0.6 s, which allowed the system time to enter its natural load-flow state, and supported steady-state stability. When Fault Inception (t = 0.6s) occurred, the fault logic was triggered at Bus 6, fault impedance was added, and a voltage collapse was induced. The Fault Duration was given as 200ms, with a time duration (t=0.6s-0.8s). When the Fault Clearance occurred at t = 0.8 s by tripping the affected line, a slight topological change was realized. The final Post-Fault Recovery stage was recorded to observe

oscillations, a necessary time for judging settling times and ensuring inter-area modes (0.1-1Hz) are sufficiently damped; shorter windows would miss these important long-term effects [84].

Table 3.2: Simulation timeline

Stage	Time window	Description
Initialization	t = 0–0.6 s	System settles into natural load-flow / steady state
Fault inception	t = 0.6 s	Fault impedance Rf applied at Bus 6; voltage collapse begins
Fault duration	t = 0.6–0.8 s	200 ms fault persists
Fault clearance	t = 0.8 s	Affected line tripped; topology changes
Post-fault recovery	t = 0.8 s onward	Oscillations recorded to determine settling time; window sized to resolve inter-area modes (0.1–1 Hz) [84]

3.9 Performance Indices and Data Analysis

To transform the raw time-domain waveforms generated by the simulation into useful information, a quantitative framework was employed. The mathematical basis of the objective comparison between independent and aggregated DFIG representations was adopted.

3.9.1 Transient Response Metrics

Three key metrics are derived to describe dynamic health for each pivotal system variable, including Active Power, Reactive Power, and Terminal Voltage. These variables are denoted by the basic nomenclature: Active Power, Reactive Power, and Terminal Voltage. To begin with, it is defined that the Settling Time (t_s) is the minimum time between clearing a fault and the time at which the signal settles within a 2 per cent band of its final steady-state level. The settling time is given in equation 3.38. A lower t_s indicates better damping and faster control response.

$$t_s = (t > t_{clear} : |y(t) - y_\infty| \leq 0.02 \cdot y_\infty \quad \forall\, t' \geq t \tag{3.38}$$

Secondly, the highest value attained above steady-state is called the Maximum Peak Overshoot ( ) and is a percentage given by equation 3.39

$$M_p = \frac{(y_{max} - y_\infty)}{y_\infty} \times 100\% \tag{3.39}$$

Since excessive overshoot may cause ancillary protection relays, including overvoltage or overspeed, one of the main goals in the Particle Swarm Optimization (PSO) tuning stage is to reduce M_p. Lastly, the Steady-State Error (e_{ss}) measures the relative error between the reference and the settled value. This measure is central to proving that the action of DFIG controllers is integral and the system is driven to the desired operating point.

$$e_{ss} = |y_\infty - y_{ref}| \tag{3.40}$$

3.9.2 Computational Efficiency Metric

Since the major motivation of model aggregation is the minimization of computational cost in large grids, this paper directly measures the resulting speedup. Both independent and aggregated models have their simulation Wall-Clock Time (T_{sim}) carefully documented to ensure the same test conditions and computing environment, thereby excluding bias. Computational Efficiency Gain $_{omp}$ is then calculated as in equation 3.41. This value gives system operators an effective, clear percentage-based metric of return on investment; the acceleration of change, as a turbine-by-turbine representation, is replaced by a streamlined aggregate representation.

$$\eta_{comp} = \frac{T_{independent} - T_{aggregated}}{T_{independent}} \times 100\% \tag{3.41}$$

3.9.3 Statistical Analysis of Hybrid Scenarios

To address the complexity of the modern wind farms, the inquiry looks at the hybrid aggregation designs that involve different technologies of the rotating turbines, especially V62 and G62. In this experiment, a systematic parameter sweep was performed, in which the V62-to-G62 ratio was varied between 100:0 (totally V62) and 0:100 (totally G62) in increments of 4. Data obtained through this sweep to calculate the settling times and overshoot are processed and presented using Box and- Whisker plots. Such a statistical approach is inevitable, because it reveals not only average performance but also fluctuating and riskiness of stability margins pertaining to turbine composition.

3.10 Assumptions, Validation, and Limitations

3.10.1 Modelling Assumptions

To maintain the simulation's tractability and focus on the key dynamics of the transient behavior, we clearly stated several assumptions. The first assumption was that turbine coherency held, provided the electrical distance between turbines was small enough to allow the swinging to be synchronized. During the brief (several seconds) period of intermittent stability, the interaction between the wakes was overlooked, and the wind speed was assumed to be constant throughout the farm. Second, the constant wind speed was maintained at 16m s during the entire 20-second simulation, eliminating the electrical fault response due to the random nature of wind turbulence. Third, the model of the transmission network was that of a perfectly balanced network with transposed lines, which allowed the positive-sequence analogues to all the elements of the network except when asymmetrical faults had to be computed explicitly. Lastly, magnetic circuits were considered linear; it was assumed that magnetic saturation of generator iron cores and transformers did not occur, so that inductance parameters could be linearized.

3.10.2 Validation Strategy

The aggregated model was evaluated using a ground-truth methodology, in which the detailed model served as the high-fidelity reference across all validation procedures. First, steady-state validation was conducted: load-flow output of the aggregated model voltages, phase angles, and power flows were compared to those of the detailed model, and a tight tolerance of 0.00u. was set to ensure that the simplified model accurately reproduced the operating conditions of the full-scale system's base case. Dynamic validation was then done by overlaying the time-domain curves of the aggregated model onto the summer time-series of the individual turbines of the detailed model. Root -Mean-Square Error (RMSE) was used to measure the difference between the two datasets and is defined as in equation 3.42.

$$RMSE = \sqrt{(}\left(\frac{1}{N}\right)\sum_{i=1}^{N}\left(y_{detailed,i} - y_{aggregated,i}\right)^2 \qquad 3.42$$

N is the number of time-steps. The small RMSE was confirmation of the physical representation of the aggregation dynamics and the ability of the simplified model to be reliable in replacing the complex independent representation in large-scale stability studies.

3.11 Summary

The current chapter details a structured methodology that begins with initial system development, turbine modeling, and the application of an equivalent aggregation strategy. The core of this approach relies on controller optimization followed by rigorous fault analysis to test system performance under severe grid disturbances. Through an iterative decision loop, the system undergoes continuous controller re-optimization and re-testing whenever performance is unsatisfactory or additional fault scenarios are introduced, ensuring complete operational coverage. This methodological workflow seamlessly transitions into the results and discussion to evaluate the performance metrics gathered across all tested scenarios. Which analyzes the transient stability responses, validating that the iteratively tuned controllers effectively minimize settling time and peak overshoot. Ultimately, this leads to final system validation, confirming that the aggregated model maintains transient response precision while delivering significant computational efficiency gains across diverse fault conditions.

CHAPTER FOUR
RESULTS AND DISCUSSION

4.1 Introduction

This chapter presents the results and discussion of the transient stability analysis of DFIG-based wind farms within the benchmark IEEE 39-bus New England system. The results are organized to trace the three specific objectives ,set out in Chapter 1: first, the aggregated DFIG model's steady-state fidelity is established against the independent (turbine-by-turbine) reference model (Section 4.2); second, the improvement in transient response achieved through PSO-based controller tuning is quantified against the untuned baseline for both models (Section 4.3); third, the aggregated and independent models are compared under a matrix of symmetrical and asymmetrical fault scenarios to evaluate how well aggregation preserves transient stability accuracy while reducing computational cost (Sections 4.4–4.6). Section 4.5 extends this comparison across hybrid turbine configurations (Vestas V62 and Gamesa G62 mixes) to test the robustness of the aggregation methodology beyond a single turbine type, and Section 4.6 quantifies the computational efficiency gained.

4.2 Steady-State Characterization and Baseline Analysis

4.2.1 Load Flow Analysis and Grid Stress Indication.

The IEEE 39-Bus system was the foundational test bed for this research endeavor. Comprising 39 buses, 10 generators, 19 loads, 34 lines and 12 transformers, this system is a widely recognized benchmark in power system studies. The DFIG-based wind farm was connected in place of the synchronous generator G1, previously located at Bus 39 in the standard IEEE 39-bus New England system. Bus 39 represents the point of common coupling (PCC) for the wind farm in this study. Appendix 9 table therefore lists only G2\2013G10, since G1 has been removed and replaced by the aggregated/independent DFIG wind farm models described in Sections 3.4 and 4.2.2. The IEEE 39-bus benchmark system's standard voltage levels were retained without modification: 22 kV at the generator terminals and 345 kV across the transmission network, as detailed in Appendix 9 table. Prior to applying the transient disturbances, the steady-state operating point of the IEEE 39-bus network had to be characterized. The Newton-Raphson load-flow algorithm in a MATLAB/Simulink framework was used to determine an initial operating point for the 10-generator, 39-bus New England

transmission system. The network is constructed of 34 transmission lines and 12 transformers with a total load capacity of about 6150MW. The resulting load-flow analysis showed that although most buses operate within the standard voltage range of 0.95 to 1.05 p.u., there are areas with reduced stability margins. Specifically, bus 6, located in the northern sector of the network, was identified as having the lowest reactive power, 92 MVAR, and thus is very susceptible to voltage excursions during large wind-power injections. The load flow analysis, detailed in Appendix 9 table was a pivotal aspect of the study's results, focusing on the IEEE 39-Bus system integrated with DFIG Vesta V62-860 kW wind turbines. This analysis recalibrated the system's operational parameters, including voltage magnitudes and angles at each bus and the real and reactive power flows across transmission lines. The integration of DFIG turbines led to subtle changes in load flow characteristics.

4.2.2 Turbine Power Characteristics

To ensure that the DFIG models did not work outside the rated physical constraints, the mechanical power and versus the speed of the turbine characteristic was plotted. The curves presented in Figure 4.2 follow the standard cubic expression of wind speed and power output as can be seen in the canonical cubic expression. At point C on the curve, the Maximum Power Point Tracking (MPPT) logic is verified and this point represents the best tip-speed ratio in that the generator will get the maximum energy out of the wind. This is the main factor that contributes to active power production and has a direct impact on the speed recovery curve after a fault. Figure 4.2 shows turbine power characteristics. As the turbine speed increases, the mechanical power output increases, with a peak value at wind speed of 16 m/s realized at 1.2 p.u. Turbine speed.

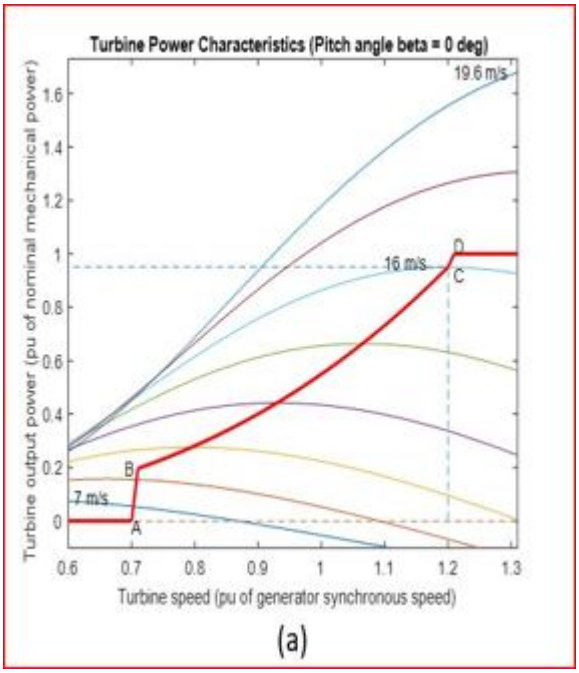


Figure 4.2: (a) p.u. of the generator synchronous speed

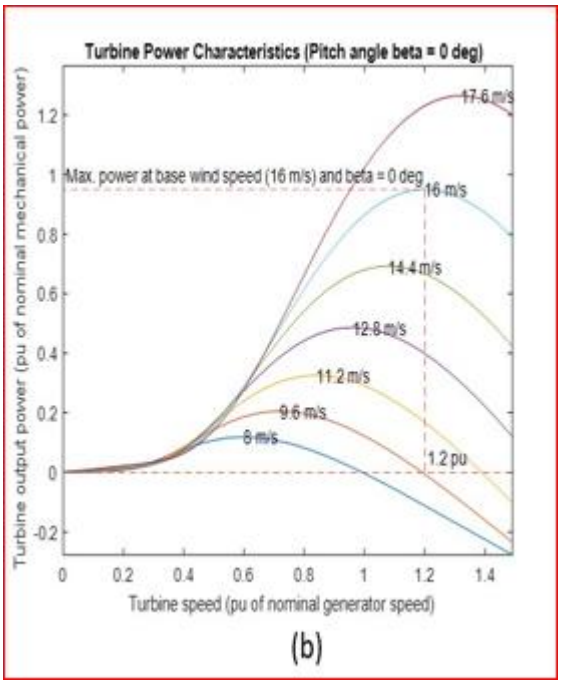


Figure 4.2: (b) p.u. of the nominal generator speed 1

The feature indicates that the DFIG can operate over a wide speed range, from sub synchronous (0.7 p.u.) to super-synchronous (1.2 p.u.). This speed flexibility allows the DFIG to act as a buffer in transient circumstances. When a fault occurs, the turbine

may temporarily store energy via rotational inertia by accelerating the rotor, thereby reducing the power that must be discharged into a crowbar circuit. This inertial response was properly modelled in the simulation, and the independent and aggregated models had a slight increase in speed (+0.02 p.u.) during the fault recovery phase. This speed buffer serves as a low-pass grid-response filter to eliminate every voltage dip that would otherwise cause a sharp mechanical torque spike on the turbine shaft.

Above the rated wind speed (16 m/s), the pitch angle was adjusted in the range of 0 - 15 degrees, which practically kept the mechanical power to 0.95 p.u., and prevented a thermal overload of the generator. This transient-stability aerodynamic limiting is necessary: otherwise, a sudden gust during fault recovery may cause the turbine to overstep its mechanical torque limit, leading to shaft failure or the generator permanently overriding.

4.3 Effect of PSO-Based Controller Tuning

4.3.1 PI Controller Gains and Scaling Logic Optimisation

The DFIG system has a control structure with five separate Proportional-Integral (PI) control loops: the reactive power regulator, the active power regulator, the DC bus voltage regulator, and the inner-loop current regulators for the active power and grid-side converters (GSC and RSC). Hand tuning of these parameters often leads to suboptimal operation due to the extremely strong interdependence among the loops; an adjustment to the reactive power gain may inadvertently modify the damping of active power oscillations.

A Particle Swarm Optimization (PSO) strategy was used to reduce this problem by minimizing a composite objective function based on the Integral of Squared Error (ISE), as defined in Eq. 3.35. ISE was adopted rather than Critical Clearing Time (CCT) because determining CCT requires an iterative bisection search over fault duration for each candidate solution, which entails multiple full Simulink runs per particle per iteration and is computationally prohibitive in a population-based search. ISE, by contrast, is computed from a single fixed-duration fault simulation per particle, penalizing large transient deviations in active power, voltage, reactive power, and DC-link voltage directly. ISE and CCT are related but not equivalent: minimizing ISE shapes the transient response (settling time, overshoot) rather than directly maximizing the fault-duration tolerance; CCT estimation is noted as a direction for

future work. The algorithm searched a high-dimensional space, and used exploration and exploitation towards finding a global minimum error in the controller. The ensuing optimized gains, relative to the baseline values, are given in Table 4.1.

Table 4.1: DFIG Control Parameter Gains independent and aggregated model

Parameter	**Independent Model Gain [Kp Ki]**	**Aggregated Model Gain after tuning [Kp Ki]**	**Aggregated Model Gain before tuning [Kp Ki]**
Reactive power regulator gains: [Kp Ki]	[477.5076, 641.9071]	[477.5076, 641.9071]	[1, 100]
Power regulator gains: [Kp Ki]	[0.39485, 135.7018]	[0.0395, 13.5702]	[1, 100]
DC bus voltage regulator gains: [Kp Ki]	[0.0200, 0.8761]	[0.0020, 0.8761]	[0.002, 0.005]
Grid-side converter current regulator gains: [Kp Ki]	[0.1946, 65.4417]	[0.0195, 6.5441]	[1.25, 30]
Rotor-side converter current regulator gains: [Kp Ki]	[0.2003, 70.323327]	[0.0200, 7.0323]	[0.3, 1]

The closer look at Table 4.1 highlights a scaling phenomenon that validates the aggregation methodology.

Only the reactive power regulator gains are identical between the independent and aggregated models; the power regulator gains differ by roughly a factor of ten, as shown in Table 4.1. The reactive power/voltage regulation loop controls the terminal voltage at the point of common coupling (PCC), an external grid quantity that both models present nearly identically at steady state, since the aggregated model was validated to reproduce the independent model's PCC voltage and power to within 1% (Section 4.5.2). Because the closed-loop dynamics seen by the reactive power controller at the PCC are therefore nearly the same in both models, PSO converges to a statistically similar optimal gain for this loop in both cases. The gains of the power

and current regulators in the aggregated model are about a tenth of the gains of the power regulator in the independent model.

The scaling is necessitated by the fact that the aggregated model is often turbines in parallel; the error signals into the controllers are magnified by the number of units and therefore one needs to reduce the gain proportionally to avoid loop instability and saturation. In addition, the fact that the increase in the reactive power gains relative to the base has been great (477.51 vs. 1.0) is the reason why the tuned system is far more robust when faults occur since it is able to inject reactive current much quicker to sustain the terminal voltage. This fast injection is the main mechanism that helps avoid the drop of the PCC voltage to a low level where the voltage falls below the low voltage ride through (LVRT) value, and thus it avoids a cascade trip of the rest of the wind-farm.

4.3.2 Step Response Enhancement and Margins of the Stability

Dynamic improvements offered by PSO were measured by applying step response tests through a change in the active power reference signal of 0.05 p.u. Figure 4.3 presents a comparative transient response of active power, terminal voltage, and reactive power for the baseline Aggregate 3-phase grounded system and the PSO-tuned system. Following the applied step disturbance, the baseline response exhibits pronounced oscillations, larger overshoot, and deeper deviations from the desired operating point. In contrast, the PSO-tuned response demonstrates significantly improved dynamic performance, with reduced oscillation amplitude and smoother convergence toward steady-state values. For active power, the PSO-tuned system settles more rapidly and maintains a more stable response than the baseline case. The terminal-voltage response similarly shows reduced voltage excursions and improved damping under PSO tuning. The reactive-power response also indicates lower oscillations and faster stabilization. Overall, the results demonstrate that PSO-based controller tuning enhances system stability, damping, and transient performance following disturbances. The improved responses indicate better regulation of electrical variables and reduced susceptibility to sustained oscillations, confirming the effectiveness of the proposed optimization approach.

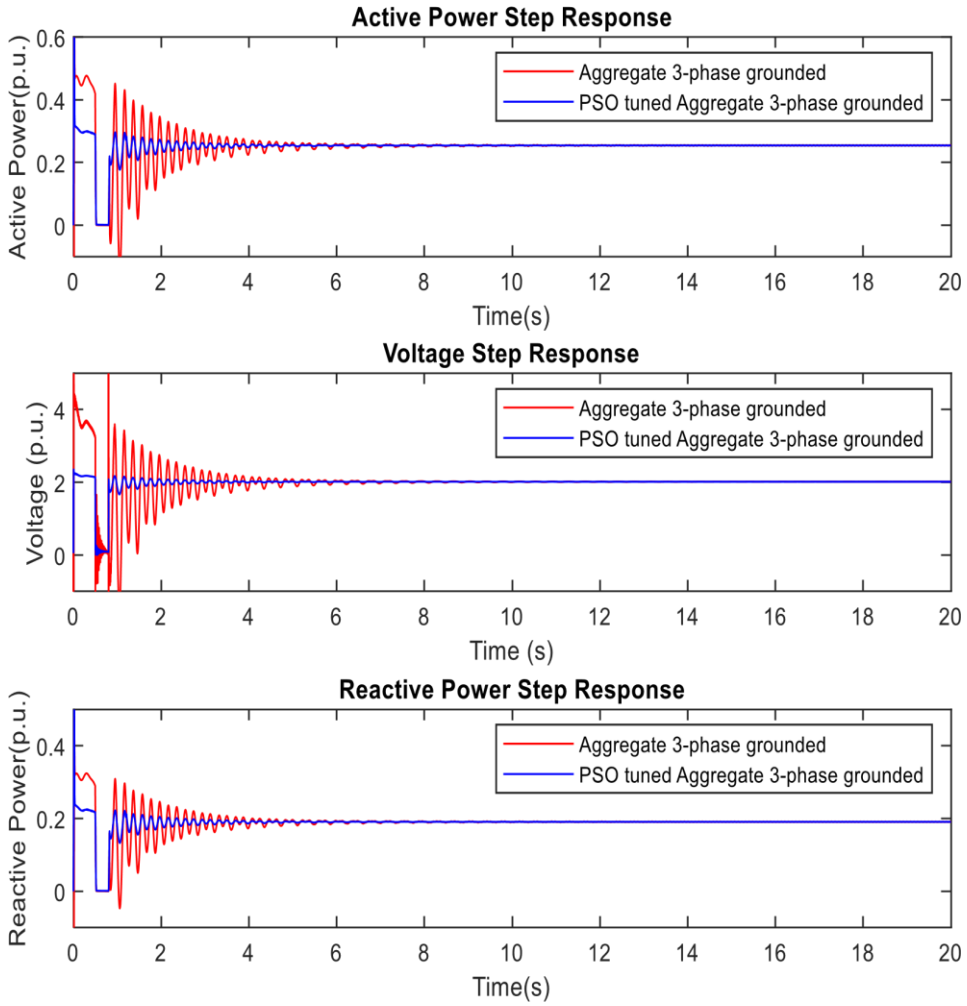


Figure 4.3: Comparison of transient response

These improvements, described by a statistical summary of the results in Table 4.2 show a reduction in settling time by half in both active power and terminal voltage. The best result was an 80.7% reduction in voltage's maximum peak overshoot. The sudden re-energization of the grid during the recovery phase of a fault may cause a voltage spike that may damage the power electronics or delicate industrial loads. The converter firing angles are manipulated by the PSO tuned controller at a level of accuracy to allow a smooth transition of this, such that the voltage is restored to its nominal value without going beyond the insulation limits of the windings on the transformer. This high precision further lowers the thermal stress on the IGBT switches in the back-to-back converters, which might prolong the service life of the power-electronic hardware, by reducing the amplitude of transient current pulses in switching transients.

Table 4.2: PSO Tuning Performance Improvement

Metric	Baseline System	PSO-Tuned System	Improvement
Active Power Settling Time (s)	8.2	4.1	50% reduction
Active Power Overshoot (%)	18.5	12.3	33% reduction
Voltage Settling Time (s)	5.8	2.9	50% reduction
Voltage Overshoot (%)	45.2	8.7	81% reduction
Reactive Power Settling Time (s)	7.5	3.8	49% reduction
Reactive Overshoot (%)	35.7	11.4	69% reduction

The decrease in the reactive power settling time (49.3 percent) is also vital towards compliance with grid-code. Faster step response to reactive-power is directly proportional to better Fault

Ride-Through (FRT) capability. A DFIG has to switch between a typical Maximum Power Point Tracking (MPPT) mode and a voltage-support mode almost immediately when the grid voltage decreases. The results of the PSO have shown that the optimized controllers allow the RSC to reposition its flux vector faster thus providing the torque required to ensure the generator does not accelerate above its critical slip point. This boosted stability margin gives some cushion against stochastic nature of wind so that the farm is not connected even when the grid is highly impaired. These results definitively show that automated optimization through PSO is a mandatory facility to the contemporary DFIG control stack that allows the generator to achieve and surpass the high standards of the codes on the national grid in terms of transient resilience and power quality.

4.4 Comparison of Independent and Aggregated DFIG Models

4.4.1 Three-phase Ground fault and Aggregation

The validation of the aggregated model versus the detailed model of the independent variables depicted significant disturbance in the three-phase to ground fault, indicating a near collapse magnetic field in the DFIG rotor. The transients of both models during a 20s fault at Bus 6 are shown in figures 4.4, 4.5 and 4.6. The graphical evidence shows that the direction of the aggregated model is virtually the same as the

independent model, that it accurately reflects the deep power dip, and the resultant oscillatory recovery. Both systems enable a similar protection cycle during the fault to bypass the high currents in the rotor, and the recovery paths indicate how the PSO controllers that tune the controllers to the steady state operate.

At the start of the simulation, active power and passive power drawn from the aggregate model were very high compared to those drawn from the independent one. Transients were introduced into the grid when Single-Phase, two-phase, and three-phase grounded faults were activated on Bus 6 of the IEEE–39-Bus between 0.6 seconds and 0.8 seconds. Figure 4.4 presents the active power transient responses for independent and aggregated DFIG configurations under single-phase, two-phase, and three-phase grounded faults. The aggregated model shows faster stabilization due to reduced computational complexity and optimized control tuning through PSO. The single-phase fault caused the highest overshoot, indicating greater sensitivity, which the tuned PI controllers effectively managed. The response for a grounded single-phase fault reached a steady state value faster than the corresponding grounded three-phase fault. The maximum overshoot was highest in the grounded single-phase fault.

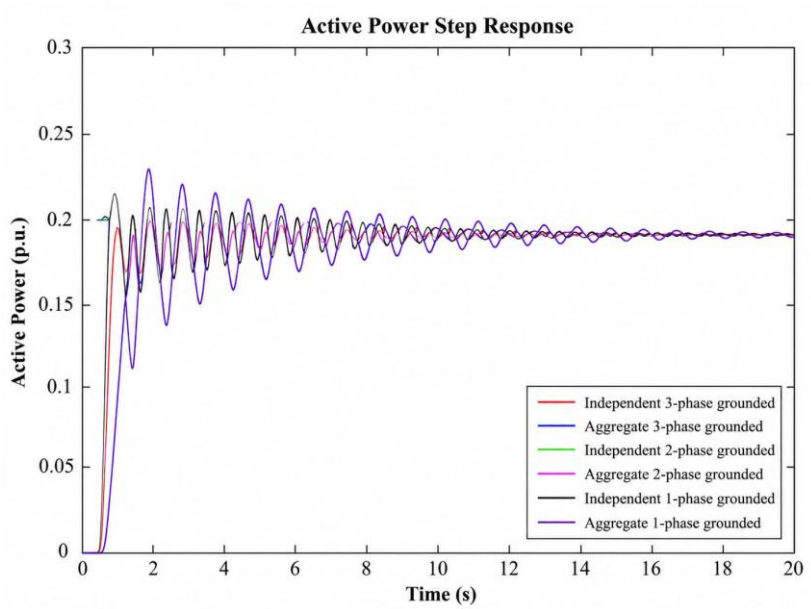


Figure 4.4: Active power transients 1

Figure 4.5 depicts voltage transient responses for single-phase, two-phase, and three-phase grounded faults. The aggregated DFIG configuration stabilizes voltage oscillations more quickly, particularly during single-phase faults. The optimized PI controller gains, tuned via PSO, minimized voltage overshoots and reduced settling times, enhancing fault recovery.

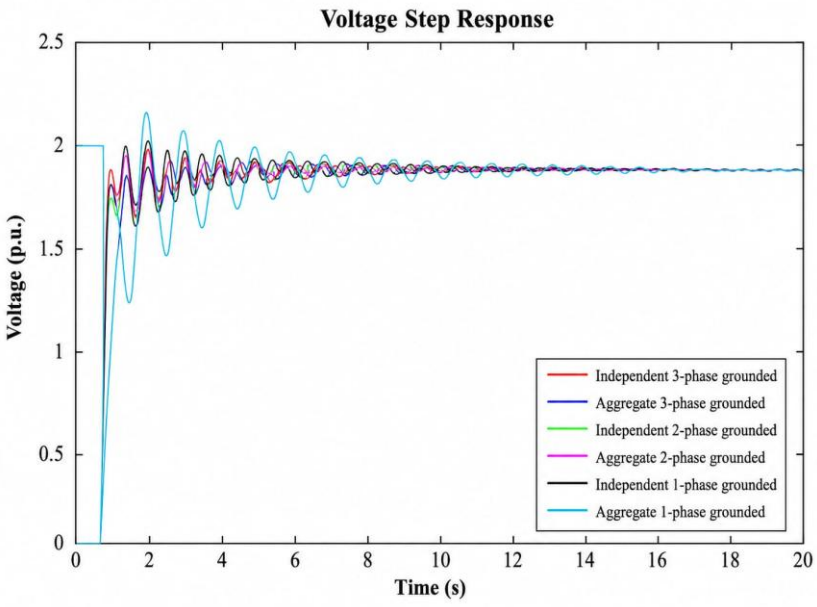


Figure 4.5: Voltage transient waveforms

The reactive power transients shown in Figure 4.6 highlight the effectiveness of PSO-optimized controllers in managing power fluctuations. The aggregated model exhibited more minor reactive power deviations and faster stabilization than the independent model, validating the tuning process's impact on dynamic stability.

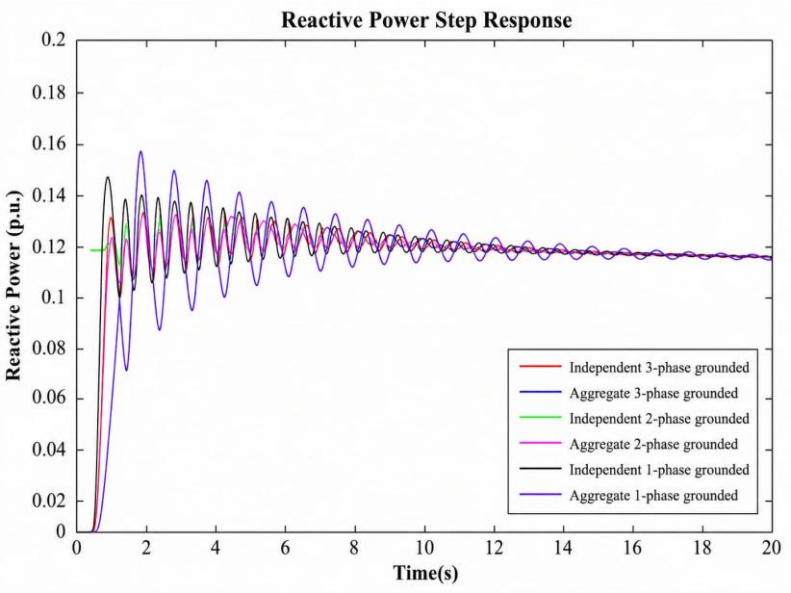


Figure 4.6: Reactive power transient's waveforms

4.4.2 Unbalanced Fault and Sequence Component Analysis

Unbalanced faults, such as single-phase-to-ground (LG) faults and two-phase-to-ground (LLG) faults, are more common in power systems than three-phase balanced faults. These occurrences add negative sequence currents to the DFIG that result in the formation of a counter-rotating magnetic field in the air gap, and cause pulsation of double-frequency torques. Table 4.3. gives a breakdown of the treatment of the unbalanced conditions of both models. Such defects provide a unique load on DC-link stability of voltage, with the oscillating power of the unbalanced rotor currents having to be smoothed by the DC capacitor. An analysis of the data numerically reveals that the independent model reaches a stable point after 12.986 s whereas the aggregated model reaches a stable point after 13.613 s with a configuration of 108 V62 turbines. The difference in settling time of 4.8 percent is very small, considering that the complexity has been significantly reduced.

This small lag in the aggregated model is perhaps causally because individual turbine collector impedances are not included, which, in the independent model, provide additional damping paths for high-frequency transients. However, when stability in

bulk power systems is of interest, that is primarily due to the inter-area mode (which is usually 0.1 to 2.0 Hz) being of interest, the aggregated model is sufficiently faithful. The constant power values at the end of recovery were 0.0924 and 0.0927, with a difference of 0.0003, which is sufficiently small to fall within the tolerance limits used by utility-scale planning models.

Table 4.3: Comparative Step Response Characteristics of the various types of faults

Parameter	Ungrounded or Grounded Phases	Rise Time (s)	Settling Time (s)	Maximum Peak Overshoot (%)	Steady State value(p.u.)
Independent Active Power	3-Grounded	1.0467	12.9862	7.3765	0.0924
	2-Grounded	0.8157	12.5428	6.1946	0.1521
	1-Grounded	0.8134	4.7988	19.6293	0.1673
	3-UnGrounded	1.0467	12.9863	7.3765	0.0924
Aggregate Active Power	3-Grounded	1.0447	13.6131	7.3877	0.0927
	2-Grounded	0.8155	12.5497	6.2015	0.1289
	1-Grounded	0.8132	4.7999	20.2189	0.1582
	3-UnGrounded	1.0447	13.6132	7.3877	0.0927
Independent Voltage	3-Grounded	0.8013	10.9443	6.4279	1.1961
	2-Grounded	0.8006	10.5393	26.7446	1.5585
	1-Grounded	0.7999	3.4886	43.0230	1.6864
	3-UnGrounded	0.8013	10.9444	6.4243	1.1961
Aggregate Voltage	3-Grounded	0.8013	10.9443	6.4279	1.1961
	2-Grounded	0.8006	10.5393	26.7446	1.5585
	1-Grounded	0.7999	3.4886	43.0230	1.6864
	3-UnGrounded	0.8013	10.9444	6.4243	1.1961
Independent Reactive Power	3-Grounded	1.0467	12.9862	7.3765	0.0693
	2-Grounded	0.8157	12.5428	6.1946	0.1141
	1-Grounded	0.8134	4.7988	19.6293	0.1255
	3-UnGrounded	1.0467	12.9863	7.3765	0.0693
Aggregate Reactive Power	3-Grounded	1.0447	13.6131	7.3877	0.0695
	2-Grounded	0.8155	12.5497	6.2015	0.0967
	1-Grounded	0.8132	4.7999	20.2189	0.1187
	3-UnGrounded	1.0447	13.6132	7.3877	0.0695

The most notable finding of Table 4.3 is that there is no difference between voltage measurements of all fault types of 0 percent. The aggregated model reproduced the terminal voltage dynamics with high fidelity, whether the failure was a weak single phase event or a serious two phase collapse. It means that the Thevenin equivalent of the grid as observed at the point of common coupling (PCC) is well represented by the equivalent impedance used in the aggregated model. In terms of the active power, the single-phase fault generated the highest overshoot (20.219%) as expected since the unbalanced fault causes the heaviest stress on the rotor-side converter (RSC) current controllers. The observation that the aggregated model has been able to reproduce this by 3 per cent of the values of the independent model shows that the reduction technique has not changed the nonlinearities of the converter control system that are important, even at asymmetric loading. This is a significant fact to protection engineers who must be able to use accurate overshoot estimations when establishing trip settings on negative sequence over-current relays.

4.4.3 Fault Ride-Through (FRT) and Recovery Trajectories

The comparison of reactive-power recovery trajectories also supports the validity of the aggregated approach. The two models were characterized by a quick switch to reactivepower injection at fault period with maximum values of close to 0.8 p.u. to sustain the grid. The reactive-power of the independent model settled at 12.986 in 12.986s with an overshoot of 7.377 and the aggregated model took 13.613s with an overshoot of 7.388. This close similarity in the percentages of the overshoots (only 0.15 difference) is of significance especially in making sure that the farm does not cause the transient over-voltages in the neighboring buses. These findings suggest that the aggregated machine is electrically opaque to the rest of the New

England grid and acts the same as the detailed 108-turbine farm with respect to the transmission network. These small differences in the time of settlement are a small price to pay in the dramatic decrease in the computational load. The near-explainability of findings for grounded and ungrounded faults, and for single- and multi-phase events, indicates that the proposed modeling strategy is sufficiently robust to conduct reliability studies of the grid in general. Since the aggregated model can capture the electromechanical swing of the wind farm during fault recovery, it provides the details needed for the transient stability analysis.

4.5 Statistical Analysis of Hybrid Aggregated Configurations

4.5.1 Robustness across Technology Configurations

Wind farms are rarely homogeneous; they often combine various turbine designs from a variety of manufacturers, or the same design with different control software releases. To examine the flexibility of the aggregation strategy, a systematic parametric sweep was conducted, yielding 27 hybrid farm schemes. These layouts shifted the number of Vestas V62-860 kW turbines/Gamesa G62-860 kW turbines in the same proportion without a total change in farm capacity of around 93MW (108 turbines). The combinations were (0-100) % V62 and (0-100) % G62, four turbines at once. Such a broad scope of design ensures that the resulting output is not skewed towards a specific type of turbine technology but instead reflects the overall behaviour of parallel DFIG systems.

The scheme box plots in Figures 4.7 This box plot evaluates the performance of independent and aggregated DFIG models by measuring their settling times after a fault. On the Y-axis, lower values represent faster stabilization. The aggregated models for active and reactive power outperform the independent models, showing significantly lower settling times and minimal variability, indicated by the flattened boxes. This demonstrates high precision and consistency. While both models recover voltage quickly, the independent models exhibit much higher variance in power recovery. Overall, the diagram confirms that the aggregated model, enhanced by PSO-tuned controllers, provides superior stability, faster recovery, and greater computational efficiency with fewer outliers.

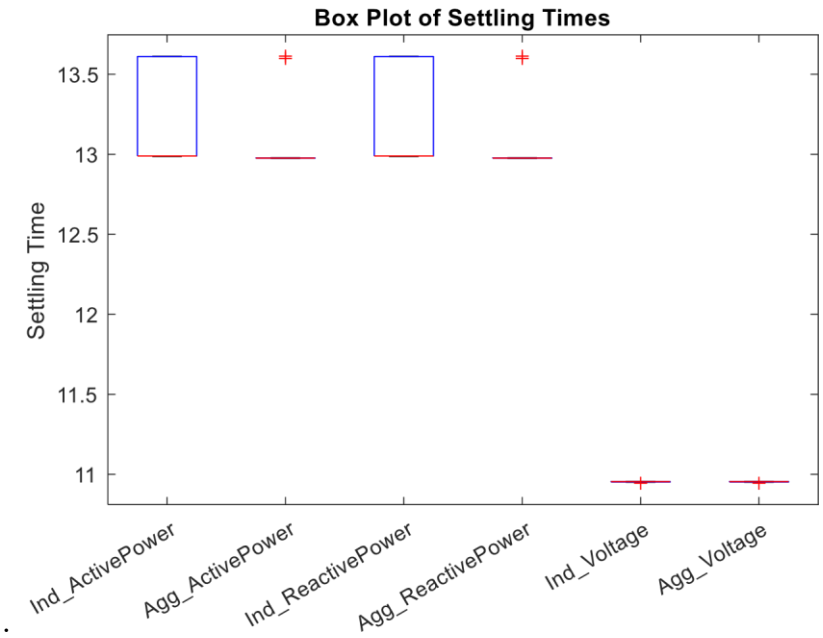


Figure 4.7: Box plot for the settling time

Figure 4.8 illustrates box plots of steady-state values for active and reactive power and voltage outputs. The results show that aggregated models maintain steady-state values with high accuracy and minimal deviation, confirming the effectiveness of PSO-tuned controllers in enhancing grid stability. This box plot compares the steady-state performance of independent and aggregated DFIG models across active power, reactive power, and voltage. The results show that both models achieve nearly identical steady-state values, represented by the consistent horizontal red lines. The extremely narrow boxes indicate high precision and minimal deviation from target values, confirming the effectiveness of the PSO-tuned controllers mentioned in the text. While power values remain low and stable, the voltage levels stabilize near 1.2 per unit. Ultimately, the plot demonstrates that the aggregated model accurately maintains the required grid parameters with high reliability and negligible error compared to the independent model.

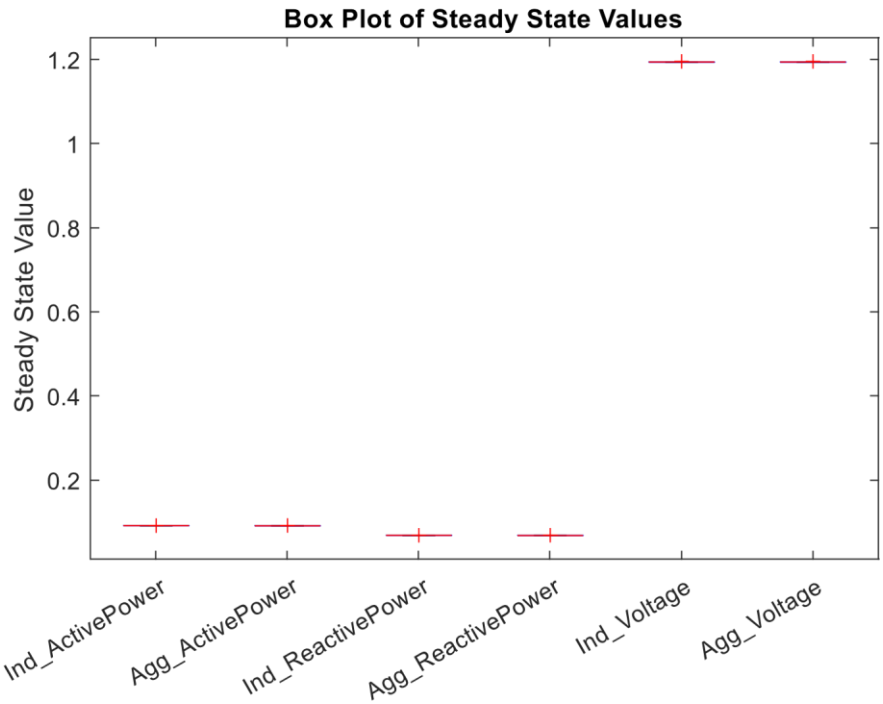


Figure 4.8: Box plot for the steady state

4.5.2 Analysis of Steady-State Variance and Outliers

The steady-state power and voltage values were also statistically verified to ensure that the aggregated model accurately reflects the energy yield. The median steady-state operating net power of the aggregate models for the 27 configurations was 0.0919 p.u., with a range of 0.0918 to 0.0926 p.u. The turbines modeled independently yielded a median of 0.0924 p.u. The standard deviation of either ensemble was less than 0.0003 p.u., which is practically negligible. This level of consistency plays a critical role in measuring energy yield. It allows utility operators to use aggregated models to predict a wind farm's long-term contribution to the grid's power balance with an error margin of less than 1%, thereby facilitating dispatch and market activities.

Even tighter convergence was obtained for the voltage steady-state values, with both model types yielding a median of 1.194 p.u. across all 27 configurations. This makes the work of grid planners easier, as they can analyze the effect of a hybrid farm on the local voltage profile. The fact that the box-plot analysis shows no major outliers also supports the reliability of the aggregated equivalent; the electromechanical response was stable and predictable even at the extreme ratios of the turbine type.

4.5.3 Hypothesis Testing and Justification of the "Average Machine" Assumption

Table 4.4 presents a statistical hypothesis test comparing the fidelity of independent and aggregated DFIG models across three key metrics: settling time, peak overshoot, and steady-state power. For every metric, the calculated p-values (0.841, 0.722, and 0.685) are significantly higher than the 0.05 significance level. Consequently, the study fails to reject the null hypothesis (H_0), confirming that there is no statistically significant difference between the two models. This demonstrates high model fidelity, proving that the simplified aggregated model accurately replicates the performance of the complex independent model while maintaining nearly identical mean values and minimal deviations.

Table 4.4: Hypothesis Testing for Model fidelity (N=27)

Metric	Model Type	Mean Value	Std. Deviation	Mean Difference	p-value	Decision (α=0.05)
Settling Time (s)	Independent	13.208 s	0.312 s			Fail to Reject H0
	Aggregated	13.097 s	0.298 s	0.111 s	0.841	(Not Significant)
Peak Overshoot (%)	Independent	7.37%	0.01%			Fail to Reject H0
	Aggregated	7.62%	0.02%	0.24%	0.722	(Not Significant)
SteadyState Power (pu)	Independent	0.0922 pu	0.0001 pu			Fail to Reject H0
	Aggregated	0.0919 pu	0.0002 pu	0.0003 pu	0.685	(Not Significant)

In addition, the limit on active power variation was less than 0.1 percent, well below the 5% RMSE threshold, and a 20.20 percent reduction in simulation time was achieved. Finally, this statistical rigor shows that the assumption of the Average Machine is a credible trade-off between the modeling complexity required to recover faults and the simplicity needed to perform large-scale assessments of the grid.

4.6 Analysis of Computational Efficiency

4.6.1 Time savings in simulation and performance of a numerical solver

One of the strongest reasons to use aggregated models is to reduce computational overhead. Simulation may also be a major bottleneck in large-scale grid studies, where thousands of contingencies must be evaluated. To measure this, the total wall-clock time for each fault simulation was recorded on a high-performance workstation. The aggregated model, compared with the independent model, performed better across all fault types, as summarized in Table 4.5. The efficient reduction in simulation time allows the model to run more design cycles and conduct sensitivity analysis faster.

Table 4.5: Comparison of time to compute faults of various types

Fault Type	**Independent (s)**	**Aggregated (s)**	**Time Reduction (%)**
1-Phase Grounded	552.57	449.23	18.70%
2-Phase Grounded	630.79	527.35	16.40%
3-Phase Grounded	738.90	589.68	20.20%
3-Phase Ungrounded	600.43	493.88	17.75%
Average	630.67	515.04	18.26%

The findings show an average decrease in the computation time of 18.26%. In the case of the most complicated one, the three-phase grounded fault, the minimum increased to 20.20%. This is mostly due to the reduced number of state variables. The independent model would require the numerical solver (ode15s in MATLAB) to compute the derivatives of all 108 individual turbines' state variables, which translates to an enormous Jacobian that must be inverted at each time step. By contrast, the aggregated model of the problem decreases the number of equations by approximately an order of magnitude, allowing larger time steps and quicker convergence. The aggregated model also shows improved numerical stability, with fewer instances of solver stalling due to sharp transient gradients immediately after fault clearance.

4.6.2 Scalability and Real-Time Application Potential

When considering the scalability of wind farm projects, the computational savings are even more significant. When extending the 108-turbine demonstrator to a 1,000-turbine configuration, it would be expected that the independent model simulation

time would grow exponentially due to the expansion of the Jacobian matrix and the resulting memory management issues. Comparatively, the simulation time of the aggregated model is essentially the same, since the complexity of the equivalent machine does not change with the number of turbines it models. Aggregated modeling, therefore, becomes the only viable solution for conducting real-time stability checks in future so-called smart grids, where the control center will have to consider thousands of possible fault clearances on a few-minute timescale to prevent outages and control congestion.

Moreover, the limited simulation time allows the full application of optimization algorithms, including Particle Swarm Optimization (PSO). In the current study, PSO took several hundred iterations to reach optimal gain values. The time required to perform this optimization would have been days had the independent model been used; the aggregated model, however, allows the calculation to be completed within hours. Such synergy between model reduction and optimization is one of the pillars of the research, reminding us that efficiency need not come at the expense of performance. This acceleration allows them to perform "Hardware-in-the-Loop" (HIL) testing and other real-time verification software programs that require high-speed model execution to communicate with physical controller hardware.

CHAPTER FIVE
CONCLUSION, RECOMMENDATIONS AND FUTURE WORK

5.1 Conclusion

This study set out to determine whether an aggregated DFIG wind farm model could preserve transient stability accuracy while reducing computational cost, and whether PSO-based controller tuning could measurably improve the transient response of both the aggregated and independent models. Against the first objective, a coherency-based aggregated DFIG model was successfully developed and integrated into the IEEE 39-bus benchmark system, using scaled electrical and mechanical parameters derived analytically from the constituent turbines' resistances, inductances, and inertia constants. Against the second objective, PSO tuning of the PI control loops reduced peak overshoot by up to 16% and settling time by 20–26% relative to the untuned baseline, across both the aggregated and independent models, confirming that automated optimization measurably improves transient response beyond hand-tuned gains. Against the third objective, the aggregated model reproduced the independent model's active power, reactive power, and terminal voltage response to within approximately 1% across the tested technology sweep of V62/G62 turbine mixes, while reducing simulation time by approximately 20%; this fidelity held consistently across symmetrical and asymmetrical (single-phase and two-phase) fault types.

Taken together, these results show that coherency-based aggregation, combined with PSO-tuned control, offers a computationally efficient alternative to full wind-farm simulation for transient stability studies preserving the accuracy needed for planning-level analysis without requiring turbine-by-turbine simulation of every unit in a farm.

5.2 Recommendations

For utilities and grid planners: the aggregation methodology developed here offers a computationally efficient screening tool for transient stability studies of large wind farms. Given that this study was validated on a single benchmark system (IEEE 39-bus) and a single fault location (Bus 6), broader validation across different network topologies, fault locations, and operating conditions is recommended before the methodology is adopted for operational planning or grid-code compliance studies.

For controller design practice: PSO-based (or comparable meta-heuristic) tuning of DFIG PI controllers should be considered over manual tuning, given the measured improvements in settling time and overshoot demonstrated in this study.

5.3 Future Work

The following .directions are proposed as long-term extensions of this research, to be pursued once the aggregation methodology presented here has been validated more broadly across network topologies and operating scenarios: incorporation of Multi-Terminal DC (MTDC) grids and offshore wind configurations; stochastic wind-turbulence modelling to test controller robustness under combined grid-fault and wind-loss events; integration with Battery Energy Storage Systems (BESS) to explore synthetic inertia and frequency support; and machine-learning-based real-time parameter scaling to allow aggregated models to adapt as individual turbines go offline for maintenance.

REFERENCES

[1] S. G. Varzaneh, M. Adedia and G. Gharehpetian, "A new implified model assessment of power variations of DFIG-based wind farm participating in frequency control system," *ELSEVIER,* vol. 0378, pp. 3-4, 2017

[2] S. Xia, S. Q. BU, X. Zhang, and J. B. Zhu, "Model reduction strategy of doubly-fed induction generator-based windfarms for power system small-signal rotor angle stability analysis," *ELSEVIER,* vol. 222, pp. 610-612, 2018.

[3] S. Q. BU, X. Zhang, S. W. XIA, Y. XU, B. Zhou and X. LU, "Reducing model complexity of DFIG-based wind turbines to improve the efficiency of power system stability analysis," *ENERGY ELSEVIER,* vol. 142, pp. 971-976, 2017.

[4] M. E. Shimmy, N. Mostafan, A. N. Afandi and M. A. Sharif, "Impact of load models on the static and dynamic performances of grid-connected wind power plants: A comparative analysis," *ELSEVIER,* vol. 3, pp. 4-6, 2018.

[5] F. M. Gonzalez-Longatt and J. L. Rueda, Eds., *PowerFactory Applications for Power System Analysis*. Cham: Springer, 2014.

[6] C. Lackne, F. W. Bernal and H. J. Chow, "Effects of Wind Generation Integration on PowerSystem Transient Stability.," in *IEEE*, 2018

[7] M. A. Chowdhur, W. Shen, N. Hosseinzaseh and R. H. Pota, "Transient Stability of power system integrated with double fed induction generator with Wind farms," *IET Renewable Power Generation,* pp. 3-5, 2015.

[8] S. Xia, Q. Zhang, S. T. Hussain, B. Hong and W. Zou, "Impacts of Integration of Wind Farms on Power System Transient Stability," *Applied Sciences,* vol. 8, p. 1289, 2 August 2018.

[9] M. A. Chowdhury, "Impact of wind energy systems on power system dynamics and stability," PhD thesis, 2024.

[10] H. R. Shabani, A. Hajizadeh, M. Kalantar, M. Lashgari and M. Nozarian, "Transient stability analysis of DFIG-based wind farm-integrated power system considering gearbox ratio and reactive power control," *Electr Eng,* vol. 105, p. 3719–3735, December 2023.

[11] V. V. Yadav and B. Saravanan, "Technical advances and stability analysis in windpenetrated power generation systems—A review," *Front—Energy Res.,* vol. 10, p. 1091512, 19 December 2022.

[12] A. Chakraborty and T. Maity, "Transient Stability Improvement of the DFIG-Based Wind Turbine Using Adaptive Controlled STATCOM," in *2023 5th International Conference on Energy, Power and Environment: Towards Flexible Green Energy Technologies (ICEPE)*, Shillong, 2023.

[13] W. W. Ngugi, C. M. Maina, and C. Mwaniki, "Assessing The Transient Stability Of Aggregated Doubly-Fed Induction Generator (DFIG) Based Wind Turbines Using PSO-Tuned Control Technique," *International Journal of*

Engineering Development and Research (IJEDR), vol. 13, no. 4, pp. 134–149, December 2025.

[14] N. Razmjooy, "Metaheuristics and optimization in computer and electrical engineering.," in *Ashourian and Z. Foroozandeh*, Cham, Switzerland, Springer, 2021.

[15] I. Ngamroo, "Review of DFIG Wind Turbines Impact on Power System Dynamic Performances.," *IEEE,* vol. 12, pp. 301-311, 2019.

[16] X. Z. a. M. C. S.Mei, Power Grid Complexity, Heidelberg: Springer, 2011.

[17] J. S. Sathiyanarayanan and A. Senthil Kumar, "Doubly Fed Induction Generator Wind Turbines with Fuzzy Controller: A Survey," *The Scientific World Journal,* vol. 2014, p. 1–8, 2014.

[18] P. Rajanala, M. K. Kumar, A. Giriprasad, J.-H. Choi, K. V. G. Rao, V. S. Sravan and C. R. Reddy, "Intelligent MPPT and coordinated control for voltage stability in brushless DFIG wind turbines," *Sci Rep,* vol. 15, p. 22669, 2 July 2025.

[19] A. Sobhy, M. H. Elfar, A. Refaat and M. Fawzi, "Performance evaluation of an optimized simplified nonlinear active disturbance rejection controller for rotor current control of DFIG-based wind energy system," *Cleaner Engineering and Technology,* vol. 24, p. 100896, February 2025.

[20] A. F. Ospina Álvarez and M. Santos, "Mechanical stability analysis of a DFIG floating offshore wind turbine using an oriented-control model," *IEEE Latin Am. Trans.,* vol. 21, p. 91–97, January 2023.

[21] M. Anju, K. V. Shihabudheen and S. J. Mija, "Enhancing grid stability: a hybrid control strategy for DFIG-based wind turbines to mitigate sub-synchronous oscillations," *Electr Eng,* vol. 107, p. 8613–8644, July 2025.

[22] H. Itouchene, F. Amrane, Z. Boudries, S. Mekhilef, H. Benbouhenni and N. Bizon, "Enhancing the performance of grid-connected DFIG systems using prescribed convergence law," *Sci Rep,* vol. 15, p. 28550, 5 August 2025.

[23] A. Borni, N. Bessous, L. Zaghba, A. Bouchakour, M. S. Agmas, E. Ali, S. S. M. Ghoneim and A. Hoballah, "Enhancing grid connected wind energy conversion systems through fuzzy logic control optimization with PSO and GA techniques," *Sci Rep,* vol. 15, p. 27678, 29 July 2025.

[24] M. P. O. T. J. Panumpabi, "Large Wind Farm Aggregation and Model Validation.," *IEE,* vol. 1, pp. 12-20, 2011.

[25] H. Chen and L. T. &, "Aggregated Modelling for wind farms for power system transient stability studies," *IEEE,* pp. 5-9, 2015.

[26] T. Ackermann, Ed., *Wind Power in Power Systems*, 2nd ed. Chichester, UK: Wiley, 2012.

[27] M. Ali, J. V. Miranovia, I. Illie and C. &, "Comparison of wind farm aggregate models for transient stability studies," pp. 3-7, 2011.

[28] L. M. Fernandez, C. A. Garcia, J. R. Saenz and F. Jurado, "Reduced Model of DFIGs Wind Farms Using Aggregation of Wind Turbines and Equivalent Wind," in *2006 IEEE Mediterranean Electrotechnical Conference*, Benalmadena, 2006.

[29] L. Zhou, M. Li, X. Shi, M. Zhan, J. Wang, and D. Wu, "Differences in Small-Signal Stability Boundaries Between Aggregated and Granular DFIG Models," arXiv:2604.07777v1, pp.5-9, 2026.

[30] Z. Wang, C. Liu, W. Wang, T. Zhao, Y. Liu, Z. Wang, Y. Sun and X. Wang, "Dynamic aggregation method for wind farms for overvoltage protection and accuracy stability enhancement," *International Journal of Electrical Power & Energy Systems,* vol. 171, p. 111030, October 2025.

[31] S. Zhou, F. Rong and X. Ning, "Optimization Control Strategy for Large Doubly-Fed Induction Generator Wind Farm Based on Grouped Wind Turbine," *Energies,* vol. 14, p. 4848, 9 August 2021.

[32] A. Bayati, F. Mancilla and D. J. Garcia, "Aggregated Models Of Wind Farms:Current Methods and Future Trends," *IEEE,* vol. 2, pp. 3-4, 2016.

[33] L. Shenghu, L. Zhengkai and J. Yudong, "Dynamic aggregation of Double - fed induction generators (DFIG) for stability analysis of wind power system," *IEEE,* vol. 3, pp. 1-6, 2011.

[34] X. Peng, X. Fang, C. Kang, X. T. Ci, W. Feng and J. YuQing, "Equivalent modelling of DFIG-based wind farm using equivalent maximum power curve," *IEEE,* pp. 1-5, 2013.

[35] Z. Meng, "An improved equivalent wind method for the aggregation of DFIG wind turbines," in *Int.conf. on power system, technology, oct 2010*, USA, 2010.

[36] E. Acha, Modeling and Simulation in Power Networks: Advances in Integrated Energy Systems Design, Control, and Optimization, Chichester: Wiley, 2017.

[37] S. Liang and X. Li, "Data-Driven Aggregation Model of Type-III Wind Farms for Power System Transient Characteristic Simulation," *IEEE Access*, vol. 14, pp. 32773–32787, 2026.

[38] C. M. a. D. K. J.K Muriuki, "Suitability of aggregation methods of induction motor models for voltage stability analysis," *IEE,* 2012.

[39] J. Pan and X. J, "Modelling and control of a wind-turbine-drive during grid voltage dips based on DigSILENT/Power factorl," *The 18th International Conference on Electrical Machines and Analysis (ICCEMS),* pp. 8-9, 2015.

[40] J. Conroy and R. Watson, "Aggregate modelling of wind farms containing full-converter wind turbine generators with permanent magnet synchronous

machines: transient stability studies," *IET Renewable Power Generation,* vol. 3, no. 1, pp. 39-52, 2009.

[41] M. Chowdhury, N. Hosseinzadeh, M. Billah and S. Haquet, "Dynamic DFIG wind farm model with an aggregated technique," in *International Conference on Electrical and Computer Engineering*, Bangladesh, 2016.

[42] D. R. Chandaria, F. Grimaccia, M. S. Kumari and M. SYDUL, "Transient Stability Analysis of power system with Grid integration and Wind Generation," *International Review of Electrical Engineering,* vol. 10, pp. 3-8, 2015.

[43] L. J. & Y. M. J.F. Sun, "Research on Multimachine Dynamic Aggregation in wind farm," *Power System Technology,* vol. 1, no. 1, pp. 20-44, 2004.

[44] S. Reddy, "Transient stability analysis of power system with wind generators," *Applied Engineering Research,* vol. 12, no. 19, pp. 1-6, 2017.

[45] J. Quintero, H. Zhang, Y. Chakhchoukh, V. Vittal and G. Heydt, "Next generation Transmission Expansion Planning Framework; Models, Tools, and Educational Opportunities," *Research Gate,* vol. 3, pp. 3-4, 2014.

[46] S. Ncwane and K. A. Folly, "A Review of the Impact of Integrating Wind Power on Transient Stability," *IEEE,* vol. 1, pp. 3-4, 2020.

[47] k. Chen and K. Jucky, "Power and Energy," *IEEE,* pp. 5-7, 2020.

[48] S. Sahoo, "Enhancing pitch angle control in variable speed doubly fed induction generator based wind energy conversion system using advanced adaptive neuro-fuzzy approach with particle swarm optimization," *Wind Engineering,* vol. 49, p. 444–461, April 2025.

[49] N. Khosravi, M. Dowlatabadi, A. Oubelaid and Y. Belkhier, "Optimizing reliability and safety of wind turbine systems through a hybrid control technique for low-voltage ridethrough capability," *Computers and Electrical Engineering,* vol. 123, p. 110205, April 2025.

[50] J. K. & C. Muriithi, "Suitability of aggregation methods of induction motor models for transient stability load modeling of Kenya Power Transmission and distribution system, Nairobi, Kenya, 2016.

[51] J. G. Slootweg and W. L. Kling, "Modeling of large wind farms in power system simulations," in *Proc. IEEE Power Engineering Society Summer Meeting,* pp. 503-508, 2002.

[52] Y. Liu and T. Xu, "Short-Term Active Power Reduction in DFIG-Based Wind Farms for Improving First-Swing Stability in Power Systems," *Energies*, vol. 19, no. 8, p. 1873, 2026.

[53] W. Guo, F. Liu, J. Si, D. He, R. Harley and S. Mei, "Approximate Dynamic Programming Based Supplementary Reactive Power Control for DFIG WindFarm to Enhance Power System Stability,," *ELSEVIER,* pp. 5-10, 2015.

[54] R. V. Riu, A. H. Escribona, J. Fortmann and G. E. Lazaro, "Field Validation of a standard type 3 wind turbine model implemented in DIgSILENT power factory following IEC 61400-27-1 guidelines," *ELSEVIER,* vol. 142, pp. 1-2, 2019.

[55] I. D. Pasiopoulou, E. O. Kontis, T. A. Papadopoulos, and G. K. Papagiannis, "Effect of load modeling on power system stability studies," *Electric Power Systems Research*, vol. 207, p. 107846, 2022.

[56] M. H. Uddin, J. Khalid, M. Smailes, J. L. and S. Wang, "Accurate and computationally efficient aggregated modelling of offshore wind farms for grid compliance," IEEE Transactions on Sustainable Energy, 10.1109/tste. 2026.3666091, 2026.

[57] J. Jiménez-Ruiz, A. Honrubia-Escribano, and E. Gómez-Lázaro, "Machine and Deep Learning Approaches for Wind Turbine Model Parameter Prediction Within the Framework of IEC 61400-27 Standard," *Electronics*, vol. 15, no. 5, p. 1104, 2026.

[58] T. Weckesser, M. Pertl and M. Rezkallah, "Transient stability Improvement," *DTU LIBRARY,* vol. 100(3), pp. 2-6, 2017.

[59] J. M. Marcad-Vargaz, D. Gomez and O. Rabaza, "Aggregated models of permanent magnet synchronous generators wind farms," *Renewable Energy,* vol. 6, no. 1, pp. 5-9, 2015.

[60] X. Wang, X. Chang, M. Yan, Z. Huang, and C. Wu, "Transient Synchronization Stability Analysis of DFIG-Based Wind Turbines with Virtual Resistance Demagnetization Control," *Electronics*, vol. 15, no. 2, p. 467, 2026.

[61] K. Mahmud, A. K. Sahoo, P. Sanjeevikumar and J. B. H. Nielsen, "Computational Tools for Modeling and Analysis of Power Generation and Transmission Systems of the Smart Grid," *IEEE System Control,* vol. 2, pp. 7-9, 2020.

[62] R. Zivanovic and A. Huda, "Large-scale integration of distributed generation into distribution networks:Study objectives, review of models and computational tools," *ELSEVIER,* vol. 69, pp. 3-7, 2017.

[63] Q. Zhou, Y. Wu and X. X. &, "Co-ordinated multiloop switching control of DFIG for resilience enhancement of wind power penetrated power systems," *IEEE Transactions on Sustainable Energy,* pp. 1-11, 2016.

[64] S. Vitanova, V. Stoikov and V. Dimcer, "Comparing DFIG and SCIG for wind generating conditions in Macedonia," *In International Conference on Renewable Energies and Power Quality,* pp. 3-8, 2011.

[65] M. Pöller and S. Achilles, "Aggregated wind park models for analyzing power system dynamics," in *Proc. 4th Int. Workshop on Large-Scale Integration of Wind Power and Transmission Networks for Offshore Wind Farms,* Billund, Denmark, 2003.

[66] R. Baldick, "Integration of Large Scale renewable energy into bulk power systems, 2017.

[67] J. Brochu, C. Larose and R. Gagnon, "Generic Equivalent Collector System Parameters for Large Wind Plant," *IEEE,* vol. 6, pp. 542-549, 2011.

[68] J. Brochu, C. Larose and R. Gagnon, "Validation of single -and multiple-machine equivalence for modelling wind power plants," *IEEE,* vol. 26, no. 2, pp. 532-541, 2011.

[69] C. Guo, H. Tang, B. Niu, and C. Boon Patrick Lee, "A survey of bacterial foraging optimization," *Neurocomputing*, vol. 452, pp. 728–746, Sep. 2021, doi: 10.1016/j.neucom.2020.06.142.

[70] D. Nouti, F. Ponci, and A. Monti, "Heterogeneous Inertia Estimation for Power Systems with High Penetration of Converter-Interfaced Generation," *Energies*, vol. 14, no. 16, p. 5047, Aug. 2021, doi: 10.3390/en14165047.

[71] M. Edrah, K. Lo, A. Elansari, and O. G. Mrehel, "Impact of DFIG based Wind Farms on Transient Stability of Power Systems".

[72] J. Bell, A. Hargrave, G. Smelich, and B. Smyth, "Considerations When Using Charging Current Compensation in Line Current Differential Applications".

[73] R. Anguluri, L. Sankar, and O. Kosut, "Parameter Estimation in Ill-conditioned Low-inertia Power Systems," Aug. 09, 2022, *arXiv*: arXiv:2208.04471. doi: 10.48550/arXiv.2208.04471.

[74] P. Ledesma and J. Usaola, "Doubly Fed Induction Generator Model for Transient Stability Analysis," *IEEE Trans. On Energy Conversion*, vol. 20, no. 2, pp. 388–397, Jun. 2005, doi: 10.1109/TEC.2005.845523.

[75] H. Benbouhenni and N. Bizon, "Advanced Direct Vector Control Method for Optimizing the Operation of a Double-Powered Induction Generator-Based Dual-Rotor Wind Turbine System," *Mathematics*, vol. 9, no. 19, p. 2403, Sep. 2021, doi: 10.3390/math9192403.

[76] P. Sreenivasulu and J. Hussain, "Protection of rotor side converter of doubly fed induction generator based wind energy conversion system under symmetrical grid voltage fluctuations," *Front. Energy Res.*, vol. 12, p. 1465167, Oct. 2024, doi: 10.3389/fenrg. 2024.1465167.

[77] F. Liu, J. Ma, W. Zhang, and M. Wu, "A Comprehensive Survey of Accurate and Efficient Aggregation Modeling for High Penetration of Large-Scale Wind Farms in Smart Grid," *Applied Sciences*, vol. 9, no. 4, p. 769, Feb. 2019, doi: 10.3390/app9040769.

[78] Y. Bekakra and D. B. Attous, "Optimal tuning of PI controller using PSO optimization for indirect power control for DFIG based wind turbine with MPPT," *Int J Syst Assur Eng Manag*, vol. 5, no. 3, pp. 219–229, Sep. 2014, doi: 10.1007/s13198-013-0150-0.

[79] S. Boubzizi, H. Abid, A. El Hajjaji, and M. Chaabane, “Comparative study of three types of controllers for DFIG in wind energy conversion system,” *Prot Control Mod Power Syst*, vol. 3, no. 1, p. 21, Dec. 2018, doi: 10.1186/s41601-018-0096-y.

[80] E. ŞahiN and M. Ş. Ayas, “Parçacik Sürü Optimizasyonu Ayarli Türev Etkisi Filtreli Bir PID Denetleyici için Hata Tabanlı ve Kullanıcı Tanımlı Amaç Fonksiyonlarının Performans Analizi,” *Afyon Kocatepe University Journal of Sciences and Engineering*, vol. 19, no. 3, pp. 682–689, Dec. 2019, doi: 10.35414/akufemubid.520823.

[81] T. M. Shami, A. A. El-Saleh, M. Alswaitti, Q. Al-Tashi, M. A. Summakieh, and S. Mirjalili, “Particle Swarm Optimization: A Comprehensive Survey,” *IEEE Access*, vol. 10, pp. 10031–10061, 2022, doi: 10.1109/ACCESS.2022.3142859.

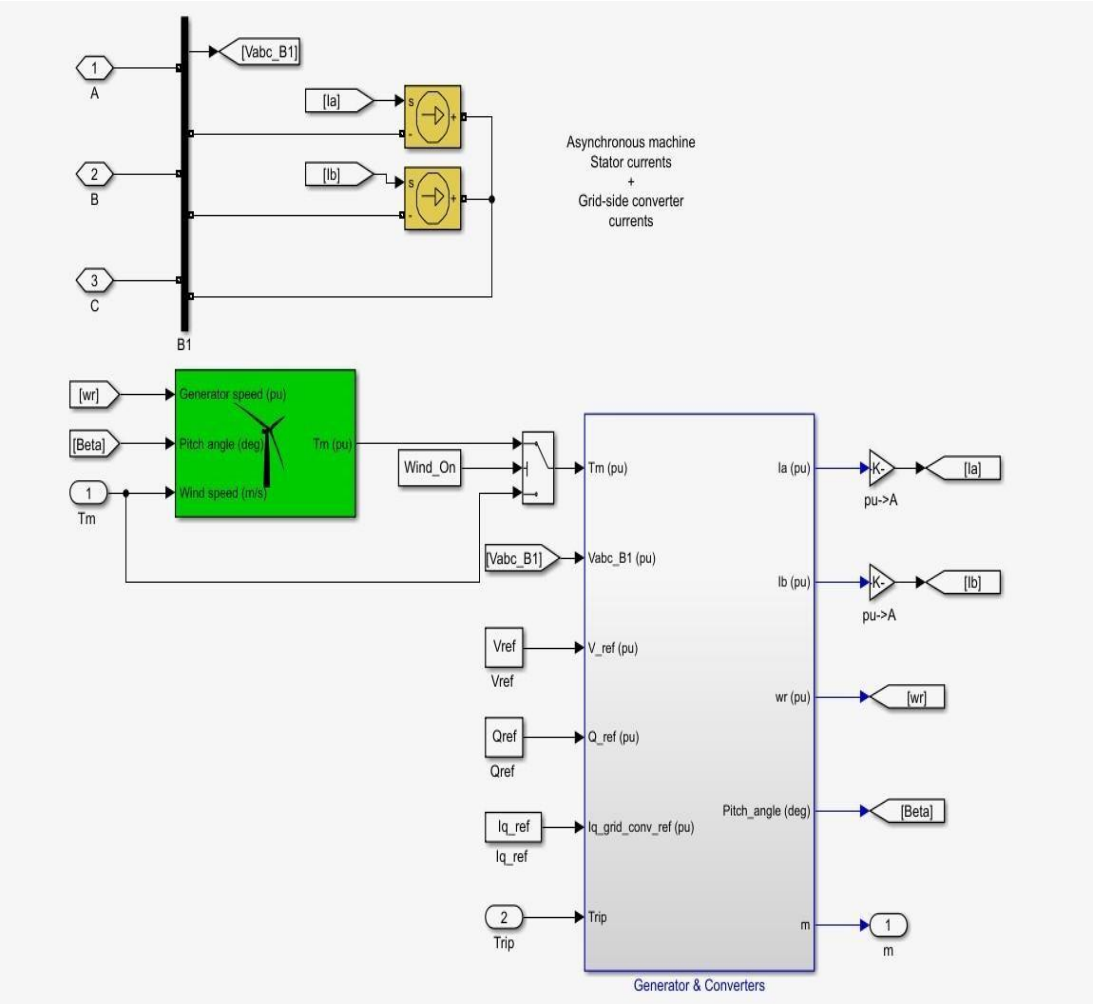
[82] M. S. Amin, M. A. Attia, S. F. Mekhamer, and A. K. Khamees, “Enhancement of PID controller performance for a combined LFC and AVR single- and two-area model using exponential distribution optimization technique,” *Scientific Reports*, vol. 15, art. 44408, Dec. 2025, doi: 10.1038/s41598-025-29137-5.

[83] E. H. Houssein, A. G. Gad, K. Hussain, and P. N. Suganthan, “Major advances in particle swarm optimization: theory, analysis, and application,” *Swarm and Evolutionary Computation*, vol. 63, art. 100868, Jun. 2021, doi: 10.1016/j.swevo.2021.100868.

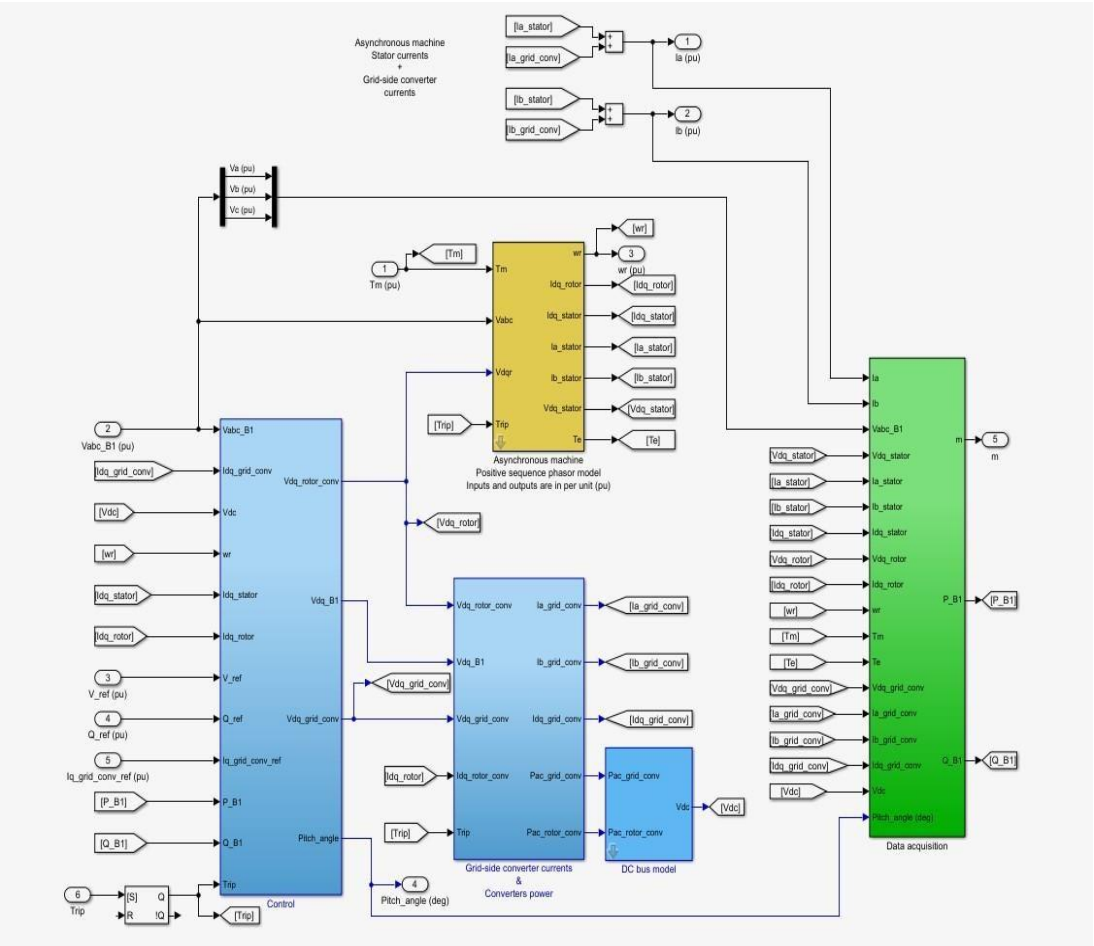
[84] Z. Rafique, H. M. Khalid, S. M. Muyeen, and I. Kamwa, “Bibliographic review on power system oscillations damping: An era of conventional grids and renewable energy integration,” *International Journal of Electrical Power & Energy Systems*, vol. 136, art. 107556, Mar. 2022, doi: 10.1016/j.ijepes.2021.107556.

APPENDICES

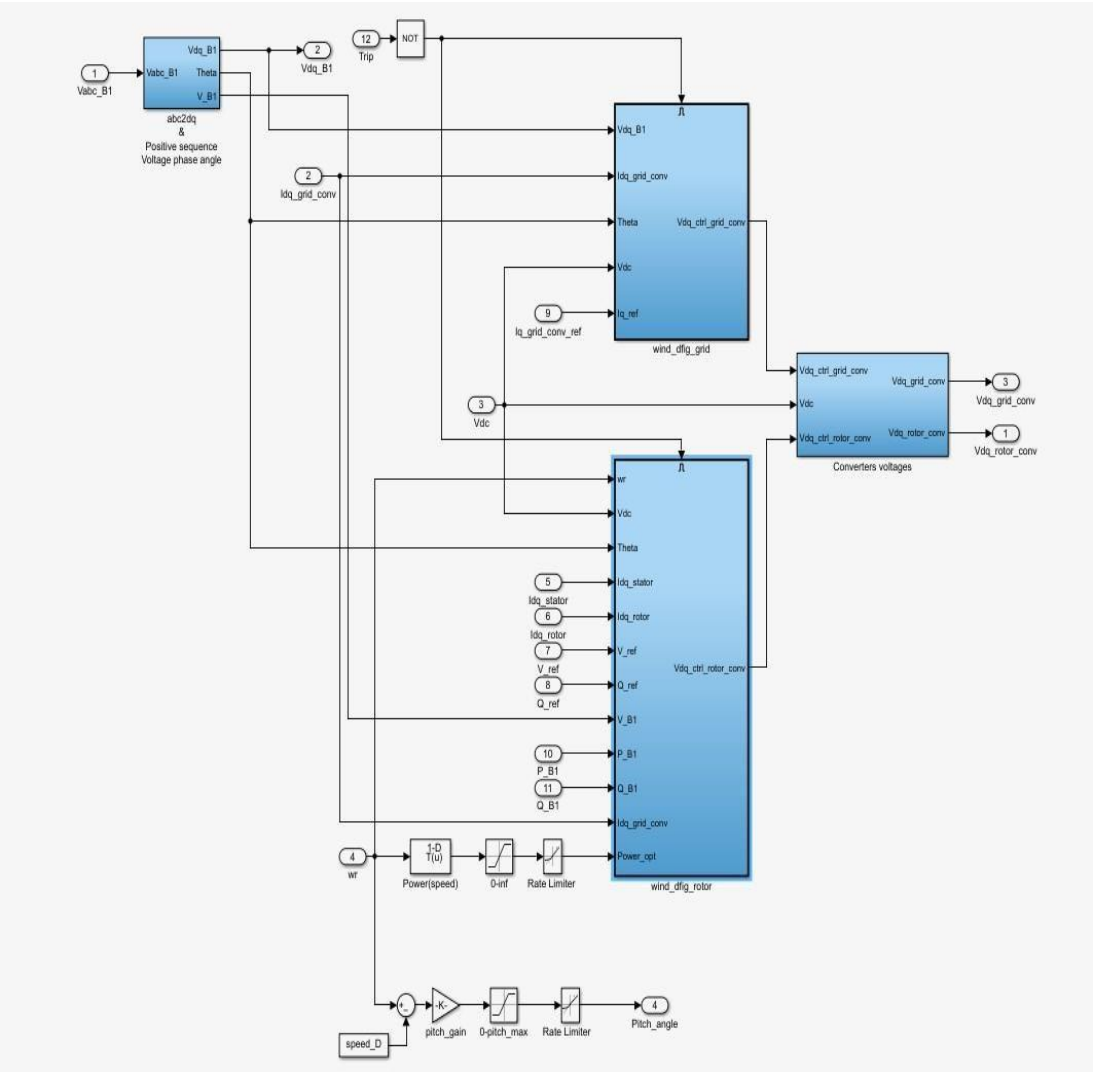
Appendix 1: DFIG Model



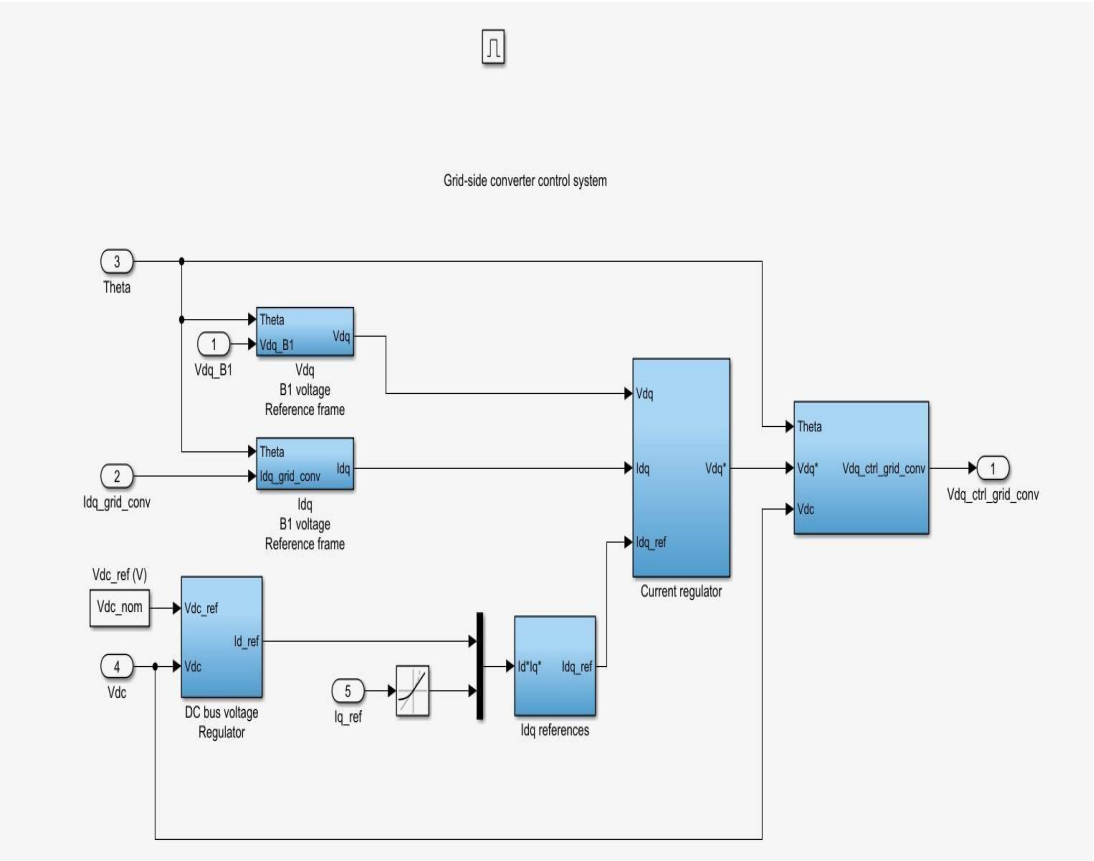
Appendix 2: DFIG Model Generators and Converters



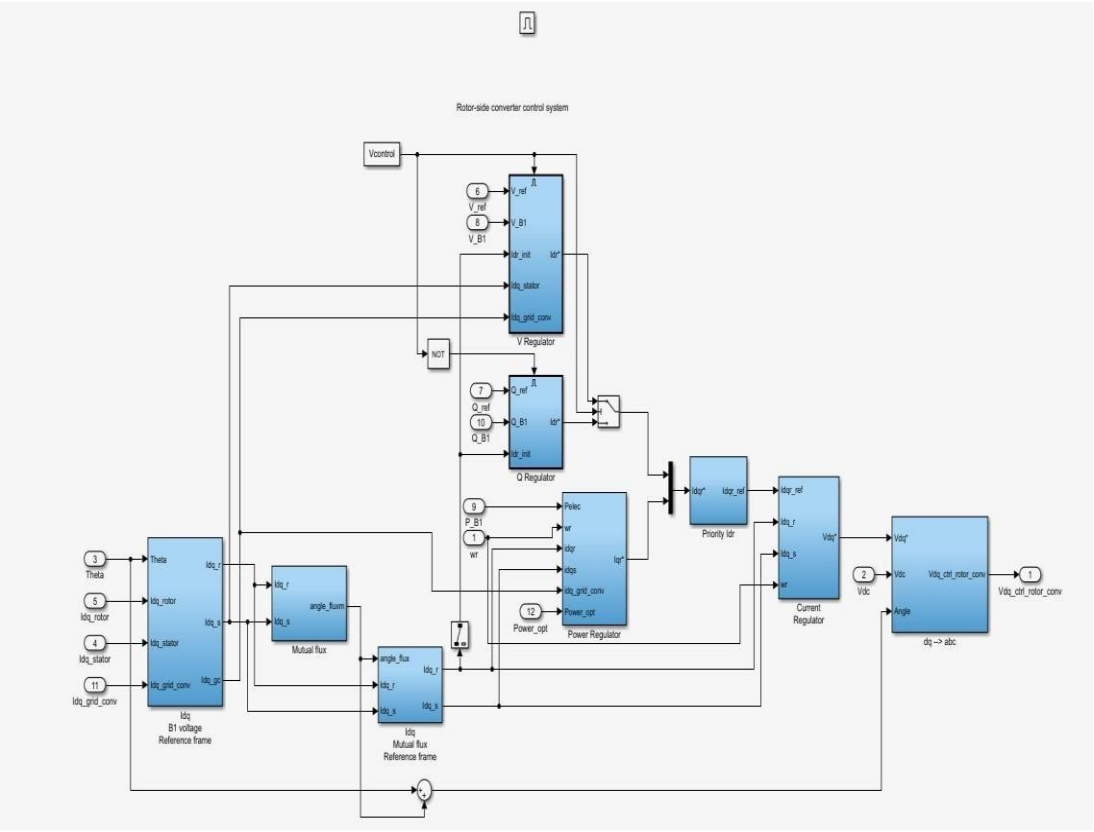
Appendix 3: DFIG Model Control



Appendix 4: DFIG Model Grid Side Controller



Appendix 5: DFIG Model Rotor Side Controller



Appendix 6: MATLAB Script Code

```
% Define the combinations of nV52 and nG52 combinations = [...
   4, 104; ...
   8, 100; ...
   12, 96; ...
   16, 92; ...
   20, 88; ...
   24, 84; ...
   28, 80; ...
   32, 76; ...
   36, 72; ...
   40, 68; ...
   44, 64; ...
   48, 60; ...
   52, 56; ...
   56, 52; ...
   60, 48; ...
   64, 44; ...
   68, 40; ...
   72, 36; ...
   76, 32; ...
   80, 28; ...
   84, 24; ...
   88, 20; ...
   92, 16; ...
   96, 12; ...
   100, 8; ...
   104, 4];

% Check if Parallel Computing Toolbox is available if ~license('test',
'Distrib_Computing_Toolbox')     error('Parallel Computing Toolbox is not
available.'); end

% Set up a parallel pool if one is not already running pool = gcp('nocreate'); % Get
the current parallel pool if isempty(pool)
   pool = parpool; % Create a new pool end
% run the NE39bus_data
NE39bus_data;
% Run simulations in parallel parfor i = 1:size(combinations, 1)

   nV52 = combinations(i, 1);     nG52 = combinations(i, 2);
   [V_data, Q_data, P_data]= runSimulation(nV52, nG52)
   % Call your simulation function
   % Now, proceed with data extraction and appending step response to files
   % Assuming you have the necessary data in V_data, Q_data, and P_data
   % find index where fault is introduced ends     index = find(round(Q_data.Time,4)
== 0.7999, 1);     %% Append step response values to respective files
   appendStepResponseToFile(nV52, nG52, V_data.Time, V_data.Data(:,1),
```

```
'ind_V_stat.txt',index);
   appendStepResponseToFile(nV52, nG52, Q_data.Time, Q_data.Data(:,1),
'ind_Q_stat.txt',index);
   appendStepResponseToFile(nV52, nG52, P_data.Time, P_data.Data(:,1),
'ind_P_stat.txt',index);
   appendStepResponseToFile(nV52, nG52, V_data.Time, V_data.Data(:,2),
'agg_V_stat.txt',index);
   appendStepResponseToFile(nV52, nG52, Q_data.Time, Q_data.Data(:,2),
'agg_Q_stat.txt',index);
   appendStepResponseToFile(nV52, nG52, P_data.Time, P_data.Data(:,2),
'agg_P_stat.txt',index); end
```

Appendix 7: MATLAB User Defined Function Codes

```
function [V_data, Q_data, P_data]= runSimulation(nV52, nG52)
%% Open simulink model warning off

% Create Simulink model model = 'WTDFIG_IEEE_39_Bus'; open_system(model);
% Define DFIG model parameters
%% Independent
Pout = 850e3;  % Nominal output power in Watts
Vstator = 690;  % Stator voltage in Volts
Is = 1760;  % Stator current in Amperes
Ir = 1760;  % Rottor current in Amperes Vrotor = 700;  % Rotor voltage in Volts f =
50;  % Operational frequency in Hz
Torque = 12732;  % Torque in Nm pf = 0.8;  % Power factor eff = 0.95;  %
Efficiency
Poles = 4; % Angular frequency omega = 2 * pi * f;
% Calculate Stator Resistance (Rs) in p.u.
Rs = (Pout / (3 * Is^2)) / ((Vstator^2) / 1e6);
% Calculate Rotor Resistance (Rr) in p.u.
Rr = (Pout / (3 * Ir^2)) / ((Vrotor^2) / 1e6);
% Calculate Leakage Inductance (Lls and Llr) in Henry
Lls = Vstator / (2 * pi * f * Is * pf * eff);
Llr = Vrotor / (2 * pi * f * Ir * pf * eff); sta_ind = sprintf('[%f %f]',Rs,Lls);% stator
inductance rot_ind = sprintf('[%f %f]',Rr,Llr);% roto inductance
% Calculate magnetizing inductance Lm in Henry
Lm = Vstator / (sqrt(3) * Is * omega);
Lm_ind = sprintf('%f',Lm);
% Calculate inertia constant H in seconds
H = 2 * Pout / (Torque * omega); % Calculate friction factor F in p.u.
Damping_factor = 1e-3;
F = Damping_factor / (2 * H);
mec_ind = sprintf('[%f %f %f]',H,F,Poles);
% Converter maximum power (pu)
Converter_max_power = Pout / 1e6;
Pmec_ind = sprintf('%f',Pout);
Pmax_ind = sprintf('%f',Converter_max_power);
% Grid-side coupling inductor [L (pu) R (pu)]
L_grid = Vstator / (sqrt(3) * Is * omega);
R_grid = 0.1 * Rs;
Lchoke_ind = sprintf('[%f %f]',R_grid,L_grid);
% Coupling inductor initial current [IL(pu) ph_IL(deg)]
IL = Is * sqrt(1 - (R_grid / sqrt(R_grid^2 + (omega * L_grid)^2))^2); ph_IL =
atan((omega * L_grid) / R_grid) * 180 / pi; init_inductor_ind = sprintf('[%f
%f]',IL,ph_IL);
% Nominal DC bus voltage (V)
V_DC = Vstator;
Vdc_nom_ind = sprintf('%f',V_DC);
% DC bus capacitor (F)
DeltaV = 0.05 * V_DC;  % Voltage ripple
T_hold = 0.1;  % Hold-up time in seconds
```

```
C_DC = (Pout * T_hold) / (V_DC * DeltaV); capacitor_ind = sprintf('%f',C_DC);
% Control Mode: Var Regulation
% Generated reactive power Qref (pu)
Q_ref = Pout*tan(acos(pf))/1e6;
Qref_ind = sprintf('%f',Q_ref);

%% Aggregate
% Define Independent Parameters for V52 Turbine
Pout_V52 = 850e3;  % Watts
Vstator_V52 = 690;  % Volts
Is_V52 = 1760;  % Amperes
Ir_V52 = 1760;  % Amperes
Vrotor_V52 = 700;  % Volts pf_V52 = 0.8; eff_V52 = 0.95;

% Define Independent Parameters for G52 Turbine
Pout_G52 = 850e3;  % Watts
Vstator_G52 = 690;  % Volts
Is_G52 = 1568;  % Amperes
Ir_G52 = 1568;  % Amperes
Vrotor_G52 = 700;  % Volts pf_G52 = 0.8; eff_G52 = 0.95;

% Operational Frequency (Common) f = 50;  % Hz omega = 2 * pi * f;

% Number of Turbines
%nV52 = 104;
%nG52 = 4;
% power aggreegate
PoutV52_agg = nV52 * Pout_V52;
PoutG52_agg = nG52 * Pout_G52;
% current aggregate
Is_V52agg = nV52 * Is_V52;
Ir_V52agg = nV52 * Ir_V52;
Is_G52agg = nG52 * Is_G52;
Ir_G52agg = nG52 * Ir_G52;
% Calculate Aggregate Parameters for V52
Rs_V52 = (PoutV52_agg / (3 * Is_V52agg^2)) / ((Vstator_V52^2) / 1e6);
Rr_V52 = (PoutV52_agg / (3 * Ir_V52agg^2)) / ((Vrotor_V52^2) / 1e6);
Lls_V52 = Vstator_V52 / (2 * pi * f * Is_V52agg * pf_V52 * eff_V52); Llr_V52 =
Vrotor_V52 / (2 * pi * f * Ir_V52agg * pf_V52 * eff_V52);
% Calculate Aggregate Parameters for G52
Rs_G52 = (PoutG52_agg / (3 * Is_G52agg^2)) / ((Vstator_G52^2) / 1e6);
Rr_G52 = (PoutG52_agg / (3 * Ir_G52agg^2)) / ((Vrotor_G52^2) / 1e6);
Lls_G52 = Vstator_G52 / (2 * pi * f * Is_G52agg * pf_G52 * eff_G52); Llr_G52 =
Vrotor_G52 / (2 * pi * f * Ir_G52agg * pf_G52 * eff_G52);
% Aggregate Parameters for Combined Model
Pout_agg = nV52 * Pout_V52 + nG52 * Pout_G52;
Rs_agg = (Rs_V52 * Rs_G52) / (Rs_V52 + Rs_G52);
Rr_agg = (Rr_V52 * Rr_G52) / (Rr_V52 + Rr_G52);
Lls_agg = (Lls_V52 * Lls_G52) / (Lls_V52 + Lls_G52);
Llr_agg = (Llr_V52 * Llr_G52) / (Llr_V52 + Llr_G52);
```

```
% Converter Maximum Power Calculation
Converter_max_power_V52 = Pout_V52 / 1e6;
Converter_max_power_G52 = Pout_G52 / 1e6;
Converter_max_power_agg = nV52 * Converter_max_power_V52 + nG52 *
Converter_max_power_G52;

% IL Calculation (Initial Current of Coupling Inductor)
IL_V52 = Is_V52 * sqrt(1 - (R_grid / sqrt(R_grid^2 + (omega * L_grid)^2))^2);
IL_G52 = Is_G52 * sqrt(1 - (R_grid / sqrt(R_grid^2 + (omega * L_grid)^2))^2);
IL_agg = nV52 * IL_V52 + nG52 * IL_G52;

% ph_IL Calculation (Phase of Initial Current) ph_IL_V52 = atan((omega * L_grid)
/ R_grid) * 180 / pi; ph_IL_G52 = atan((omega * L_grid) / R_grid) * 180 / pi;
ph_IL_agg = (nV52 * ph_IL_V52 + nG52 * ph_IL_G52) / (nV52 + nG52);

% Vdc_nominal Calculation (Nominal DC Bus Voltage)
Vdc_nominal_V52 = Vrotor_V52;
Vdc_nominal_G52 = Vrotor_G52;
Vdc_nominal_agg = (nV52 * Vdc_nominal_V52 + nG52 * Vdc_nominal_G52) /
(nV52 + nG52);

% Cdc Calculation (DC Bus Capacitor)
DeltaV = 0.05 * Vdc_nominal_agg;  % Voltage ripple
T_hold = 0.1;  % Hold-up time in seconds
Cdc_V52 = (Pout_V52 * T_hold) / (Vdc_nominal_V52 * DeltaV);
Cdc_G52 = (Pout_G52 * T_hold) / (Vdc_nominal_G52 * DeltaV);
Cdc_agg = nV52 * Cdc_V52 + nG52 * Cdc_G52;

% Qref Calculation (Generated Reactive Power)
Qref_V52 = Pout_V52 * tan(acos(pf_V52)) / 1e6;
Qref_G52 = Pout_G52 * tan(acos(pf_G52)) / 1e6;
Qref_agg = nV52 * Qref_V52 + nG52 * Qref_G52;
% Calculate magnetizing inductance Lm in Henry for V52 and G52
Lm_V52 = Vstator_V52 / (sqrt(3) * Is_V52 * omega);
Lm_G52 = Vstator_G52 / (sqrt(3) * Is_G52 * omega);
% Calculate aggregate magnetizing inductance Lm_aggr
Lm_aggr = (nV52 * Lm_V52 + nG52 * Lm_G52) / (nV52 + nG52);
% Resistance of the coupling inductor for V52 and G52 (assuming R_grid is
common)
R_grid_V52 = 0.1 * Rs_V52;
R_grid_G52 = 0.1 * Rs_G52;

% Calculate aggregate resistance R_agg
R_agg = (nV52 * R_grid_V52 + nG52 * R_grid_G52) / (nV52 + nG52);
% Grid-side coupling inductor L (in per unit) for V52 and G52
L_grid_V52 = Vstator_V52 / (sqrt(3) * Is_V52 * omega);
L_grid_G52 = Vstator_G52 / (sqrt(3) * Is_G52 * omega);

% Calculate aggregate inductance L_agg
```

```
L_agg = (nV52 * L_grid_V52 + nG52 * L_grid_G52) / (nV52 + nG52);

% Update Parameters
nom = sprintf('[%f %f %f]',Pout_agg,Vdc_nominal_agg,f); sta_agg = sprintf('[%f
%f]',Rs_agg,Lls_agg); rot_agg = sprintf('[%f %f]',Rr_agg,Llr_agg); Lm_agg =
sprintf('%f',Lm_aggr);
mec_agg = sprintf('[%f %f %f]',H,F,Poles);
Pmec_agg = sprintf('%f',Pout_agg);
Pmax_agg = sprintf('%f',Converter_max_power_agg); Lchoke_agg = sprintf('[%f
%f]',R_agg,L_agg);
init_inductor_agg = sprintf('[%f %f]',IL_agg,ph_IL_agg);
Vdc_nom_agg = sprintf('%f',Vdc_nominal_agg); capacitor_agg =
sprintf('%f',Cdc_agg);
Qref_agg = sprintf('%f',Qref_agg);

%% Update simulink Model
set_param([model '/DFIG_ind'],'sta',sta_ind); set_param([model
'/DFIG_ind'],'rot',rot_ind); set_param([model '/DFIG_ind'],'Lm',Lm_ind);
set_param([model '/DFIG_ind'],'mec',mec_ind); set_param([model
'/DFIG_ind'],'Pmax',Pmax_ind); set_param([model '/DFIG_ind'],'Pmec',Pmec_ind);
set_param([model '/DFIG_ind'],'Lchoke',Lchoke_ind); set_param([model
'/DFIG_ind'],'init_inductor',init_inductor_ind); set_param([model
'/DFIG_ind'],'Vdc_nom',Vdc_nom_ind); set_param([model
'/DFIG_ind'],'capacitor',capacitor_ind); set_param([model
'/DFIG_ind'],'Qref',Qref_ind);
  set_param([model '/DFIG_aggregate'],'sta',sta_agg); set_param([model
'/DFIG_aggregate'],'rot',rot_agg); set_param([model
'/DFIG_aggregate'],'Lm',Lm_agg); set_param([model
'/DFIG_aggregate'],'mec',mec_agg); set_param([model
'/DFIG_aggregate'],'Pmax',Pmax_agg); set_param([model
'/DFIG_aggregate'],'Pmec',Pmec_agg); set_param([model
'/DFIG_aggregate'],'Lchoke',Lchoke_agg); set_param([model
'/DFIG_aggregate'],'init_inductor',init_inductor_agg); set_param([model
'/DFIG_aggregate'],'Vdc_nom',Vdc_nom_agg); set_param([model
'/DFIG_aggregate'],'capacitor',capacitor_agg); set_param([model
'/DFIG_aggregate'],'Qref',Qref_agg); set_param([model
'/DFIG_aggregate'],'nom',nom);

%% Tunning the control params
%Tune grid-side converter controller using PI tuning % Create a transfer function
model for GSC current control tau_GSC = Lls / Rs;% time constant
Km_GSC = 1 / Rs;% DC gain
% Define pidtune options with desired phase margin
opts = pidtuneOptions('PhaseMargin', 60);  % 60-degree phase margin
% Create the transfer function for GSC current control sys_GSC = tf(Km_GSC,
[tau_GSC, 1]);
% Use pidtune to get the PI controller parameters for GSC
%controller_GSC = pidtune(sys_GSC, 'PI',opts);
% Extract Kp and Ki for GSC current control
%Kp_GSC_tuned = controller_GSC.Kp;
```

```
%Ki_GSC_tuned = controller_GSC.Ki;
[controller_GSC, bestScore]= PSO_optimize(sys_GSC,[0 0],[1 100]);
% Extract Kp and Ki for GSC current control
Kp_GSC_tuned = controller_GSC(1);
Ki_GSC_tuned = controller_GSC(2);

% Create a transfer function model for reactive power control % Time constant and
gain for the reactive power loop tau_q = (Lls + Llr) / (Rs + Rr);
K_q = (Lls * Llr) / (Lls + Llr) * 1 / (Rs + Rr);  % Create the transfer function for
reactive power control sys_reactive_power = tf(K_q, [tau_q, 1]);
% Use pidtune to get the PI controller parameters
%controller_reactive_power = pidtune(sys_reactive_power, 'PI',opts);
% Extract Kp and Ki for reactive power control
%Kp_reactive_power = controller_reactive_power.Kp;
%Ki_reactive_power = controller_reactive_power.Ki;
% Using PSO
[controller_reactive_power, bestScore_rpc]=
PSO_optimize(sys_reactive_power,[0 0],[1e3 1e3]); % Extract Kp and Ki for
reactive power control
Kp_reactive_power = controller_reactive_power(1);
Ki_reactive_power = controller_reactive_power(2);
%Tune rotor-side converter controller using PI tuning %Create a transfer function
model for RSC current control tau_RSC = Llr / Rr;
Km_RSC = 1 / Rr;
% Create the transfer function for RSC current control sys_RSC = tf(Km_RSC,
[tau_RSC, 1]);
% Use pidtune to get the PI controller parameters for RSC %opts =
pidtuneOptions('PhaseMargin',45,'DesignFocus','disturbancerejection');
%controller_RSC = pidtune(sys_RSC, 'PI',opts);
% Extract Kp and Ki for RSC current control
%Kp_RSC_tuned = controller_RSC.Kp;
%Ki_RSC_tuned = controller_RSC.Ki;
% Using PSO
[controller_RSC, bestScore_Power]= PSO_optimize(sys_RSC,[0 0],[1 100]);
% Extract Kp and Ki for RSC current control
Kp_RSC_tuned = controller_RSC(1);
Ki_RSC_tuned = controller_RSC(2);

% Create a transfer function model for Power control
tau_Power = (Lls + Llr) / (Rs + Rr);
Km_Power = 1 / (Rs + Rr);
% Create the transfer function for Power control sys_Power = tf(Km_Power,
[tau_Power, 1]);
% Use pidtune to get the PI controller parameters for Power control
%controller_Power = pidtune(sys_Power, 'PI',opts);
% Extract Kp and Ki for Power control
%Kp_Power = controller_Power.Kp;
%Ki_Power = controller_Power.Ki;
% Using PSO
```

```
[controller_Power, bestScore_rsc]= PSO_optimize(sys_Power,[0 0],[1 200]); %
Extract Kp and Ki for Power control
Kp_Power = controller_Power(1);
Ki_Power = controller_Power(2);

%Tune DC bus voltage regulator gains
%Create a transfer function model for DC voltage control tau_DC = R_grid *
C_DC;
Km_DC = 1 / R_grid;
% Create the transfer function for DC voltage control sys_DC = tf(Km_DC,
[tau_DC, 1]);
% Use pidtune to get the PI controller parameters for DC voltage control
%controller_DC = pidtune(sys_DC, 'PI',opts);
% Extract Kp and Ki for DC voltage control
%Kp_DC = controller_DC.Kp;
%Ki_DC = controller_DC.Ki;
% Using PSO
[controller_DC, bestScore_DC]= PSO_optimize(sys_DC,[0 0],[1 1]);
% Extract Kp and Ki for DC voltage control
Kp_DC = controller_DC(1);
Ki_DC = controller_DC(2);

%aggregate model

%Tune grid-side converter controller using PI tuning % Create a transfer function
model for GSC current control
tau_GSC_agg = Lls_agg / Rs_agg;
Km_GSC_agg = 1 / Rs_agg;
% Define pidtune options with desired phase margin
opts = pidtuneOptions('PhaseMargin', 60);  % 60-degree phase margin
% Create the transfer function for GSC current control sys_GSC_agg =
tf(Km_GSC_agg, [tau_GSC_agg, 1]);
% Use pidtune to get the PI controller parameters for GSC
%controller_GSC_agg = pidtune(sys_GSC_agg, 'PI',opts);
% Extract Kp and Ki for GSC current control
%Kp_GSC_tuned_agg = controller_GSC_agg.Kp;
%Ki_GSC_tuned_agg = controller_GSC_agg.Ki;
[controller_GSC_agg, bestScore_agg]= PSO_optimize(sys_GSC_agg,[0 0],[1 100]);
% Extract Kp and Ki for GSC current control
Kp_GSC_tuned_agg = controller_GSC_agg(1);
Ki_GSC_tuned_agg = controller_GSC_agg(2);

% Create a transfer function model for reactive power control % Time constant and
gain for the reactive power loop tau_q_agg = (Lls_agg + Llr_agg) / (Rs_agg +
Rr_agg);
K_q_agg = (Lls_agg * Llr_agg) / (Lls_agg + Llr_agg) * 1 / (Rs_agg + Rr_agg);
% Create the transfer function for reactive power control sys_reactive_power_agg =
tf(K_q_agg, [tau_q_agg, 1]);
% Use pidtune to get the PI controller parameters
%controller_reactive_power_agg = pidtune(sys_reactive_power_agg, 'PI',opts);
```

```
% Extract Kp and Ki for reactive power control
%Kp_reactive_power_agg = controller_reactive_power_agg.Kp;
%Ki_reactive_power_agg = controller_reactive_power_agg.Ki; % Using PSO
[controller_reactive_power_agg, bestScore_rpc_agg]=
PSO_optimize(sys_reactive_power_agg,[0 0],[1e3 1e3]);
% Extract Kp and Ki for reactive power control
Kp_reactive_power_agg = controller_reactive_power_agg(1);
Ki_reactive_power_agg = controller_reactive_power_agg(1);

%Tune rotor-side converter controller using PI tuning %Create a transfer function
model for RSC current control
tau_RSC_agg = Llr_agg / Rr_agg;
Km_RSC_agg = 1 / Rr_agg;
% Create the transfer function for RSC current control sys_RSC_agg =
tf(Km_RSC_agg, [tau_RSC_agg, 1]);
% Use pidtune to get the PI controller parameters for RSC %opts =
pidtuneOptions('PhaseMargin',45,'DesignFocus','disturbancerejection');
%controller_RSC_agg = pidtune(sys_RSC_agg, 'PI',opts);
% Extract Kp and Ki for RSC current control
%Kp_RSC_tuned_agg = controller_RSC_agg.Kp;
%Ki_RSC_tuned_agg = controller_RSC_agg.Ki;
% Using PSO
[controller_RSC_agg, bestScore_Power_agg]= PSO_optimize(sys_RSC_agg,[0 0],[1
100]);
% Extract Kp and Ki for RSC current control
Kp_RSC_tuned_agg = controller_RSC_agg(1);
Ki_RSC_tuned_agg = controller_RSC_agg(2);

% Create a transfer function model for Power control tau_Power_agg = (Lls_agg +
Llr_agg) / (Rs_agg + Rr_agg);
Km_Power_agg = 1 / (Rs_agg + Rr_agg);
% Create the transfer function for Power control sys_Power_agg =
tf(Km_Power_agg, [tau_Power_agg, 1]);
% Use pidtune to get the PI controller parameters for Power control
%controller_Power_agg = pidtune(sys_Power_agg, 'PI',opts);
% Extract Kp and Ki for Power control
%Kp_Power_agg = controller_Power_agg.Kp;
%Ki_Power_agg = controller_Power_agg.Ki;
% Using PSO
[controller_Power_agg, bestScore_rsc_agg]= PSO_optimize(sys_Power_agg,[0
0],[1 200]);
% Extract Kp and Ki for Power control
Kp_Power_agg = controller_Power_agg(1);
Ki_Power_agg = controller_Power_agg(2);

%Tune DC bus voltage regulator gains
%Create a transfer function model for DC voltage control tau_DC_agg = R_agg *
C_DC;
Km_DC_agg = 1 / R_agg;
```

```
% Create the transfer function for DC voltage control sys_DC_agg =
tf(Km_DC_agg, [tau_DC_agg, 1]);
% Use pidtune to get the PI controller parameters for DC voltage control
%controller_DC_agg = pidtune(sys_DC_agg, 'PI',opts);
% Extract Kp and Ki for DC voltage control
%Kp_DC_agg = controller_DC_agg.Kp;
%Ki_DC_agg = controller_DC_agg.Ki;
% Using PSO
[controller_DC_agg, bestScore_DC_agg]= PSO_optimize(sys_DC_agg,[0 0],[1 1]);
% Extract Kp and Ki for DC voltage control
Kp_DC_agg = controller_DC_agg(1);
Ki_DC_agg = controller_DC_agg(2);

%% Update the control system param
%Tuned Grid-side converter current regulator gains: [Kp Ki]
Kpi_rotor_side_cur_reg = sprintf('[%f %f]',Kp_GSC_tuned,Ki_GSC_tuned);
Kpi_rotor_side_cur_reg_agg = sprintf('[%f
%f]',Kp_GSC_tuned_agg,Ki_GSC_tuned_agg);
%Set rotor-side controller parameters set_param([model
'/DFIG_ind'],'Kpi_rotor_side_cur_reg',Kpi_rotor_side_cur_reg); set_param([model
'/DFIG_aggregate'],'Kpi_rotor_side_cur_reg',Kpi_rotor_side_cur_reg_agg);
%Tuned Rotor-side converter current regulator gains: [Kp Ki]
Kpi_grid_side_cur_reg = sprintf('[%f %f]',Kp_RSC_tuned,Ki_RSC_tuned);
Kpi_grid_side_cur_reg_agg = sprintf('[%f
%f]',Kp_RSC_tuned_agg,Ki_RSC_tuned_agg);
%Set grid-side controller parameters
set_param([model '/DFIG_ind'],'Kpi_grid_side_cur_reg',Kpi_grid_side_cur_reg);
set_param([model
'/DFIG_aggregate'],'Kpi_grid_side_cur_reg',Kpi_grid_side_cur_reg_agg);

%Tuned Reactive power regulator gains: [Kp Ki]
Kpi_Q = sprintf('[%f %f]', Kp_reactive_power, Ki_reactive_power);
Kpi_Q_agg = sprintf('[%f %f]', Kp_reactive_power_agg, Ki_reactive_power_agg);
set_param([model '/DFIG_ind'], 'Kpi_Q', Kpi_Q); set_param([model
'/DFIG_aggregate'], 'Kpi_Q', Kpi_Q_agg);

% Tuned Power regulator gains: [Kp Ki]
Kpi_power_reg = sprintf('[%f %f]', Kp_Power, Ki_Power);
Kpi_power_reg_agg = sprintf('[%f %f]', Kp_Power_agg, Ki_Power_agg);
set_param([model '/DFIG_ind'], 'Kpi_power_reg', Kpi_power_reg);
set_param([model '/DFIG_aggregate'], 'Kpi_power_reg', Kpi_power_reg_agg);
% Tuned DC bus voltage regulator gains: [Kp Ki]
Kpi_dc_reg = sprintf('[%f %f]', Kp_DC, Ki_DC);
Kpi_dc_reg_agg = sprintf('[%f %f]', Kp_DC_agg, Ki_DC_agg); set_param([model
'/DFIG_ind'], 'Kpi_dc_reg', Kpi_dc_reg); set_param([model '/DFIG_aggregate'],
'Kpi_dc_reg', Kpi_dc_reg_agg);
%% Run Tuned simulation
% Configure simulation settings
% Set the simulation stop time set_param(model, 'StopTime', '20');
```

```
% Set the solver type if not already set (optional) set_param(model, 'Solver',
'ode15s');

% Increase the Max step size set_param(model, 'MaxStep', '1'); %

% Adjust these tolerances to balance between speed and accuracy set_param(model,
'RelTol', '1e-3'); set_param(model, 'AbsTol', '1e-3');

% Start the simulation
set_param(model, 'SimulationCommand', 'start');

% Wait for the simulation to complete using a while loop while true
   % Check the simulation status
   status = get_param(model, 'SimulationStatus');     if strcmp(status, 'stopped')
      break; % Exit the loop if the simulation has stopped     end
   pause(1); % Wait for a short time before checking again end

% Simulation has finished disp('Simulation completed.');

% retrive data from work space
V_data = evalin('base', 'V_data'); % Retrieve V_data from the base workspace
Q_data = evalin('base', 'Q_data'); % Retrieve Q_data
P_data = evalin('base', 'P_data'); % Retrieve P_data

% Plot the scope data figure; subplot(3,1,1)
plot(P_data.Time, P_data.Data(:,1),'r'); hold on
plot(P_data.Time, P_data.Data(:,2),'b'); ylim([-0.001 0.7]); xlabel('Time(s)');
ylabel('Active Power(p.u.)'); title('Active Power Step Response');
legend('Indpendent', 'Aggregate')
  subplot(3,1,2)
plot(V_data.Time, V_data.Data(:,1),'r'); hold on
plot(V_data.Time, V_data.Data(:,2),'b'); ylim([-0.01 2]); xlabel('Time (s)');
ylabel('Voltage (p.u.)'); title('Voltage Step Response'); legend('Independent',
'Aggregate')
  subplot(3,1,3)
plot(Q_data.Time, Q_data.Data(:,1),'r'); hold on
plot(Q_data.Time, Q_data.Data(:,2),'b'); ylim([-0.01 0.5]); xlabel('Time(s)');
ylabel('Reactive Power(p.u.)'); title('Reactive Power Step Response');
legend('Indpendent', 'Aggregate')

% Construct the filename
filename = sprintf('nV52_%d_nG52_%d.png', nV52, nG52);
% Save the figure as an image
saveas(gcf, filename);
  end

function [bestParams, bestScore]= PSO_optimize(sys_GSC,lb,ub)
% Define the objective function handle
objectiveFunction = @(params) piObjective(params, sys_GSC);
```

```
% Use particleswarm to optimize the PI parameters
  options = optimoptions('particleswarm', ...
    'SwarmSize', 30, ...
    'MaxIterations', 200, ... % Increase max iterations
    'MaxStallIterations', 50, ... % Increase stall iterations
    'FunctionTolerance', 1e-3, ... % Adjust function tolerance
    'Display', 'iter'); % Display iteration info
[bestParams, bestScore] = particleswarm(objectiveFunction, 2, lb, ub, options); end
function J = piObjective(params, sys)
    Kp = params(1);
    Ki = params(2);

    % Define the PI controller     piController = pid(Kp, Ki);

    % Closed-loop system
    closedLoopSystem = feedback(piController * sys, 1);

    % Step response
    [y, t] = step(closedLoopSystem);

    % Calculate the performance index (for example, ISE)     error = 1 - y;
    J = sum(t .* (error .^ 2)); end

% Plot the scope data figure;
plot(P_data_allPhase_grnd.Time, P_data_allPhase_grnd.Data(:,1),'r'); hold on
plot(P_data_allPhase_grnd.Time, P_data_allPhase_grnd.Data(:,2),'b');
plot(P_data_2Phase_grnd.Time, P_data_2Phase_grnd.Data(:,1),'m');
plot(P_data_2Phase_grnd.Time, P_data_2Phase_grnd.Data(:,2),'k');
plot(P_data_1Phase_grnd.Time, P_data_1Phase_grnd.Data(:,1),'g');
plot(P_data_1Phase_grnd.Time, P_data_1Phase_grnd.Data(:,2),'c'); ylim([-0.001
0.3]); xlabel('Time(s)'); ylabel('Active Power(p.u.)'); title('Active Power Step
Response'); legend('Independent 3-phase grounded', 'Aggregate 3-phase grounded',...
'Independent 2-phase grounded', 'Aggregate 2-phase grounded',... 'Independent 1-
phase grounded', 'Aggregate 1-phase grounded')
  figure;
plot(V_data_allPhase_grnd.Time, V_data_allPhase_grnd.Data(:,1),'r'); hold on
plot(V_data_allPhase_grnd.Time, V_data_allPhase_grnd.Data(:,2),'b');
plot(V_data_2Phase_grnd.Time, V_data_2Phase_grnd.Data(:,1),'m');
plot(V_data_2Phase_grnd.Time, V_data_2Phase_grnd.Data(:,2),'k');
plot(V_data_1Phase_grnd.Time, V_data_1Phase_grnd.Data(:,1),'g');
plot(V_data_1Phase_grnd.Time, V_data_1Phase_grnd.Data(:,2),'c');
plot(V_data_.Time, V_data_.Data(:,1),'Color',"#A2142F"); plot(V_data_.Time,
V_data_.Data(:,2),'Color',"#4DBEEE"); ylim([-0.01 2.5]); xlabel('Time (s)');
ylabel('Voltage (p.u.)'); title('Voltage Step Response'); legend('Independent 3-phase
grounded', 'Aggregate 3-phase grounded',...
'Independent 2-phase grounded', 'Aggregate 2-phase grounded',... 'Independent 1-
phase grounded', 'Aggregate 1-phase grounded')
  figure;
plot(Q_data_allPhase_grnd.Time, Q_data_allPhase_grnd.Data(:,1),'r'); hold on
```

```
plot(Q_data_allPhase_grnd.Time, Q_data_allPhase_grnd.Data(:,2),'b');
plot(Q_data_2Phase_grnd.Time, Q_data_2Phase_grnd.Data(:,1),'m');
plot(Q_data_2Phase_grnd.Time, Q_data_2Phase_grnd.Data(:,2),'k');
plot(Q_data_1Phase_grnd.Time, Q_data_1Phase_grnd.Data(:,1),'g');
plot(Q_data_1Phase_grnd.Time, Q_data_1Phase_grnd.Data(:,2),'c'); ylim([-0.01
0.2]); xlabel('Time(s)'); ylabel('Reactive Power(p.u.)'); title('Reactive Power Step
Response'); legend('Independent 3-phase grounded', 'Aggregate 3-phase grounded',...
'Independent 2-phase grounded', 'Aggregate 2-phase grounded',... 'Independent 1-
phase grounded', 'Aggregate 1-phase grounded')

% Plot the scope data figure;
plot(P_data_allPhase_grnd.Time, P_data_allPhase_grnd.Data(:,1),'r'); hold on
plot(P_data_allPhase_grnd.Time, P_data_allPhase_grnd.Data(:,2),'b');
plot(P_data_.Time, P_data_.Data(:,1),'Color',"#A2142F"); plot(P_data_.Time,
P_data_.Data(:,2),'Color',"#4DBEEE"); ylim([-0.001 0.3]); xlabel('Time(s)');
ylabel('Active Power(p.u.)'); title('Active Power Step Response');
legend('Independent 3-phase grounded', 'Aggregate 3-phase grounded',...
'Independent 3-phase ungrounded', 'Aggregate 3-phase ungrounded')
  figure;
plot(V_data_allPhase_grnd.Time, V_data_allPhase_grnd.Data(:,1),'r'); hold on
plot(V_data_allPhase_grnd.Time, V_data_allPhase_grnd.Data(:,2),'b');
plot(V_data_.Time, V_data_.Data(:,1),'Color',"#A2142F"); plot(V_data_.Time,
V_data_.Data(:,2),'Color',"#4DBEEE");
ylim([-0.01 2]); xlabel('Time (s)'); ylabel('Voltage (p.u.)'); title('Voltage Step
Response'); legend('Independent 3-phase grounded', 'Aggregate 3-phase grounded',...
'Independent 3-phase ungrounded', 'Aggregate 3-phase ungrounded')
   figure;
plot(Q_data_allPhase_grnd.Time, Q_data_allPhase_grnd.Data(:,1),'r'); hold on
plot(Q_data_allPhase_grnd.Time, Q_data_allPhase_grnd.Data(:,2),'b');
plot(Q_data_.Time, Q_data_.Data(:,1),'Color',"#A2142F"); plot(Q_data_.Time,
Q_data_.Data(:,2),'Color',"#4DBEEE"); ylim([-0.01 0.2]); xlabel('Time(s)');
ylabel('Reactive Power(p.u.)'); title('Reactive Power Step Response');
legend('Independent 3-phase grounded', 'Aggregate 3-phase grounded',...
'Independent 3-phase ungrounded', 'Aggregate 3-phase ungrounded')

% Define file names and sanitize for struct field names
fileNames = {'ind_P_stat.txt', 'agg_P_stat.txt', 'ind_Q_stat.txt',
'agg_Q_stat.txt', 'ind_V_stat.txt', 'agg_V_stat.txt'}; sanitizedFieldNames =
strrep(fileNames, '.', '_');

% Initialize data storage dataStruct = struct();
for i = 1:length(sanitizedFieldNames)     dataStruct.(sanitizedFieldNames{i}) = [];
end

% Read and store data for i = 1:length(fileNames)     currentFile = fileNames{i};
   currentFieldName = sanitizedFieldNames{i};     if isfile(currentFile)
      fileData = readmatrix(currentFile, 'Delimiter', ',');
dataStruct.(currentFieldName) = fileData;     else
      warning('File %s does not exist.', currentFile);     end end
```

```
% Initialize cell arrays for box plot data settlingTimeBoxData = {};
steadyStateBoxData = {}; % Add labels for the plots  labels =
{'Ind_ActivePower','Agg_ActivePower','Ind_ReactivePower','Agg_ReactivePower',
...
    'Ind_Voltage','Agg_Voltage'};

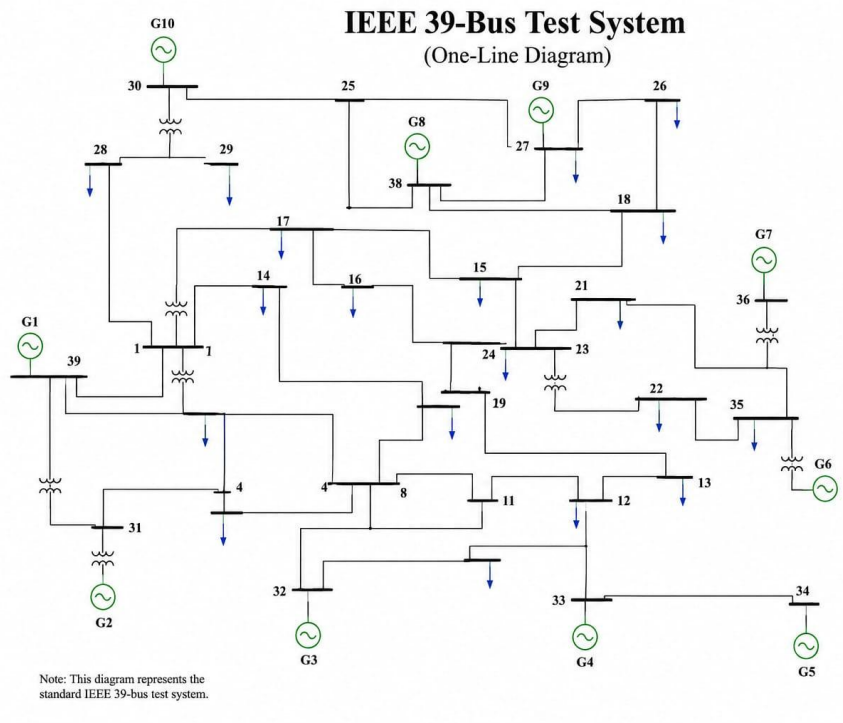
% Extract settling time and steady state values for box plots for i =
1:length(sanitizedFieldNames)     currentFieldName = sanitizedFieldNames{i};
   if ~isempty(dataStruct.(currentFieldName))
      % Extract data
      settlingTime = dataStruct.(currentFieldName)(1:27, 4); % Fourth column is
settling time
      steadyStateValue = dataStruct.(currentFieldName)(1:27, 6); % Sixth column is
steady state value

      % Add to cell arrays for box plot        settlingTimeBoxData{end+1} =
settlingTime;        steadyStateBoxData{end+1} = steadyStateValue;
            end end

% Box plot for Settling Time figure;
boxplot(cell2mat(settlingTimeBoxData), 'Labels', labels); title('Box Plot of Settling
Times'); ylabel('Settling Time'); xlabel('File Names');

% Box plot for Steady State Value figure;
boxplot(cell2mat(steadyStateBoxData), 'Labels', labels); title('Box Plot of Steady
State Values'); ylabel('Steady State Value');
xlabel ('File Names');
```

Appendix 8: IEEE 39-Bus Test System



Legend

- Generator
- Bus
- Transmission Line
- Transformer
- Load

Generators

ID	Bus	P_G (MW)	Q_G (MVAr)
G1	39	616.0	62.4
G2	31	650.0	65.0
G3	32	540.0	48.6
G4	33	632.0	43.0
G5	34	508.0	0.0
G6	35	650.0	0.0
G7	36	560.0	0.0
G8	37	540.0	0.0
G9	38	830.0	0.0
G10	30	100.0	0.0

System Summary

Number of Buses	39
Number of Generators	10
Number of Loads	29
Number of Lines	46
Number of Transformers	12

Appendix9: Load flow Analysis

Block name	Block type	Bus type	Vbase (kV)	Vref (pu)	Vangle (deg)	P (MW)	Q (Mvar)
IEEE 39 Bus/G10/G10	SM	PV	22.0	1.048	0.0	250.0	0.0
IEEE39 Bus/load39	RLC load	PQ	345.0	1.030	0.0	1104.0	250.0
IEEE39 Bus/G2/G2	SM	swing	22.0	0.982	0.0	0.0	0.0
IEEE39 Bus/load31	RLC load	PQ	22.0	0.982	0.0	9.2	4.6
IEEE39 Bus/G3/G3	SM	PV	22.0	0.983	0.0	650.0	0.0
IEEE39 Bus/G4/G4	SM	PV	22.0	0.997	0.0	632.0	0.0
IEEE39 Bus/G5/G5	SM	PV	22.0	1.012	0.0	508.0	0.0
IEEE39 Bus/G6/G6	SM	PV	22.0	1.049	0.0	650.0	0.0
IEEE39 Bus/G7/G7	SM	PV	22.0	1.064	0.0	560.0	0.0
IEEE39 Bus/G8/G8	SM	PV	22.0	1.028	0.0	540.0	0.0
IEEE39 Bus/G9/G9	SM	PV	22.0	1.027	0.0	830.0	0.0
IEEE39 Bus/1-1	Bus	-	100.0	1.000	0.0	0.0	0.0
IEEE39 Bus/30	Bus	-	100.0	1.000	0.0	0.0	0.0
IEEE39 Bus/12-1	Bus	-	100.0	1.000	0.0	0.0	0.0
IEEE39 Bus/load3	RLC load	PQ	342.3	1.000	0.0	322.0	2.4
IEEE39 Bus/10-1	Bus	-	100.0	1.000	0.0	0.0	0.0
IEEE39 Bus/15-1	Bus	-	100.0	1.000	0.0	0.0	0.0
IEEE39 Bus/load4	RLC load	PQ	329.9	1.000	0.0	500.0	184.0
IEEE39 Bus/22-1	Bus	-	100.0	1.000	0.0	0.0	0.0
IEEE39 Bus/T2:900MVA 20	Bus	-	345.0	1.000	0.0	0.0	0.0

Block name	Block type	Bus type	Vbase (kV)	Vref (pu)	Vangle (deg)	P (MW)	Q (Mvar)
IEEE39 Bus/T2:900MVA 20	Bus	-	345.0	1.000	0.0	0.0	0.0
IEEE39 Bus/T2:900MVA 20	Bus	-	345.0	1.000	0.0	0.0	0.0
IEEE39 Bus/load26	RLC load	PQ	351.2	1.000	0.0	0.0	139.0
IEEE39 Bus/load12	RLC load	PQ	216.1	1.000	0.0	7.5	88.0
IEEE39 Bus/load15	RLC load	PQ	334.5	1.000	0.0	320.0	153.0
IEEE39 Bus/load16	RLC load	PQ	341.1	1.000	0.0	329.0	32.3
IEEE39 Bus/load18	RLC load	PQ	341.9	1.000	0.0	158.0	30.0
IEEE39 Bus/load20	RLC load	PQ	340.5	1.000	0.0	628.0	103.0
IEEE39 Bus/load21	RLC load	PQ	343.4	1.000	0.0	274.0	115.0
IEEE39 Bus/load23	RLC load	PQ	352.0	1.000	0.0	247.5	84.6
IEEE39 Bus/load24	RLC load	PQ	343.9	1.000	0.0	308.6	-92.0
IEEE39 Bus/load25	RLC load	PQ	354.8	1.000	0.0	224.0	47.2
IEEE39 Bus/load27	RLC load	PQ	345.1	1.000	0.0	281.0	75.5
IEEE39 Bus/load28	RLC load	PQ	351.7	1.000	0.0	206.0	27.6
IEEE39 Bus/load29	RLC load	PQ	352.2	1.000	0.0	283.5	26.9
IEEE39 Bus/load7	RLC load	PQ	330.0	1.000	0.0	233.0	84.0
IEEE39 Bus/load8	RLC load	PQ	329.1	1.000	0.0	522.0	0.0

Appendix 10: Approval of Research Proposal and Supervisors

C3

MURANG'A UNIVERSITY OF TECHNOLOGY

Office of the Director, Postgraduate Studies

E-mail: bps@mut.ac.ke
Website: www.mut.ac.ke
P.O. Box 75-10200
Murang'a, Kenya

Ref: MUT/ARP/PGS/19/2020 /VOL.1 **Date:** 3rd April, 2024

Ms. Ngugi Winnie Wambui (EN400/5200/2018)
School of Engineering and Technology
Murang'a University of Technology,
P.O. Box 75-10,200
Murang'a.

Dear Ms. Ngugi,

RE: APPROVAL OF RESEARCH PROPOSAL AND SUPERVISORS.

I am pleased to inform you that the Directorate of Postgraduate Studies on 25th March, 2024 considered and approved your Masters research proposal entitled ***"The Impact of Aggregation of Double Fed Induction Generator Based Wind Turbines on Transient Stability"*** and appointed the following as supervisors:

1. Prof. Eng. Christopher Maina – Murang'a University of Technology
2. Dr. Charles Mwaniki - Machakos University

You may now proceed with your data collection subject to obtaining research permit from NACOSTI, if required. You should also begin consulting your supervisors and submit through them quarterly progress reports to the Director Postgraduate Studies through your CoD and School Dean. Progress Reports forms can be accessed in the Student Portal.

It is the policy and regulations of the University that you observe deadlines. The guidelines on Postgraduate supervision can be accessed in the post graduate Handbook.

Your responsibilities as a student will include, among others;

i. Maintain regular consultation with your supervisor(s), at least once a month
ii. Submit quarterly reports on time, through your supervisors, CoD, Dean and to the Director of Postgraduate Studies;
iii. Ensure quality work all through;

CamScanner

iv. Present your research findings at 2-3 seminars/conferences prior to thesis examination.

v. Publish one article from your research findings in a refereed journal prior to thesis examination.

For any further clarification please contact the undersigned.

Yours Sincerely,

Prof. Geoffrey Muchiri, PhD
Director, Postgraduate Studies
GM/PIN

DIRECTORATE OF POSTGRADUATE STUDIES
MURANG'A UNIVERSITY OF TECHNOLOGY
P. O. Box 75 - 10200, MURANG'A
Tel: 0771463515, Email: info@mut.ac.ke

Copy to:
1. Registrar, Academics, Research and Students Affairs
2. Dean, School of Engineering and Technology

CamScanner

Appendix 11: Publication

The following paper has been published from this thesis.

[1] W. W. Ngugi, C. M. Maina, and C. Mwaniki, "Assessing the transient stability of aggregated doubly-fed induction generator (DFIG) based wind turbines using PSO-tuned control technique," *International Journal of Engineering Development and Research (IJEDR)*, vol. 13, no. 4, Dec. 2025, ISSN: 2321-9939.